A Multi-Objective Optimisation of a Stiffened GFRP Sandwich Panel with a Bilayer Core Structure, through Finite Element Analysis

Matthias Grech

Dissertation submitted to the Faculty for the Built Environment, University of Malta in part fulfilment of the requirements for the attainment of the degree of Master of Engineering (Structural Engineering)

July 2024

Niddedika din id-dissertazzjoni lil ommi u lil missieri.

L-Università ta' Malta

FACULTY/INSTITUTE/CENTRE/SCHOOL Faculty for the Built Environment

DECLARATIONS BY POSTGRADUATE STUDENTS

(a) Authenticity of Dissertation

I hereby declare that I am the legitimate author of this Dissertation and that it is my original work.

No portion of this work has been submitted in support of an application for another degree or qualification of this or any other university or institution of higher education.

I hold the University of Malta harmless against any third party claims with regard to copyright violation, breach of confidentiality, defamation and any other third party right infringement.

(b) Research Code of Practice and Ethics Review Procedures

I declare that I have abided by the University's Research Ethics Review Procedures. Research Ethics & Data Protection form code BEN-2023-00099.

As a Master's student, as per Regulation 77 of the General Regulations for University Postgraduate Awards 2021, I accept that should my dissertation be awarded a Grade A, it will be made publicly available on the University of Malta Institutional Repository.

Acknowledgements

First and foremost, I would like to thank my tutor, Dr Jeanette Mireille Muñoz Abela, B.E.&A. (Hons)(Melit.), M.Sc. (Lond.), Ph.D. (Lond.), D.I.C., Eur. Ing. (FEANI), Perit, for the advice, words of encouragement, numerous critical discussions, and ultimately for taking a chance on me and giving me the confidence to explore a relatively new area of research within civil engineering.

Secondly, I would like to thank my parents. Their unwavering support, not only throughout this journey, but also in every venture I have pursued in my life, has been invaluable. For this I am incredibly grateful. I attribute everything I have achieved and will achieve, to them.

I take full responsibility for any shortcomings in this dissertation.

Abstract

Glass fibre reinforced polymer (GFRP) sandwich panels, known for their high strength-to-weight ratio, are increasingly utilized in weight-sensitive civil engineering applications. This dissertation focused on optimizing a stiffened, bilayer GFRP sandwich panel as a monolithic slab within domestic environments. This study examined how variations in facesheet thickness, core thickness, and stiffener angle (input variables) impacted vertical deflection, panel mass, material cost (output variables), and Von Mises stresses.

A preliminary design of the GFRP sandwich panel, based on literature, was analysed through finite element analysis (FEA) on *ANSYS Workbench*. A parametric model with 432 different configurations was set up. The effects of the input and output variables were globally analysed using a *Design of Experiment* (DOE) function followed by a *Response Surface* function, and locally analysed through FEA applied to specific configurations. The optimal panel design was derived using a *non-dominated sorting algorithm*, parameter-related constraints, and trends observed from this dissertation.

The results showed that higher panel mass and material cost reduced vertical deflection. Increasing core thickness was more effective than facesheet thickness in minimizing vertical deflection, panel mass, and material cost. Varying stiffener angles had minimal impact on the output variables. Increasing the core and facesheet thickness, respectively, globally reduced stress levels. Non-orthogonal stiffener angles shifted the stress distribution: reducing stress in the core, increasing it in the stiffening system, and maintaining it in the facesheets.

The optimal panel, chosen based on the described trends from the non-dominated solutions with deflections under 8.33 mm, featured 100 mm core, 1.2 mm facesheet, and a 50^{o} (or by symmetry, 130^{o}) stiffener angle.

Keywords: GFRP Sandwich Panel; Bilayer Polyurethane Foam Core; Trapezoidal Stiffening System; Multi-Objective Optimization; Finite Element Analysis

Table of Contents

List of Tables

List of Figures

Glossary

The technical terms used in this dissertation are provided hereunder.

Type		Symbol	Definition	Units
Material Properties	**General**	ρ_f	Density of Fibre	[kg/m^3]
		ρ_{FRP}	Density of Fibre Reinforced Polymer	[kg/m^3]
		ρ_{HPU}	Density of High-Density PU Foam	[kg/m^3]
		ρ_{LPU}	Density of Low-Density PU Foam	[kg/m^3]
		ρ_m	Density of Matrix	[kg/m^3]
		m_F	Mass of Facesheets	[kg]
		m_{HPU}	Mass of High-Density PU Foam	[kg]
		m_{LPU}	Mass of Low-Density PU Foam	[kg]
		m_S	Mass of Stiffening System	[kg]
		m_T	Mass of Sandwich Panel	[kg]
		V_f	Fibre Volume Ratio	[NA]
		V_m	Matrix Volume Ratio	[NA]
	Mechanical	D	Flexural Rigidity	[GNm^2]
		E_{11}	Longitudinal Modulus of Elasticity of Fibre Reinforced Polymer	[GPa]
		E_{22}	Transverse Modulus of Elasticity of Fibre Reinforced Polymer	[GPa]
		E_{33}	Vertical Modulus of Elasticity of Fibre Reinforced Polymer	[GPa]
		E_C	Modulus of Elasticity of Core	[MPa]
		E_f	Modulus of Elasticity of Fibre	[GPa]
		E_F	Modulus of Elasticity of Facesheet	[GPa]
		E_{HPU}	Modulus of Elasticity of High-Density PU Foam	[MPa]
		E_{LPU}	Modulus of Elasticity of Low-Density PU Foam	[MPa]
		E_m	Modulus of Elasticity of Matrix	[GPa]

Type		Symbol	Definition	Units
Material Properties	**Mechanical**	E_S	Modulus of Elasticity of Stiffening System	[GPa]
		E_T	Modulus of Elasticity of Sandwich Panel	[GPa]
		G_{12}	Shear Modulus of Elasticity of Fibre Reinforced Polymer; 12-axis	[GPa]
		G_{13}	Shear Modulus of Elasticity of Fibre Reinforced Polymer; 13-axis	[GPa]
		G_{23}	Shear Modulus of Elasticity of Fibre Reinforced Polymer; 23-axis	[GPa]
		G_f	Shear Modulus of Elasticity of Fabric	[GPa]
		G_{HPU}	Shear Modulus of Elasticity of High-Density PU Foam	[MPa]
		G_{LPU}	Shear Modulus of Elasticity of Low-Density PU Foam	[MPa]
		G_m	Shear Modulus of Elasticity of Matrix	[GPa]
		v_{12}	Poisson's Ratio of Fibre Reinforced Polymer; 12-axis	[NA]
		v_{23}	Poisson's Ratio of Fibre Reinforced Polymer; 23-axis	[NA]
		v_{13}	Poisson's Ratio of Fibre Reinforced Polymer; 13-axis	[NA]
		v_f	Poisson's Ratio of Fibre	[NA]
		v_{HPU}	Poisson's Ratio of High-Density PU Foam	[NA]
		v_{LPU}	Poisson's Ratio of Low-Density PU Foam	[NA]
		v_m	Poisson's Ratio of Matrix	[NA]
		σ_{11}	Longitudinal Tensile Strength of Fibre Reinforced Polymer	[MPa]
		σ_{22}	Transverse Tensile Strength of Fibre Reinforced Polymer	[MPa]
	Cost	c_f	Cost per Unit Mass of Fabric	[€/kg]

Type		Symbol	Definition	Units
Material Properties	**Cost**	c_{FRP}	Cost per Unit Mass of Fibre Reinforced Polymer	[€/kg]
		c_{HPU}	Cost per Unit Volume of High-Density PU Foam	[€/m^3]
		c_{LPU}	Cost per Unit Volume of Low-Density PU Foam	[€/m^3]
		c_m	Cost per Unit Mass of Matrix	[€/kg]
		C_f	Cost of Fabric	[€]
		C_{FRP}	Cost of Fibre Reinforced Polymer	[€]
		C_{HPU}	Cost of High-Density PU	[€]
		C_{LPU}	Cost of Low-Density PU	[€]
		C_m	Cost of Matrix	[€]
		C_T	Cost of Sandwich Panel	[€]
Geometric Properties		A	Cross-Sectional Area	[m^2]
		b	Width of Sandwich Panel	[m]
		I_C	Second Moment of Area of Core	[m^4]
		I_F	Second Moment of Area of Facesheets	[m^4]
		I_T	Second Moment of Area of Sandwich Panel	[m^4]
		I_S	Second Moment of Area of Stiffening System	[m^4]
		L	Length of Sandwich Panel	[m]
		L_S	Length of Trapezoidal Stiffener	[mm]
		R	Radius	[m]
		S	First Moment of Area	[m^3]
		T_C	Thickness of Core	[mm]
		T_{Ct}	Thickness of Total Core	[mm]
		T_{Fb}	Thickness of Bottom Facesheet	[mm]
		T_{Ft}	Thickness of Top Facesheet	[mm]
		T_S	Thickness of Stiffener	[mm]

Type	Symbol	Definition	Units
Geometric Properties	T_{Sl}	Thickness of Half Stiffener (Left)	[mm]
	T_{Sr}	Thickness of Half Stiffener (Right)	[mm]
	V_{LPU}	Volume of Low-Density PU Foam	[m^3]
	V_{HPU}	Volume of High-Density PU Foam	[m^3]
	V_m	Volume of Matrix	[m^3]
	V_f	Volume of Fibre	[m^3]
	ϑ_1	Stiffener Angle #1	[degrees]
	ϑ_2	Stiffener Angle #2	[degrees]
Statics	M	Bending Moment	[Nm]
	q	Uniformly Distributed Load	[N/m]
	V	Shear Force	[N]
	Δ	Maximum Vertical Deflection at Longitudinal Midplane	[mm]
	Δ_1	Vertical Deflection due to Bending	[mm]
	Δ_2	Vertical Deflection due to Shear	[mm]
	Δ_T	Total Vertical Deflection	[mm]
	σ_C	Stress in Core	[MPa]
	σ_F	Stress in Facesheet	[MPa]

The abbreviations used in this dissertation are provided hereunder.

Abbreviation	Definition
A	Angle
AA	Analytical Analysis
C	Core
CFRP	Carbon Fibre Reinforced Polymer
DOE	Design of Experiment
F	Facesheet
FE	Finite Element
FEA	Finite Element Analysis
FRP	Fibre Reinforced Polymer
GFRP	Glass Fibre Reinforced Polymer
HM	High Modulus
HS	High Strength
NYSDOT	New York State Department of Transportation
PU	Polyurethane
PVC	Polyvinylchloride
RC	Reinforced Concrete

1. Introduction

1.1. Background

In engineering, solid materials are classified into four main groups: metals, ceramics, polymers, and composites. The latter refers to a combination of the aforementioned material families. An example of a composite material is glass-fibre reinforced polymer (GFRP), which consists of glass fibres (a ceramic) embedded within a polymeric material (Callister W. D., 2007). This dissertation explored the behaviour of sandwich panels made from GFRP, as discussed later.

Composite materials have typically been used in high-performance applications in the aerospace, marine, and sports industries (Callister W. D., 2007). However, there has been an increasing amount of research focused on implementing these materials in civil engineering applications. This has been achieved through the use of composite wraps for strengthening purposes (Vijayan, et al., 2023), and more recently through the development of structural sandwich panels (Manalo, Aravinthan, Fam, & Benmokrane, 2016).

Composite sandwich panels are structural members, typically consisting of a polymeric core, sandwiched between top and bottom GFRP facesheets (Kampner & Grenestedt, 2007; Fam & Sharaf, 2010). Such members have found widespread popularity owing to their high strength-to-weight ratio. In civil engineering, this enables such systems to be used in weight-sensitive cases, typically as roofing solutions, as well as bridge decks, to name a few (Aref, Alampalli, & He, 2004; Keller, Haas, & Vallee, 2008; Keller, Rothe, de Castro, & Osei-Antwi, 2013).

Recently however, effort has been placed in introducing such technology within domestic environments, for the purpose of a state-of-the-art flooring solution, be it for rehabilitation purposes, or building anew (Correia, Garrido, Gonilha, & Branco, 2012; Mastali, Valente, & Barros, 2013; Garrido M. , 2016; Noel & Fam, 2021).

Research in this regard has shown that GFRP sandwich panels are very much prone to failure due to core failure. As a result, widespread development has been placed on enhancing the performance of the core. Amongst such developments, multilayer core systems, i.e. core systems composed of multiple non-fibrous materials, and stiffened core material systems, i.e. core systems reinforced through the introduction of a stiffening system, have been found to be most promising (Manalo, Aravinthan, Fam, & Benmokrane, 2016).

1.2. Goals & Objectives

This dissertation therefore sought to further contribute to the development and adoption of composite materials in the construction industry by investigating core-strengthening techniques in GFRP sandwich panels used as monolithic slab members in domestic environments. The research question addressed was:

"What would be the optimal configuration for a trapezoidally-stiffened, bilayer, GFRP sandwich panel, used as a monolithic slab in domestic environments?"

The answer was sought through a multi-objective optimization process, considering vertical deflection, panel mass, and material cost (output variables). The optimization involved varying the following input variables: a) core thickness, b) facesheet thickness, and c) the angle of the trapezoidal stiffening system.

The objectives of this dissertation were twofold: first, to study the effects of the input variables on the output variables, including Von Mises stresses; and second, to determine the optimal panel input parameters for optimal performance in vertical deflection, panel mass, and material cost for use as a monolithic slab in domestic environments.

1.3. Overview of the Research Methods

In achieving the set objectives, a preliminary design of the GFRP sandwich panel in consideration was first set up. This was conducted according to guidelines derived on the basis of state-of-the-art research obtained from the literature review.

The analysis of this panel was then carried out via finite element analysis (FEA) using *ANSYS Workbench* (ANSYS, Inc., 2023). In this regard, a preliminary study was first conducted to establish the basic methodology based on a study by Manjusha et al. (2020). This constituted setting up material and geometric parameters, followed by the setup of load and boundary conditions. Successful implementation of the methodology by Manjusha et al. (2020) was noted to have been achieved if the discrepancy between the results of the preliminary study and the published study was less than or equal to 5.00%.

This methodology was then adapted to the GFRP sandwich panel design set up. Given a total of 432 panel configurations, determining the relationship between the input variables and the output variables individually would have been impractical. Instead, a machine learning algorithm was applied to predict the global behaviour of the input variables on the output variables. These predictions were based on a data set with known performance metrics for predefined panel configurations.

Next, a plot of the output variables was generated, from which identified trends were further investigated through the application of finite element analysis on relevant panel configurations. This allowed the effects of the input variables on the output variables, and Von Mises stresses, to be locally studied.

Finally, with the aim of identifying the optimal panel configuration, a *non-dominated sorting algorithm* was applied to the predicted data set. This, together with the application of parameter-related constraints, and observed trends allowed for the optimal panel configuration to be determined.

1.4. Structure of the Dissertation

This dissertation consists of five main chapters. This first (and current) chapter discusses the background which gave rise to such dissertation, and associated goals and objectives. This was followed by an overview of the research methods employed.

The literature review served to provide a holistic understanding on composite materials, and fibre-reinforced polymer sandwich systems. This was followed by an understanding on the mechanics of sandwich systems, and their applications within civil engineering. Focus was then placed on the current principal developments taking place within fibre-reinforced polymer sandwich systems, whereby further depth was provided on the state-of-the-art developments pertaining stiffened core material systems, and multilayer core systems. The latter findings served to develop a set of guidelines, that allowed for the design of a standard-sized, trapezoidally-stiffened, bilayer GFRP sandwich panel to be optimized.

The methodology chapter was broken down in two sections. The first served as a preliminary study, conducted with the aim of following an established methodology in numerically modelling a GFRP sandwich panel. The second sought to describe the adaptation of the aforementioned established methodology to the designed GFRP sandwich panel. It additionally also served to describe the steps adopted in determining the effects of the input variables on the output variables, and in optimizing the designed GFRP sandwich panel.

The results chapter was set up such that it corresponded to the objectives of this dissertation. It was therefore composed of two sections, with the first discussing the effects of the input variables on the output variables, and Von Mises stresses. The second section discussed the rationale that allowed for the optimal panel configuration to be determined.

The last chapter serves to draw the main conclusions identified in this dissertation, as well as limitations encountered. Some recommendations pertaining future research was also provided.

2. Literature Review

This chapter delved into the realm of fibre-reinforced polymer (FRP) sandwich systems within civil engineering, beginning with a foundational exploration of composite materials. It progressed to discuss the composition and structural principles of FRP sandwich panels, with emphasis given to the *Classical Sandwich Panel Theory*. Highlighting their versatile applications in civil engineering, the discussion then shifted towards recent advancements, particularly focusing on innovations in core materials. Finally, this chapter concluded by synthesizing key insights, applying them to the design context of a trapezoidally-stiffened, bilayer GFRP sandwich panel.

2.1. Composite Materials

A composite material is a material which is made up of two or more constituents, whose performance exceeds that of the individual constituents themselves. This, albeit each constituent maintains their chemical, physical, and mechanical properties. The two constituents making up a composite material are the dispersed phase (also commonly known as the reinforcement phase), and the matrix phase. The former typically imparts high strength and stiffness to the composite material, whilst the latter ensures that the dispersed phase is maintained in the proper spacing and orientation, and protected from abrasion and the surrounding environment (Jones, 1999; Campbell, 2010). Refer to Figure 2-1.

Typical reinforcement materials include fibres, such as glass, carbon, or aramid. Fibres are typically used to reinforce polymer matrices, hence the term; fibre-reinforced polymer. Typical polymeric matrix materials include epoxy, phenolic, polyurethane, and polyimide (Barbero, Materials, 2018).

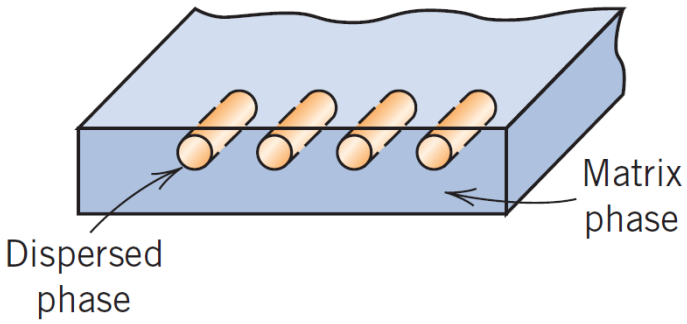

Figure 2-1: The phases making up a typical composite specimen include the dispersed phase, and the matrix phase (Callister W. D., 2007).

As opposed to bulk materials, such as metals and polymers, composite materials are deemed to behave in an orthotropic manner; a sub-set of anisotropy. This is because the properties of a composite material differ along three mutually perpendicular axes of symmetry. As a result of this, only normal strains are produced on the application of a load applied parallel to such axis. This behaviour is entirely dependent on the layer (ply) sequence applied (Campbell, 2010; Barbero, Micromechanics, 2018). Understanding this is important as it allowed for proper composite material modelling to take place during the numerical modelling portion of this dissertation.

When speaking on ply sequences, it is common to speak of the 1-2-3 coordinate system. Here the 1-axis denotes the direction parallel to the fibres, the 2-axis denotes the direction perpendicular to the fibres, and the 3-axis denotes the direction normal to the plane defined by axis 1 and 2. Such coordinate system is denoted in Figure 2-2. Applying a load parallel to the fibre direction will yield a longitudinal modulus of elasticity, and a longitudinal tensile strength similar in magnitude to that of the fibres themselves. This is denoted by E_{11}, and σ_{11}, respectively. Note that as this will be further explained, such properties are also dependent on the properties of the matrix (Campbell, 2010; Barbero, Ply Mechanics, 2018).

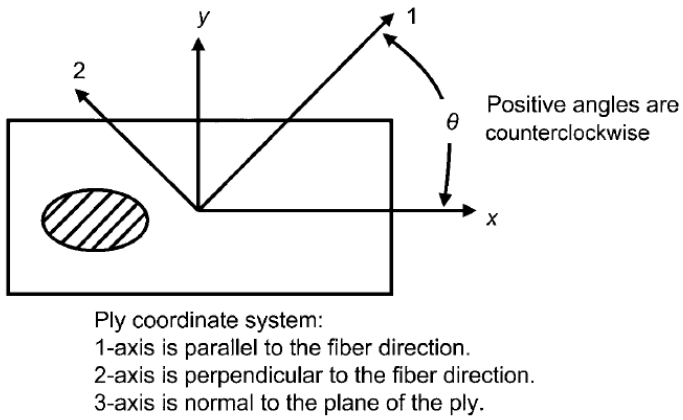

Figure 2-2: Ply sequence denoted via 1-2-3 coordinate system. This is shown in tandem with the cartesian coordinate system, albeit being independent of it (Campbell, 2010)

On the other hand, applying a load perpendicular to the fibre direction will yield a transverse modulus of elasticity, and a transverse tensile strength similar to that of the matrix in magnitude. This is much smaller to that of the fibre, and is denoted by E_{22} and σ_{22}, respectively. This decrease in modulus of elasticity and tensile strength can be attributed to the fact that in this manner, the fibres and the matrix are functioning in series, thus making the composite material dependent on the matrix. This phenomenon is graphically depicted in Figures 2-3A and B. Note that similarly, as described in the case prior, such properties are also dependent on the properties of the fibre (Campbell, 2010; Barbero, Ply Mechanics, 2018).

Another contributing factor to a composite's mechanical properties is the fibre volume ratio. Refer to Figure 2-3C. For a fibre volume ratio (V_f) of unity, the longitudinal and transverse modulus of elasticity of the composite material are equal to the fibre's modulus of elasticity (E_f), being that only one constituent is available (the fibre). Hence $E_{11} = E_{22} = E_f$. For fibre volume ratios less than unity, E_{11} and E_{22} begin to approach the magnitude of matrix's modulus of elasticity (E_m). This is achieved at different rates, with the E_{22} being more sensitive in this regard. This is attributed to the orthotropic behaviour of composite materials, whereby the system is much more dependent on the weaker matrix when loaded in the transverse direction (Campbell, 2010; Barbero, Ply Mechanics, 2018).

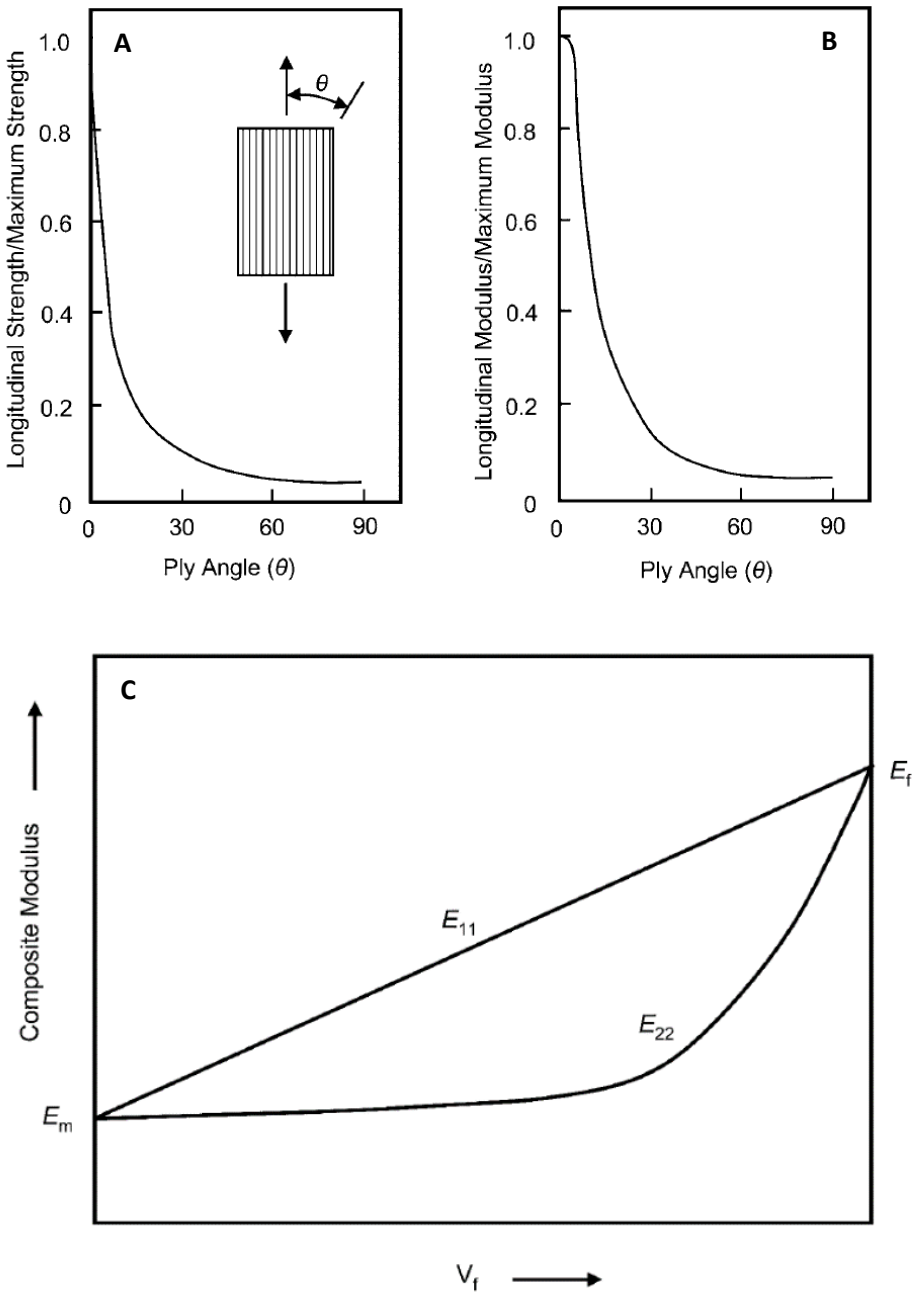

Figure 2-3: (A) and (B) depict the variation in longitudinal strength, and modulus, as a function of ply angle. (C) exhibits the relationship between the composite modulus and fibre volume fraction, for a unidirectional lamina (Campbell, 2010).

2.2. Fibre-Reinforced Polymer Sandwich Systems

Fibre-reinforced polymer sandwich systems are panels, used in applications within which a combination of high strength and low weight are required. These typically constitute of a polymeric central core, sandwiched via top and bottom FRP facesheets (Kampner & Grenestedt, 2007; Fam & Sharaf, 2010)

In said arrangement, flexural strength and stiffness is imparted via the outer facesheets, whilst shear strength and rigidity are imparted via the inner core (Kampner & Grenestedt, 2007; Manjusha & Althaf, 2020). Typical facesheet materials include glass fibre reinforced polymers (GFRP), or carbon fibre reinforced polymers (CFRP), albeit the former is more commonly used in civil engineering works owing to its economic efficiency. Both materials are identified to be ideal candidates providing the sandwich panel with high specific strength and stiffness (Manalo, Aravinthan, Fam, & Benmokrane, 2016).

Figure 2-4A illustrates the stress-strain relationships of high modulus (HM) carbon reinforced polymer, high strength (HS) carbon reinforced polymer, aramid reinforced polymer, glass reinforced polymer, and carbon reinforced polymer, compared to mild steels, in the form of tendons and bars (Abbood, Odaa, Hasan, & Jasim, 2021). This suggests that the stress-strain relationship of typical FRP materials is linear.

As for core materials, polyvinylchloride (PVC) foam, and polyurethane (PU) foam are typically used. These are used in densities ranging from 30 kg/m^3 to 400 kg/m^3, and 21 kg/m^3 to 400 kg/m^3, respectively[i]. Between the two, PU foams are identified to be relatively cheaper, and hence, more commonly adopted in civil engineering works (Manalo, Aravinthan, Fam, & Benmokrane, 2016).

As exhibited in Figure 2-4B, PU foams follow a nonlinear viscoelastic stress-strain relationship. This relationship is typically characterized by an initial elastic region where the foam behaves elastically under relatively low strains. It is followed by a plateau region where the strain increases occur at a relatively constant applied stress. Finally, at very high strains, significant stress increases are observed, until failure (Elliot, Windle, Eeckhaut, & Ludwig, 2002). Understanding this complex stress-strain relationship is crucial, as it poses challenges in accurately developing mathematical models that describe the behaviour of PU foams.

[i] Note that here, the foams towards the lower-bound find more practical use in providing excellent thermal insulation, as opposed to enhancing structural rigidity.

Throughout the years, various different foam core geometries have been adopted, with the most basic form consisting of a simple foam core. This is shown in Figure 2-5A (TOPOLO, 2023). Other types of foam cores include the honeycomb core, and the trussed core. These are shown in Figure 2-5B and C (TOPOLO, 2022; Manalo, Aravinthan, Fam, & Benmokrane, 2016).

Compared to the basic core, the honeycomb core performs better in both compression and in shear, and the trussed core provides a lighter sandwich panel, owing to the reduced materials utilisation (Wicks & Hutchinson, 2001). Nevertheless, practical issues have mitigated widespread use of such core typologies. Trussed-core sandwich panels are very difficult to produce, owing to the difficulty in ensuring fibre continuity across truss members of adjacent panels. Additionally, the presence of voids present between the facesheets and the core makes it difficult for mechanical connectors to be effectively implemented. This is also true for honeycomb core panels, which are additionally, also susceptible to moisture entrapment that ultimately leads to skin-core delamination (Kooistra & Wadley, 2007). This, together with the increased costs involved in implementing such solutions, give honeycomb core and trussed core sandwich panels a high barrier of entry within civil engineering industry (Reis & Rizkalla, 2008). Therefore, for the purposes of this dissertation, further focus was given to the basic foam core.

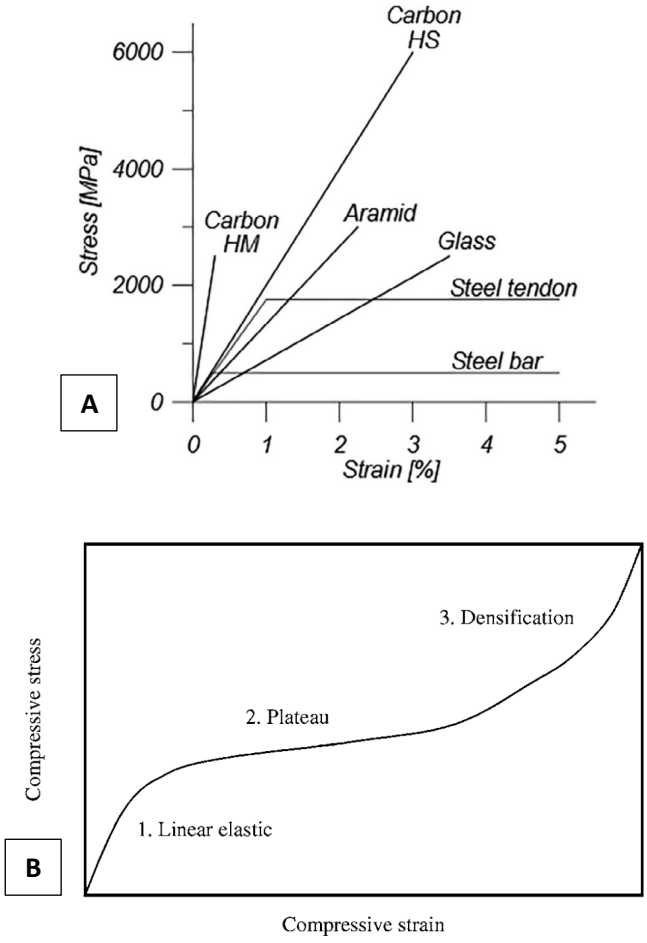

Figure 2-4: Typical stress-strain relationship of: (A) FRP materials, and mild steels (Abbood, Odaa, Hasan, & Jasim, 2021); (B) PU foam (Elliot, Windle, Eeckhaut, & Ludwig, 2002).

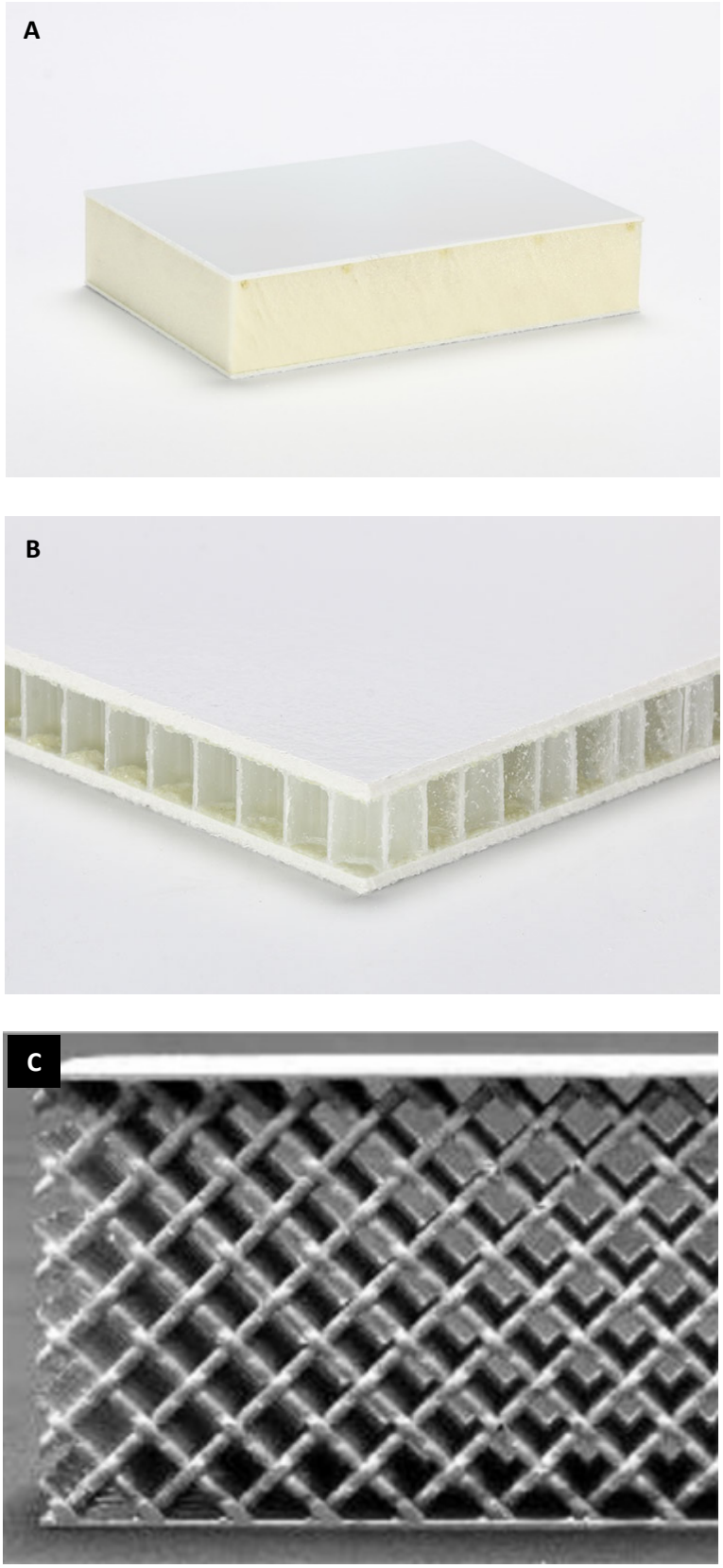

Figure 2-5: GFRP sandwich panels of different core geometries are shown; (A) simple foam core (TOPOLO, 2023); (B) honeycomb core (TOPOLO, 2022); (C) trussed core (Manalo, Aravinthan, Fam, & Benmokrane, 2016)

2.3. Classical Sandwich Panel Theory

This section served to describe the basic principles behind the mechanics of sandwich panels. This was made through the introduction of the *Classical Sandwich Panel Theory*, which considers first order shear deformation, as well as unidirectional behaviour of the panels. In this regard, reference is made to an isotropic sandwich panel of width, b, core thickness, T_C, equal top and bottom facesheet thickness, T_{Ft} and T_{Fb}, and length, L, with a length-to-width ratio of greater or equal to 3 (Allen, Sandwich Beams, 1969). This is shown in section in Figure 2-6.

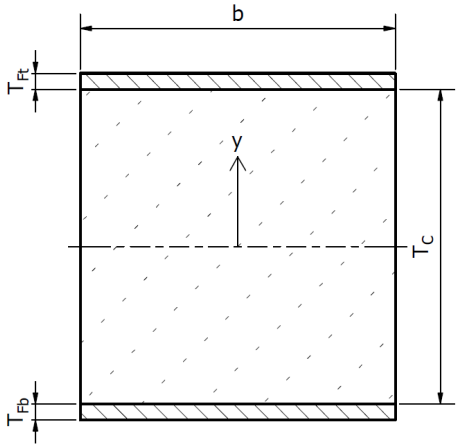

Figure 2-6: Cross-section of a typical sandwich panel.

This theory assumes that the cross-section of the panel remains plane to the longitudinal axis when deflected. This assumption leads to a well-known relationship between the applied bending moment (M), and the curvature of the member $\left(\frac{1}{R}\right)$, as described in Eq. 2.1 (Allen, Sandwich Beams, 1969).

$$\frac{M}{E_T I_T} = -\frac{1}{R} \qquad \text{Eq. 2.1}$$

Here, the product of the panel's Young's Modulus (E_T), and the second moment of area (I_T) encompass the panel's flexural rigidity, D. Owing to the different materials used in the construction of a sandwich panel, the flexural rigidity is the sum of the flexural rigidities of the individual components making up the panel. For a sandwich panel consisting of a central core (denoted by subscript C), sandwiched by top and bottom facesheets (denoted by subscript F), this is given by Eq. 2.2 (Allen, Sandwich Beams, 1969).

$$D = E_T I_T = E_F I_F + E_C I_C \qquad \text{Eq. 2.2}$$

Note that in the case that a stiffening system with the same material properties as the facesheet were introduced, Eq. 2.2 would need to be modified to include the addition of $E_F I_S$.

When calculating the stresses across the sandwich panel, the flexure formula is applicable owing to the assumption that cross-section remains plane to the longitudinal axis. However, an adapted version of this formula is required to account for the composite nature of the cross-section. The

magnitude of the bending stress within the facesheets (σ_F) and core (σ_C), is expressed by Eq. 2.3 and Eq. 2.4, respectively (Allen, Sandwich Beams, 1969).

$$\sigma_F = \frac{My}{D} E_F \quad \text{Eq. 2.3}$$

$$\sigma_C = \frac{My}{D} E_C \quad \text{Eq. 2.4}$$

Note that, *y* is representative of the vertical translation from the neutral axis to the point at which stress is of concern. This is shown in Figure 2-6.

Similarly, the shear formula is applicable for calculating shear stress across the sandwich panel, owing to the adopted assumption. As with the flexure formula, an adapted version is presented in Eq. 2.5 to account for the composite nature of the cross-section (Allen, Sandwich Beams, 1969).

$$\tau = \frac{V}{Db} \sum (SE) \quad \text{Eq. 2.5}$$

Note that *V* is the shear force associated with the region in consideration, and *S* is the first moment of area.

Calculations pertaining to the deflection of a simply supported sandwich panel are found to be different to those typically used for beams and shafts. Owing to the limit stiffness of the core, the application of shear to the core is noted to impart significant deflections to the core. As a result of this, the panel's ultimate deflection (Δ) is defined as a function of the deflection due to bending (Δ_1), and shear (Δ_2). This is shown in Eq. 2.6. In the case of a uniformly distributed load, acting on a simply supported panel, the total deflection is given by Eq. 2.7 (Allen, Sandwich Beams, 1969).

$$\Delta = \Delta_1 + \Delta_2 \quad \text{Eq. 2.6}$$

$$\Delta = \frac{5qL^4}{384D} + \frac{qL^2}{8AG} \quad \text{Eq. 2.7}$$

Here *q* represents the uniformly distributed load, and *A* depends on the specific panel configuration under consideration. For an unstiffened panel, *A* is the cross-sectional area of the core. However, in the case of a stiffened panel, *A* refers to the cross-sectional area of the stiffening system. Similarly, *G* also varies depending on whether the panel is stiffened or not. If unstiffened, *G* is the shear modulus of the core material. In contrast, for stiffened panels, *G* represents the shear modulus of the stiffening material. In this latter scenario, due to E_F being significantly greater than E_C, the core's contribution to shear resistance is negligible and thus disregarded (Allen, Sandwich Beams, 1969).

Note that due to the orthotropic behaviour of GFRP sandwich panels, for instances of unidirectionality (that is, panel-to-width ratio ≥ 3.0), the *Classical Sandwich Panel Theory* is still found to apply. In this regard, if unidirectional behaviour is predominantly noted to occur along the 1-axis, E_F is to be substituted by E_{11} wherever applicable in the described equations (Allen, Sandwich Beams, 1969).

2.4. Uses in Civil Engineering

In understanding as to why research in composite materials for civil engineering use is important, the applicability of FRP sandwich systems needs to be considered. In this regard such systems are found to already be in use in housing, bridge and pedestrian decks, bridge beams, floating and protective structures, and railway sleepers (Manalo, Aravinthan, Fam, & Benmokrane, 2016).

The decision of opting for such materials as opposed to more conventional ones, such as steel and reinforced concrete, is predominantly owed due to the relatively high strength-to-weight ratio imparted by FRP sandwich systems. This therefore allows engineers to design structures that are sufficient in resisting the applied loads, while only being a fraction of the weight of a typical steel/reinforced concrete (RC) structure. For context, the quasi-permanent load of a concrete slab (for housing-purposes) varies from 8 kN/m^2 to 10 kN/m^2, whilst that of a GFRP panel varies from 3 kN/m^2 to 5 kN/m^2 (Arruda & Lopes, 2020).

This difference was further reinforced in Fam & Sharaf (2010). Via numerical analysis, the authors showed that in achieving the same strength properties exhibited by the tested GFRP sandwich panels, equivalent RC sections which are 9 to 14 times the weight of a GFRP sandwich panel, would be required. Note that this was found to be true for a RC slab whose section is dimensionally similar as the GFRP panel being emulated, using C30 concrete, a 25 mm cover, and steel reinforcement of yield and ultimate strength of 400 MPa and 550 MPa, respectively (Fam & Sharaf, 2010).

This characteristic enables sandwich panels to be sufficiently lightweight such that they may be handled via a limited number of workers, without the need of additional machinery to lift and set up the panel. This, in addition to the fact that such panels are prefabricated, brings about increases in time efficiency, which in turn brings about reductions in construction-related costs. Furthermore, in the case that such panels are manufactured abroad, the energy associated in transporting such panels will be less to those derived from transporting traditional building materials (namely RC and steel) (Garrido M. , 2016; Arruda & Lopes, 2020).

Owing to the facesheets of the panel, such panels are envisaged to also contribute minimally to maintenance costs. This is attributed to the good performance characteristics FRP laminates exhibit within harsh environments (Garrido M. , 2016).

Consider the new Main Gate of the Novartis Campus in Basel, Switzerland (Figure 2-7). This constituted of a rectangular single-story building, enclosed by four glass walls. Owing to the limited load-carrying capacity of the glass walls, the designers needed a material that is sufficiently lightweight. As a result of this, the designers opted for a roofing solution, made entirely of GFRP sandwich panels. This allowed for a relatively lightweight roof structure, approximately weighing 0.7 kN/m^2, which is solely supported via the perimeter glass walls (Keller, Haas, & Vallee, 2008).

In addition to GFRP sandwich panels being lightweight, they are also identified to be excellent insulators (Arruda & Lopes, 2020). This is due to their low thermal conductivity. Such a property makes them ideal roofing/walling solutions in countries with relatively intense climates (Arruda & Lopes, 2020). As in the case of the new Main Gate of the Novartis Campus, this allowed the designers to achieve both structural and insulative functions, through a single-layer building envelope. This in turn allowed it to also serve architectural functions being that the implementation of a GFRP roof structure voids the need for an additional insulative layer (Keller, Haas, & Vallee, 2008).

GFRP panels are also useful in constructing, as well as rehabilitating, bridge decks. As an example, consider an approximately 7.8 m long reinforced concrete bridge, built in 1926, on route 248, in the town of West Union, New York. As a result of the deterioration endured, the New York State Department of Transportation (NYSDOT) aimed to revitalize the bridge, increasing its load carrying capacity in the process, as opposed to demolishing the bridge and building anew. In achieving this, the NYSDOT needed a material that was strong, but additionally, light enough, to allow an increased live load to be carried by the bridge. In this regard, the NYSDOT implemented a GFRP bridge deck. This increased the bridge's loading capacity from 10 tonnes, to around 45 tonnes (Aref, Alampalli, & He, 2004).

Figure 2-7: Novartis Campus Entrance Building, Basel, Switzerland. Roof is composed of GFRP sandwich panels (Roth, 2006)

Another instance of a rehabilitated vehicular bridge is the RC bridge across the Avancon River in Switzerland. Here the designers sought to both rehabilitate, and expand the original design, with the addition of another vehicular lane. This would upgrade the bridge from one lane to two lanes, and from a load carrying capacity of 280 kN to 400 kN. All this was to be achieved while still maintaining the original stone abutments. In ensuring that the additional load did not exceed the load-bearing capacity of the stone abutments, a GFRP decking structure was devised to lie on two longitudinal steel girders. Refer to Figure 2-8. This was identified to be a successful solution, striking a good balance between the increase in live load, and decrease in dead load. Note that the new bridge deck was estimated to be 75% lighter to a comparable RC deck, weighing in approximately at 1.57 kN/m^2 (Keller, Rothe, de Castro, & Osei-Antwi, 2013).

Figure 2-8: Vehicular bridge, Avancon River, Switzerland. Deck is composed of GFRP sandwich panels (Osei-Antwi, de Castro, Vassilopoulos, & Keller, 2013).

As demonstrated by the case studies provided, the use of sandwich panels within civil engineering has mostly been limited to roofing, and bridge-decking applications, with a predominant focus on the latter. As it pertains to the application of such technology in buildings, this area is noted to still be unexplored. Albeit this, it is important to note that research in this regard has been very much on the rise. This is particularly true in the context of implementing the discussed advantages; most of which stem from the panel's lightweight construction. In this regard, reference is made to Garrido (2016), and Mastali et al. (2013), both of whom explored the concept of implementing composite slab systems in favour of deteriorating timber floors, thus rehabilitating old masonry buildings. Similarly,

Correa et al. (2012) investigated the use of such panels as monolithic slab members[ii], and Noel et al. (2021) devised empirical design equations with the aim of adopting such panels for walling-purposes.

From the latter, it was clear that a drive is currently present in exploring the potential use of sandwich panels as an alternative construction material within the construction industry. With the aim of further contributing to this body of information, this dissertation sought to further investigate the use of sandwich panels as an alternative flooring solution.

2.5. Recent Developments

Most of the research consulted, focusing on the development of FRP sandwich panels, indicated that the manner in which FRP sandwich panels fail is very much dependent on the core material, as opposed to the outer skin arrangements. This was suggested to be the case because, relative to the outer skin, the core material imparts a very low shear stiffness to the FRP sandwich system (Manalo, Aravinthan, Fam, & Benmokrane, 2016).

Understanding this meant that therefore, in optimizing FRP sandwich systems, focus needed to be placed on core optimization. In this regard, the recent developments that have been taking place can be categorized as follows: *Corrugated Sandwich Panel Systems; Stiffened Core Material Systems; Intermediate Core Layer Systems; Multilayer Core Systems and; Hybrid Core Systems*. These will be briefly explained.

Corrugated Sandwich Panel Systems are panel systems whereby core enhancement is achieved through the introduction of corrugations to either the top or bottom skins, or both (Kampner & Grenestedt, 2007). This allows the corrugated face/s to take on a degree of the shear load being applied that would otherwise need to be fully resisted by the core. This not only allows for greater shear-carrying capabilities to be achieved, but also lighter panels to be produced. Refer to Figure 2-9A.

Similarly, *Stiffened Core Material Systems* also function by actively allowing fibres to sustain a degree of the shear load being applied to the sandwich panel. This was however noted to be achieved through the implementation of stiffeners within the core material (Reis & Rizkalla, 2008). Refer to Figure 2-9B.

[ii] In this context, the term *monolithic slabs* gives reference to a slab, void of beams along the floor span.

Intermediate Layer Systems refer to systems whereby the core is enhanced through the introduction of an additional layer, be it at the top, bottom, and/or within the core material itself. The concept here is that by providing an additional layer to the core, which is stiffer, a higher degree of rigidity would be imparted to the overall structural system of the sandwich panel (Mamalis, Spentzas, Pantelelis, Manolakos, & Ioannidis, 2008). Refer to Figure 2-9C.

Multilayer Core Systems refer to systems whereby the core is composed of multiple non-fibrous materials; perhaps multiple polymeric foam core structures of varying density. The implementation of different-density core structure in strategic positions within the core may allow for more efficient use of materials, and an overall improved core performance (Keller, Haas, & Vallee, 2008). Refer to Figure 2-9D.

Any panel constituting of a combination of two or more of the aforementioned core-strengthening techniques is referred to as a *Hybrid Core System*. Refer to Figure 2-9E.

Amongst such developments however, the implementation of a *Stiffened Core Material System*, a *Multilayer Core System,* or a combination of both, (thus forming a *Hybrid Core System)*, are identified to be the most promising. This was put forward by Manalo et al. (2016) from the fact that, solutions such as the *Intermediate Layer System* incur increased material costs, imparted from the large amount of material required in the implementation of the intermediate layer/s. The same was also true for *Corrugated Facing Sandwich Panels*, whose increased costs are a derivative of additional manufacturing processes (machining), and associated labour and material waste-generation (Manalo, Aravinthan, Fam, & Benmokrane, 2016).

Contrary to this, the implementation of the *Hybrid System* previously suggested, allows the use of cheap and low-strength core materials, and the adaptation of simple production processes. Both of which render H*ybrid Core Systems* cost effective systems that can be adopted.

This does not mean to imply that such *Hybrid Systems* are without fault. Notably, Kampner and Grenestedt (2007) point out that such panels tend to perform unfavourably under shock loads. This is suggested to be the case due to the stiff connection present between the stiffener and the top/bottom face sheets. This in turn may cause the stiffener to puncture the face sheets (Kampner & Grenestedt, 2007).

The next subsection highlighted recent developments in these areas, important observations, and findings, as it pertains to this dissertation. This served as the framework to this dissertation. However, it must be noted that this was predominantly discussed within the *Stiffened Core Material System* domain, as research pertaining to the use of *Multilayer Core Systems* was relatively scarce, even more so in the case of *Hybrid Core Systems*.

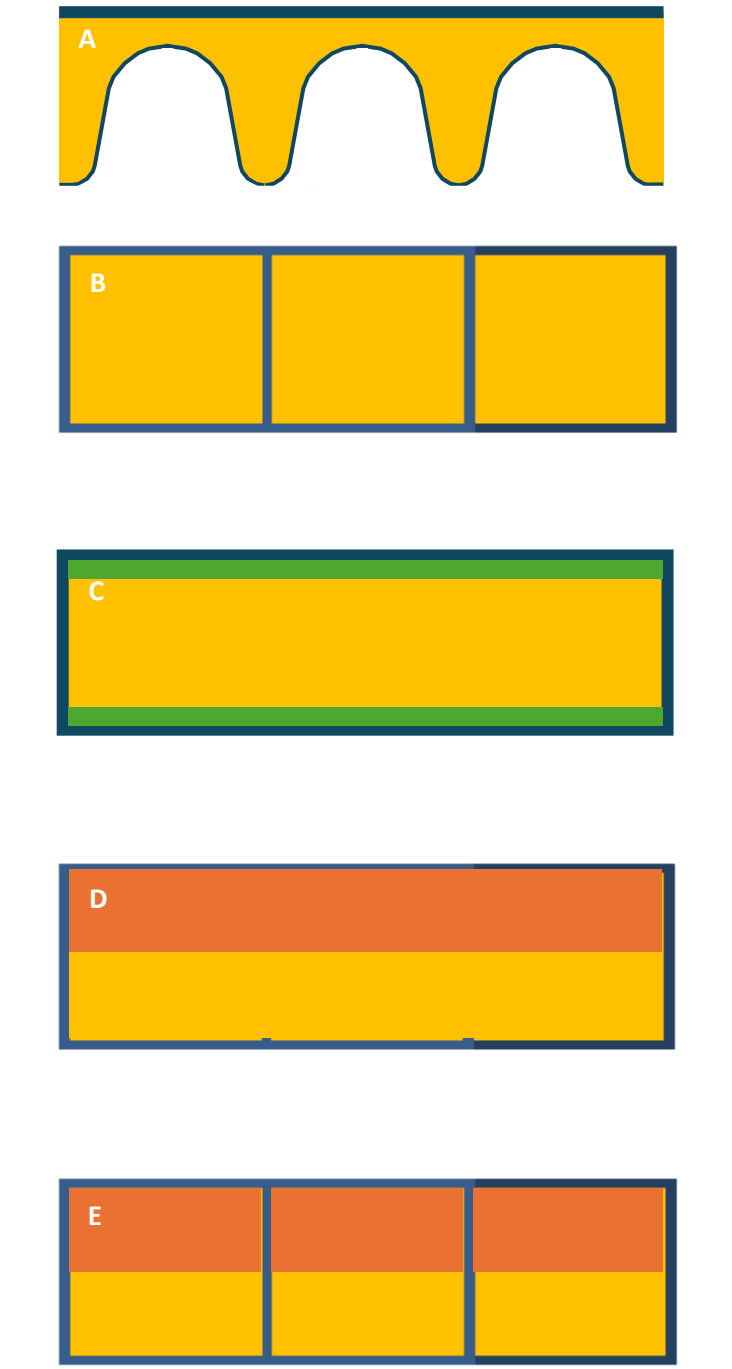

Figure 2-9: (A) Corrugated Sandwich Panel; (B) Stiffened Core Material System; (C) Intermediate Layer System; (D) Multilayer Core System; (E) Hybrid Core System (Mohamed, et al., 2015).

2.5.1. Core Material Development

To best illustrate the use and implementation of *Hybrid Core systems*, it is best to revert back to Keller's aforementioned project on the new Main Gate of the Novartis Campus in Basel, Switzerland. Here, Keller et al. (2018), successfully designed and installed a GFRP sandwich roof structure, by adopting a hybrid approach; that is through the use of mixed-density polyurethane foams, and orthogonal GFRP stiffeners (Keller, Haas, & Vallee, 2008). The need in opting for a hybrid system was derived as a result of the large variations in shear acting on the roof structure. In total, three different types of polyurethane foams were used. This was however still noted to be insufficient. As a result, this led to the implementation of a system of orthogonal stiffeners. Figure 2-10 exhibits a view of the concerning hybrid roof structure in section (Keller, Haas, & Vallee, 2008).

The thickness of such stiffeners varies, with the largest noted to be 9 mm. This was approximately 85% the thickness of the thickest portion of the facesheets (T_{Ft}). This was noted to be in excess to that recommended in Arruda & Lopes' study, suggesting that the optimal stiffener thickness was $0.7T_{Ft}$ (Arruda & Lopes, 2020).

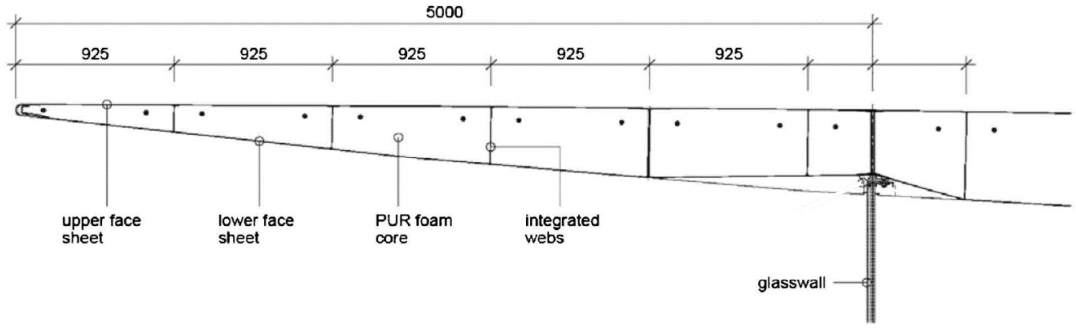

Figure 2-10: Hybrid GFRP sandwich roof panel (Keller, Haas, & Vallee, 2008).

Maintaining the same design philosophy, Manjusha et al. investigated the effects of different stiffener systems within a multilayer core configuration (Manjusha & Althaf, 2020). The three stiffener systems studied were: a) trapezoidal, b) rhombic, and c) sinusoidal. These stiffener designs are shown in Figures 2-11A – C. Note that although not specified, in the case of the trapezoidal and rhombic stiffener configuration, the angle subtended by the stiffener was noted to be around 45° with respect to the horizontal plane. From the study, the sinusoidal system outperformed its counterparts, exhibiting the least total deformation at its midspan. This was suggested to have occurred due to a higher GFRP volume percentage present within the panel. Both the trapezoidal and rhombic systems performed similarly suggesting that this may have occurred as a result of both systems being similar in GFRP volume percentage (Manjusha & Althaf, 2020). However, it must be noted that the implementation of a sinusoidal stiffener system may be impractical, proving to be costlier to produce in terms of the additional fibre-content required, increased workmanship, and overall higher degree of difficulty presented by the curvilinear elements. Perhaps it was for these reasons that research on

stiffener systems has been predominantly focused on more streamlined designs. For this reason, it is to the interest of this dissertation that focus was to be placed on streamlined stiffening designs.

An example of such can be taken from a study conducted by Mohamed et al. (2015), who, similarly as in the previous case, attempted to strengthen the core of a composite sandwich panel through a system of trapezoidal stiffeners, and additionally, a system of orthogonal stiffeners. These are shown in Figures 2-11i - ii, and are denoted as *Types 2* and *3*, respectively. The difference between the two systems was the angle subtended by the stiffener with respect to the horizontal plane. The angle of the stiffeners with respect to the horizontal for the orthogonal system was noted to be 90^{o}, while for the trapezoidal system, although unspecified, this was noted to be in the region of $60^{0} – 90^{0}$. Comparisons of such systems were conducted with respect to an unstiffened panel. This was denoted as *Type 1*, Figure 2-11iii. From the results obtained, the trapezoidal system outperformed its counterparts, exhibiting a fourfold shear core strength increase, as shown in Figure 2-12. This was attributed to the implementation of shear layers embedded between the trapezoid sections (Mohamed, et al., 2015).

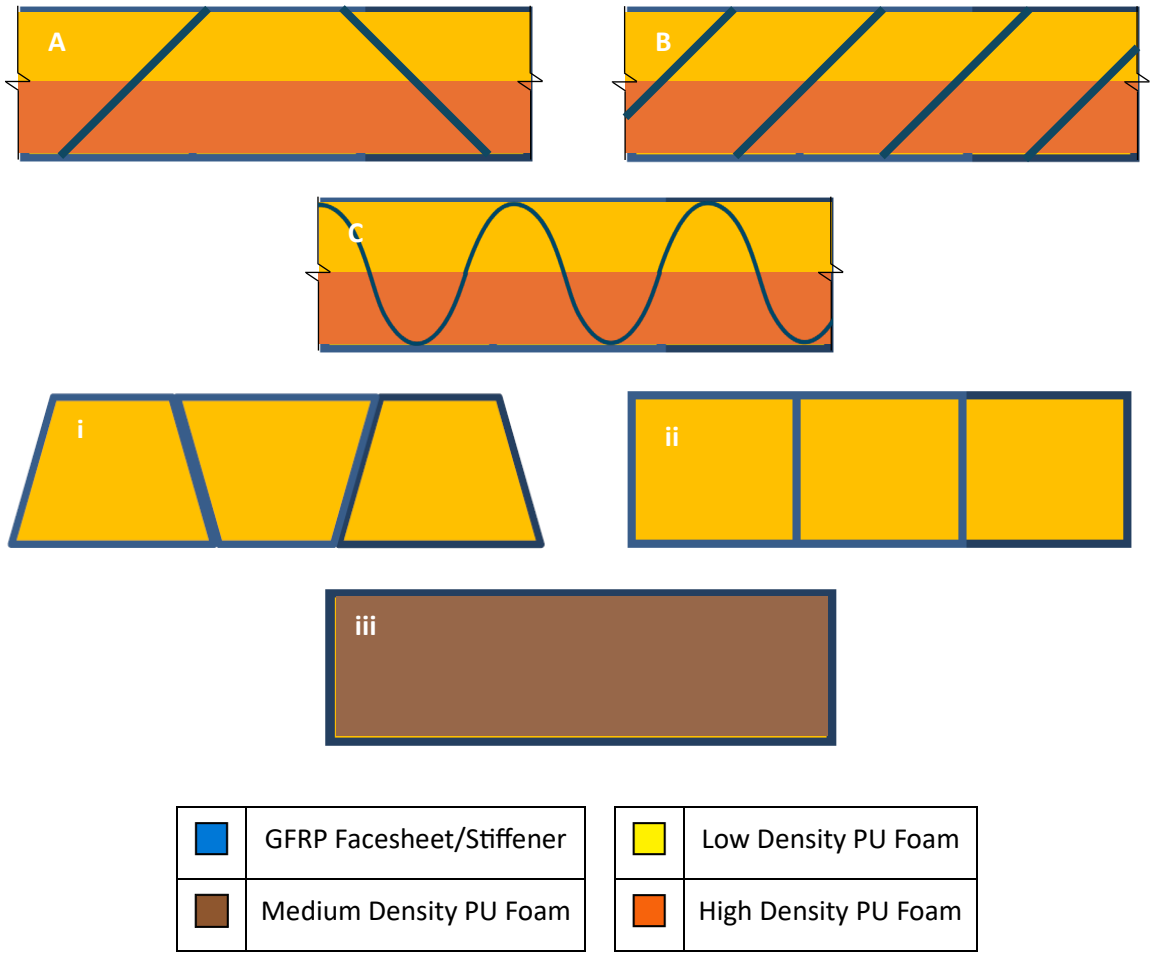

Figure 2-11: Stiffener configurations; (A) Trapezoidal ($\vartheta \approx 45^{o}$); (B) Rhombic ($\vartheta \approx 45^{o}$); (C) Sinusoidal; (i) Trapezoidal *($60^{o} < \vartheta < 90^{o}$); (ii) Orthotropic; (iii) Unstiffened, (Mohamed, et al., 2015).*

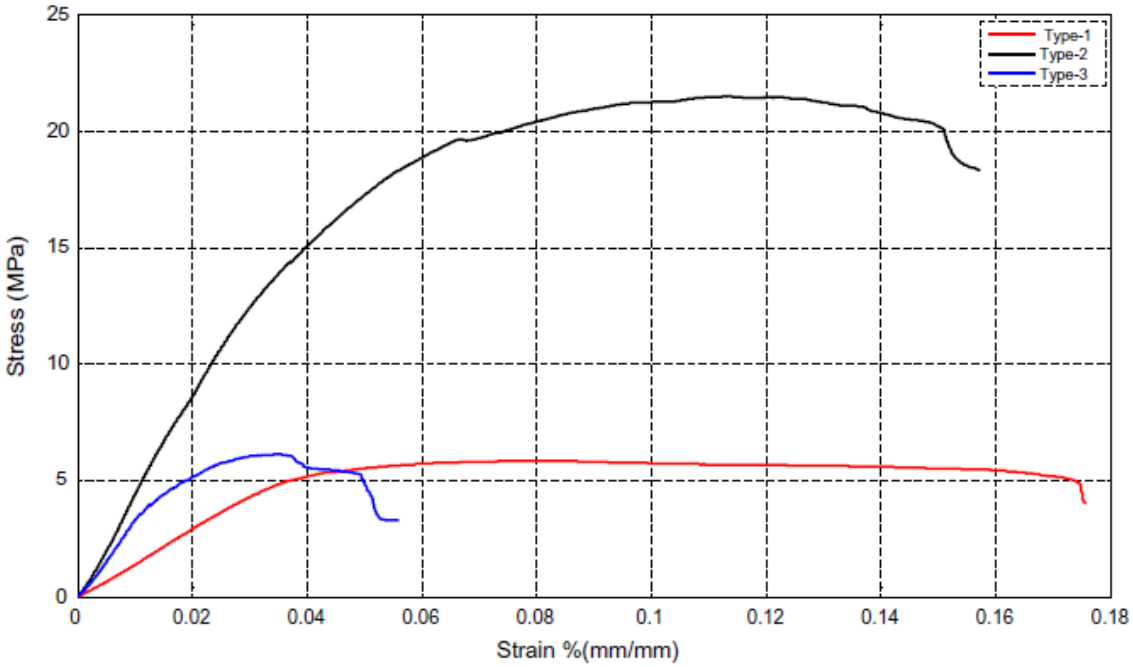

Figure 2-12 Stress-strain graph for; an unstiffened GFRP panel (Type 1 – RED); a trapezoidal-stiffened GFRP panel (Type 2 – BLACK); an orthogonally-stiffened GFRP panel (Type 3 – BLUE), (Mohamed, et al., 2015).

Comparing the Von-Mises stress contours derived from computer simulation of a three-point-bend test, it was identified that in the case of the trapezoidal system, for an applied load equalling to a total displacement of 2.2 mm, maximum Von-Mises stresses of 0.12 MPa, and 168.6 MPa, were identified in the foam core, and the stiffener, respectively. Refer to Figures 2-13A and B, respectively. This implied that for such a system, the trapezoidal stiffener was predominantly responsible in taking on the load being applied. Similarly, the orthogonal stiffener system was also identified to outline the same type of behaviour, albeit a smaller contribution was provided by such stiffeners. Refer to Figure 2-13C (Mohamed, et al., 2015).

The same concept was further supported in Kampner and Grenestedt's study (2007). Here, simulations conducted on a corrugated sandwich panel revealed that the corrugated face sheets contributed in carrying a portion of the shear load. This allowed for slimmer sandwich panels to be developed (Kampner & Grenestedt, 2007).

These findings therefore led to the understanding that for a stiffening system to have an appreciable effect on the shear resistance of a sandwich system, the implemented shear layers are best to be designed not following an orthogonal system.

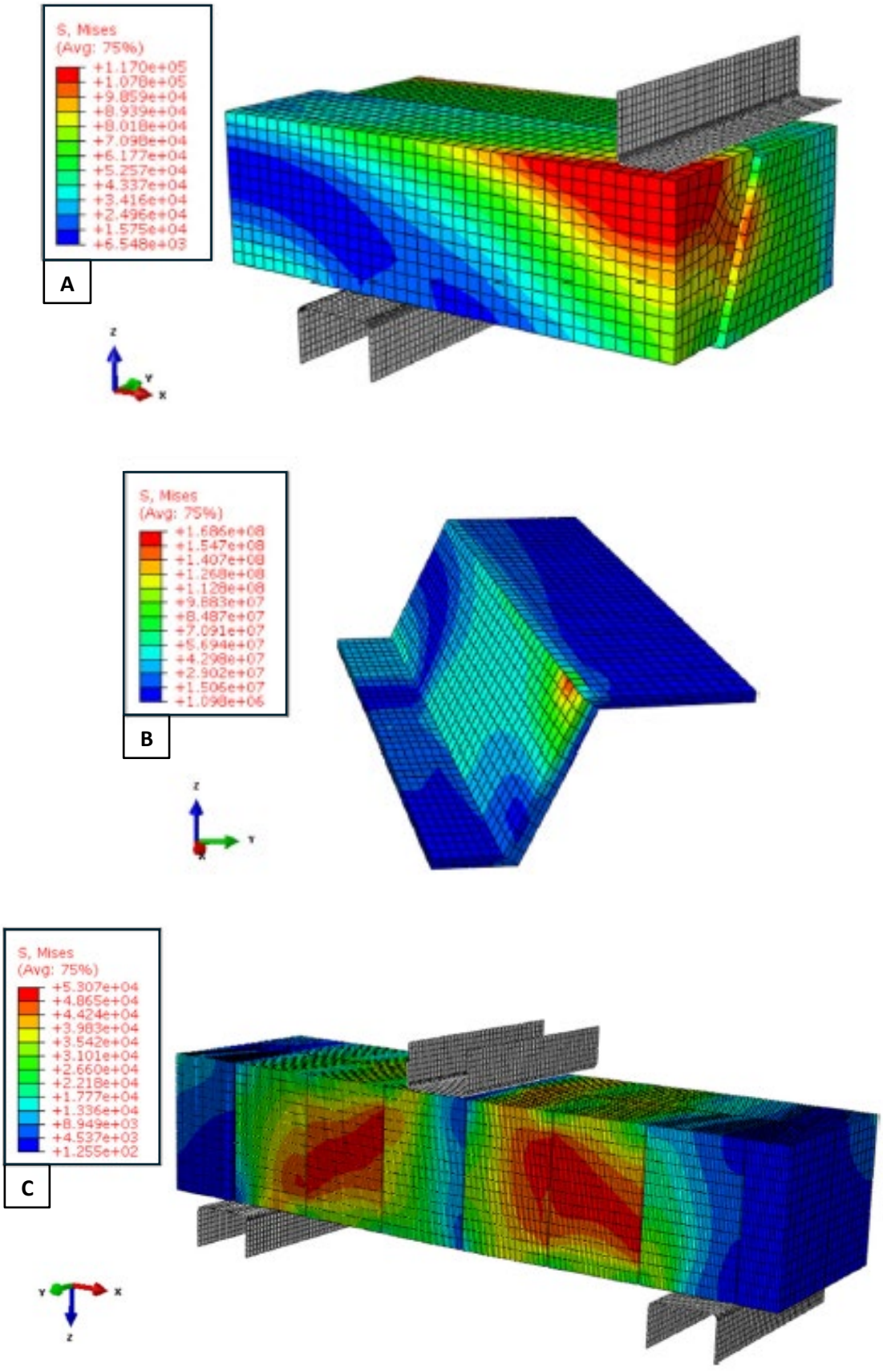

Figure 2-13: Von-mises stress contours for: (A) Trapezoidal-stiffened core; (B) Trapezoidal-stiffener; (C) Orthogonally-stiffened GFRP panel, (Mohamed, et al., 2015).

Similarly, Fam et al. studied the effects of orthogonal stiffeners, having different configurations within a GFRP sandwich panel. Such stiffener configurations included varying combinations of longitudinal and/or transverse stiffeners (at mid-point), and/or bordering stiffeners. These are summarized in Figure 2-14, along with any of their associated detailing. From the tested configurations, configuration *P5* (configuration consisted of a longitudinal stiffener at midpoint, and at all 4 borders) exhibited the largest failure load, an increase of 140%, relative to *P1* (configuration did not constitute of any stiffening measures). Refer to Figure 2-15. The effects imparted by the stiffening system on the foam core (having a density of 31.6 kg/m^3) in *P5* was identified to be equivalent to an unstiffened system, having a foam core, whose density was doubled (i.e. 64.2 kg/m^3), implying greater weight-savings (Fam & Sharaf, 2010). In cases configurations *P2* and *P3*, and *P5* and *P6*, the addition of a transverse stiffener was noted to have gone unnoticed. This was exhibited from the insignificant percentage increase in failure load observed. This behaviour was suggested by Fam & Sharaf to be owed to the one-way bending nature of the panel (Fam & Sharaf, 2010). This implied that the design of a stiffening system for the purposes of a one-way slab, was to be most effective if such stiffeners were designed in the longitudinal direction.

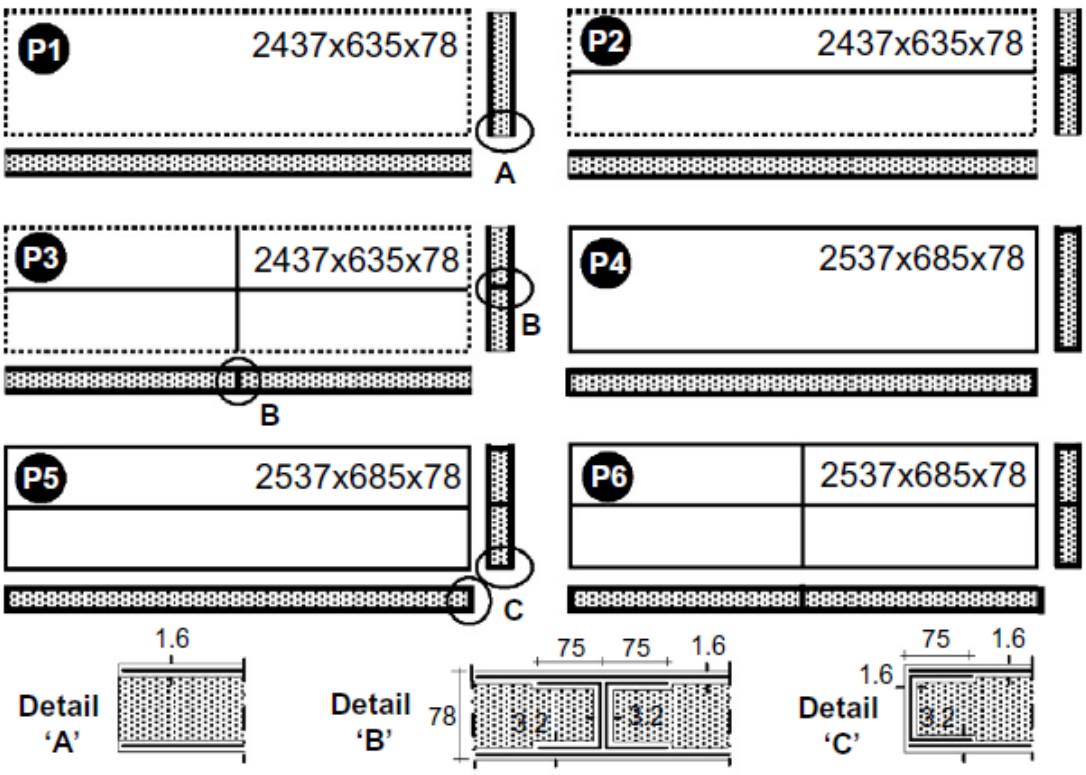

Figure 2-14: Schematic of all stiffener configurations tested (P1 – P5), along with any associated detailing, (Fam & Sharaf, 2010).

When considering Figure 2-15, it was identified that for all configurations, the total deflection varied linearly as the load increased. This was in alignment to Keller's (2008) observations, who additionally identified that such linearity was predominantly maintained on unloading the specimens (Keller,

Haas, & Vallee, 2008). In all cases, the maximum allowable deflection for a simply supported member, typically requested in most design codes, $\left(\frac{span}{360}, \frac{span}{180}\right)$, was exceeded very much before failure of the panel occurred (Fam & Sharaf, 2010). The implication of this was twofold. The first was that, satisfying the maximum allowable deflection criteria would result in a large strength safety factor. Secondly, it implied that stiffness was the governing factor in the design of sandwich panels. This meant that panel failure was a function of vertical deflection. This approach was adopted in (Manjusha & Althaf, 2020)

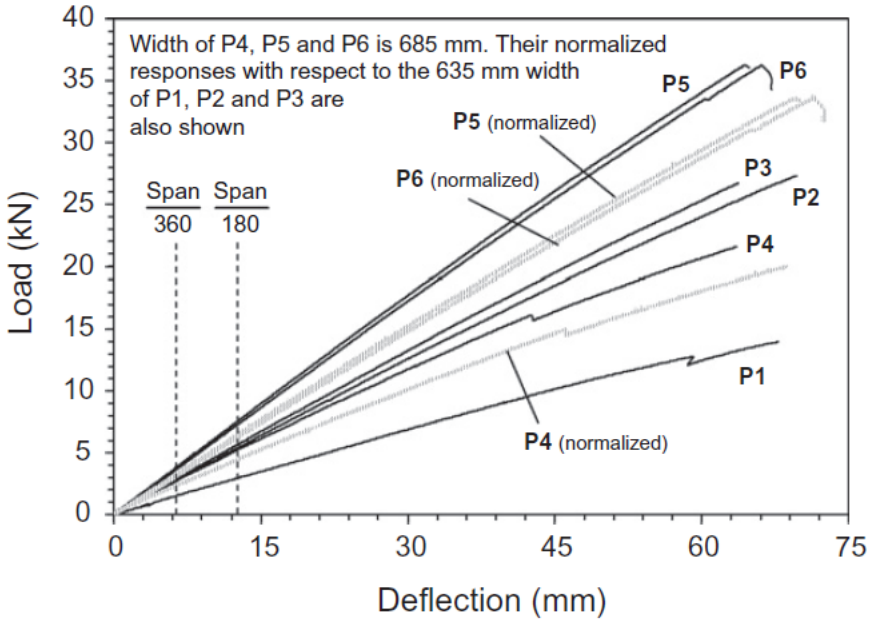

Figure 2-15: Graph of load-deflection for all tested specimens. Indicated are also typical deflection control limits, (Fam & Sharaf, 2010).

Studies in this regard were noted to go beyond the analysis of different stiffener geometries and their effects on a GFRP sandwich panel. There are many parameters that make up a stiffener system. As a result, studies have also focused on other qualities making up a stiffener system, such as its spacing. In a study conducted by Sharaf et al. (2015), the effects of stiffener spacing on the ultimate bending capacity of a sandwich panel were examined. From such study, it was determined that for a panel, 685 mm in width, and 78 mm in height, no significant improvements were noted in implementing more than two longitudinal stiffeners. This is shown in Figure 2-16, within which *S-new 1* and *S-new 2*, denote the previously described configuration *P5*, alternatively having two, and three, longitudinal stiffeners, respectively. From such study, the authors therefore suggested an optimal stiffener spacing to thickness ratio of 2.93 (Sharaf & Fam, 2015)**.** This ratio was found to be in excess to that adopted in Keller's design, who opted for a more conservative ratio of 1.5 (Keller, Haas, & Vallee, 2008).

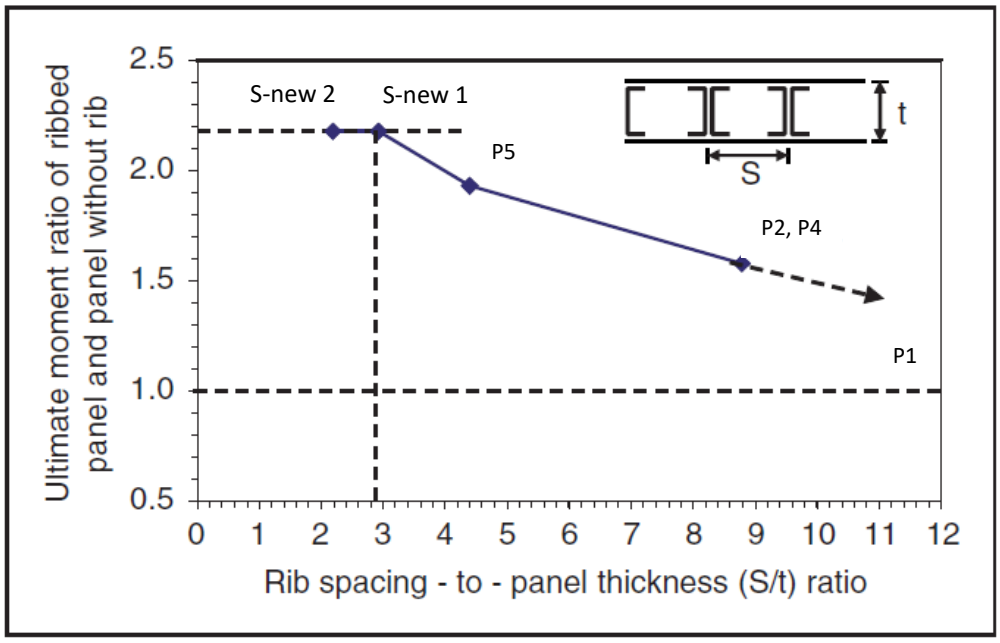

Figure 2-16: Graph of ultimate moment ratio of ribbed panel (P2, P4, P5, S-new 1, and S-new 2) and panel without rib (P1) vs rib spacing-to-panel thickness (Sharaf & Fam, 2015).

As mentioned earlier, aside from the implementation of an orthogonal stiffener system, in their study, Keller et al. strategically made use of polyurethane foam cores, whose density varied throughout the design of the roof panel (Keller, Haas, & Vallee, 2008). The concept of using foam cores in this manner has been studied by Kampner and Grenstedt. For illustration purposes, such study highlighted the application of such a concept to a simply supported beam, acting upon by a uniformly distributed load. Here, regions of high shear were identified to be present closer towards the supports of the beam, thus suggesting the use of high-density foams, exclusively for such regions. Refer to Figure 2-17. Doing so yielded an efficient use of materials, rendering a beam which was stronger, and lighter, relative to a thicker beam, composed entirely of a lower-density foam (Kampner & Grenestedt, 2007).

In a study conducted by Manjusha and Althaf, a similar concept was explored, whereby a multilayer core system was designed to vary over its height, as opposed to its length, as in Kampner and Grenstedt's study. In this regard, Manjusha and Althaf sought to identify the best material configuration for a bilayer core system using different grades of polyurethane foams. Four different configurations were considered. These are denoted by *A* – *D*, and are depicted in Figures 2-18A – D. The best performing configuration (i.e. the system which exhibited minimal vertical deformation), was identified to be configuration *B*, constituting of a low-density polyurethane top-layer, and a high-density polyurethane bottom-layer. This exceeded the worst-performing configuration, *A*, by approximately 4% (Manjusha & Althaf, 2020). This therefore suggested that for a simply supported bilayer GFRP sandwich panel in flexure, the core configuration that would yield optimal performance was to consist of a low-density polyurethane top-layer, and a high-density polyurethane bottom-layer.

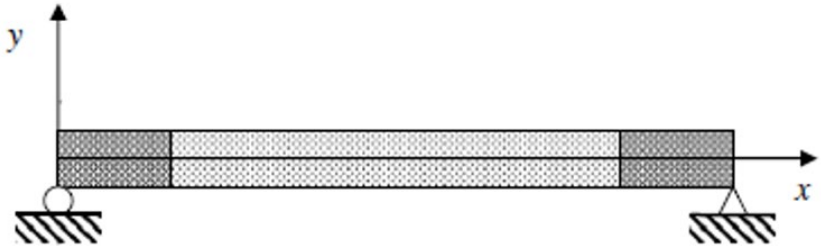

Figure 2-17: Illustrates the use of a multiple cores for a simply supported beam, on the basis of variation in shear. This dictates that denser cores (DARK GRAY) are needed at the supports, (Kampner & Grenestedt, 2007).

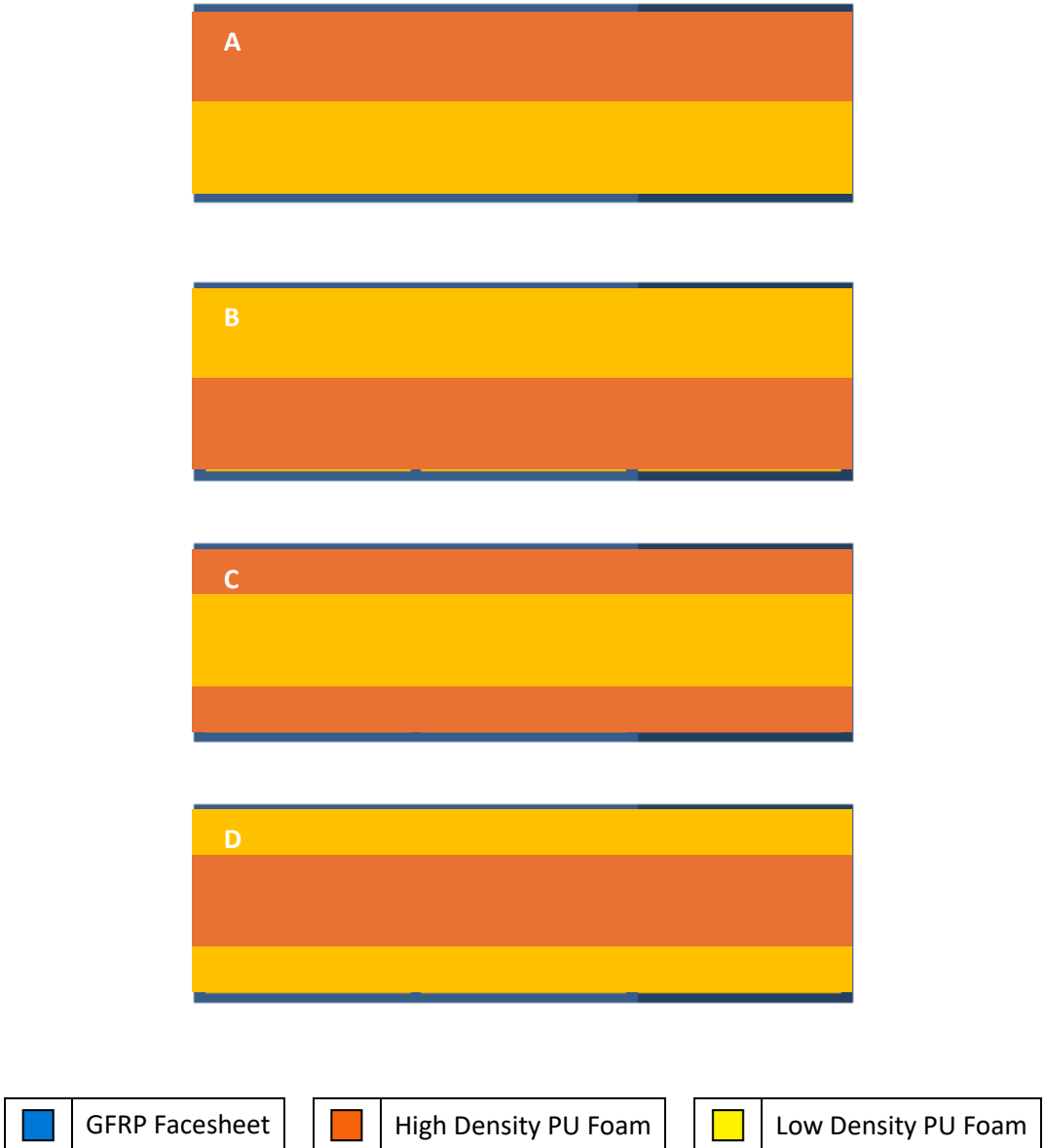

Figure 2-18: Different foam core configurations tested in (Manjusha & Althaf, 2020).

2.6. Concluding Remarks

In closing this chapter, key points pertaining to the direction of this dissertation were highlighted. As discussed within S*ection 2.4* sandwich panels have a wide range of application within civil engineering activities. In this regard, it was of the purpose of this dissertation to further contribute to the application of sandwich panels as building floors within domestic buildings. As in Correia, Garrido, Gonilha, & Branco (2012), focus was placed in optimizing the behaviour of sandwich panels as a monolithic slab system.

As described in *Section 2.5.1*, owing to the promising results derived via stiffened core material systems, and multilayer core systems, this dissertation sought to focus on this type of hybrid system. In particular, this dissertation sought to conduct a multi-objective optimization whereby a standard-sized (3 m by 1 m) trapezoidally stiffened bilayer sandwich panel was optimized in terms of vertical deflection, panel mass, and material cost. This was to be done with respect to variations in; the stiffening system's angle; the thickness of the facesheets, and; the thickness of the bilayer core.

Range of values pertaining to the input parameters, and associated step size to be investigated are exhibited in Table 2-1. Note that the range of; the facesheet thickness was defined on the basis of economic viability; the core thickness was based on the total thickness of traditional flooring solutions (≈150 – 200 mm), and the aspiration in achieving slimmer sections, and; the angle of the trapezoidal stiffening system was set up on the basis of geometric constraints.

Note that analysis was to be done through finite element analysis.

Table 2-1: Input variables and their associated range and step size.

Input Variable	**Range**		**Step Size**
	Lower Bound	**Upper Bound**	
Facesheet Thickness [mm]	1.2	4.0	0.4[iii]
Core Thickness [mm]	50	100	10
Stiffener System Angle [degree]	50	130	10

In this regard, as per *Section 2.5.1*, this dissertation aimed to adopt the use of a GFRP trapezoidal stiffening system and GFRP facesheets. Additionally, due to the one-way bending nature of the panel, the fibres of the GFRP components were aligned in the longitudinal direction, in alignment to the panel's span direction. Additionally, based on the findings by Manjusha & Althaf (2020), a bilayer core of low- and high-density PU foam was incorporated into the panel. In this manner, the cores were to

[iii] This is equivalent to the thickness of one ply.

be of equal thickness, and on the basis of the same study, the high-density core was to be situated on top of the bottom facesheet.

Note that the adoption of such materials was primarily a function of economy. Relevant material properties were extracted from Manjusha & Althaf's (2020) study.

The stiffener design guidelines highlighted in *Section 2.5.1.* were summarized in Table 2-2. These were followed in generating the design of the trapezoidal stiffening system for the GFRP sandwich panel sought to be optimized in this dissertation.

In designing the trapezoidal stiffening system, it was determined that an even number of stiffeners was required. To ensure the sandwich panel was neither over-stiffened nor under-stiffened, guideline #4 was applied using a median core thickness of 75 mm. This resulted in a stiffener spacing of approximately 220 mm (2.93 x 75 mm), corresponding to 5 stiffeners. However, due to the requirement for an even number of stiffeners, the system was adjusted to include 6 stiffeners. To ensure proper connectivity between adjacent panels, the edge stiffeners were constrained to an angle of 90^{o} with respect to the horizontal plane.

Table 2-2: Shear stiffening system design guidelines summarized from Section 2.5.1.

#	Guideline		Reference
1	Streamlined Design		(Manjusha & Althaf, 2020)
2	Non-Orthogonal		(Kampner & Grenestedt, 2007; Mohamed, et al., 2015)
3	Longitudinal		(Fam & Sharaf, 2010)
4	Optimal Stiffener Spacing-Thickness Ratio	2.93	(Sharaf & Fam, 2015)
5	Optimal Stiffener Thickness	$0.7T_{Ft}$	(Arruda & Lopes, 2020)

Such guidelines yielded the hybrid GFRP sandwich panel design shown in Figure 2-19. In this figure, numbers *#1 - #5* indicated the core identification, while letters *A – F* denoted the stiffener.

Owing to similarities between Manjusha & Althaf's (2020) study, and this dissertation, the next chapter commenced by undertaking a preliminary study (*Section 3.1*) that served to establish the basic methodology to be followed. The second potion of the chapter (*Section 3.2*) adopted and developed the same methodology in ultimately determining the optimal hybrid sandwich panel configuration for the purposes of an alternative slab solution within domestic buildings.

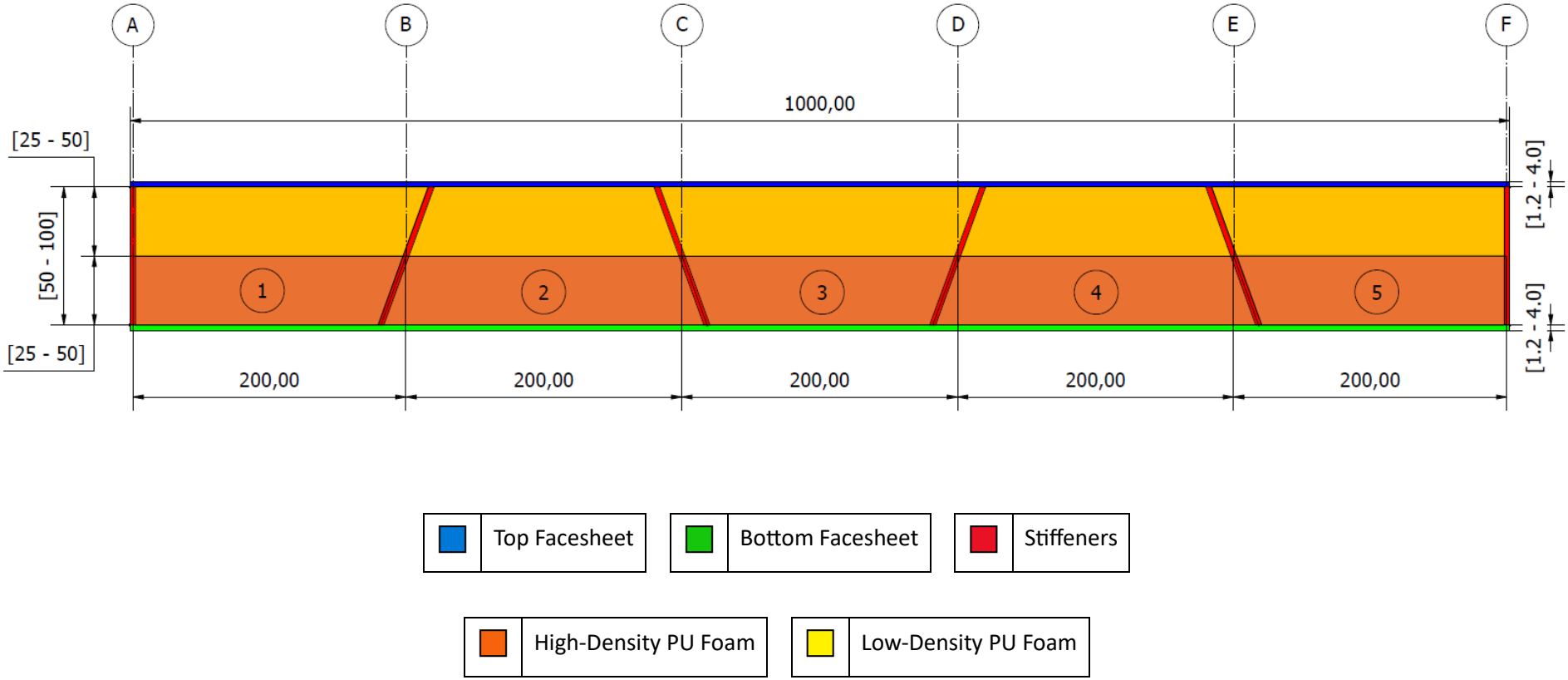

Figure 2-19: Design of the standard-sized, trapezoidally stiffened GFRP sandwich panel with a bilayer core. Dimensions are in mm

3. Methodology

To optimize the trapezoidally-stiffened GFRP sandwich panel and determine how the input variables affected the panel's vertical deflection, mass, material cost, and Von Mises stresses, a two-step process was employed. This approach was detailed in the two main sections of this chapter: *Section 3.1* and 3.2. The first section provided a detailed account of a preliminary study aimed to establish a methodology for developing a numerical model for a GFRP sandwich panel. The second section adapted this methodology to the trapezoidally-stiffened GFRP sandwich panel designed, detailing the steps taken to determine the relationship between input and output variables, and identify the optimal panel configuration.

3.1. Preliminary Study

In establishing the basic methodology that would allow for numerical analysis of a GFRP sandwich panel to be achieved, a preliminary study was first conducted. In this regard, Manjusha et al.'s study (2020) was re-simulated, albeit not in its entirety. For the purposes of this study, attention was given to the case shown in Figure 3-1. Successful implementation of the methodology conducted by Manjusha et al. (2020) was noted to have been achieved only if a discrepancy of smaller or equal to 5.00% was noted to have been present between the result of this study, and the published study.

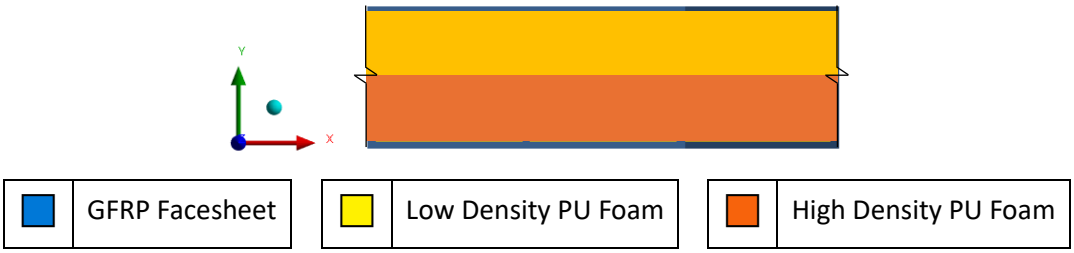

Figure 3-1: GFRP sandwich panel chosen for the preliminary study.

The flowchart shown in Figure 3-2 summarizes the methodology followed in conducting numerical analysis on the sandwich panel shown in Figure 3-1.

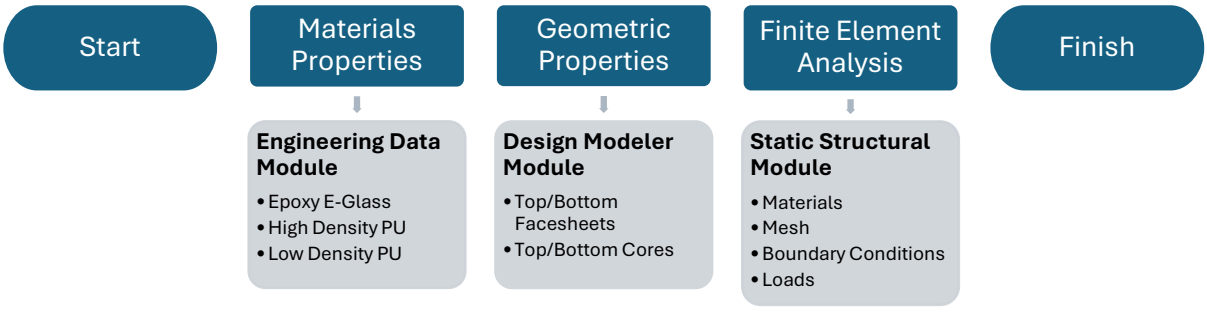

Figure 3-2: Flowchart summarizing the methodology adopted in conducting the preliminary study.

3.1.1. Material Properties

First, the material properties of the GFRP sandwich panel were defined using the *Engineering Data* module. These included three materials: epoxy e-glass woven fabric, high-density polyurethane (PU) foam, and low-density polyurethane (PU) foam. As described in Manjusha et al.'s study (2020), the fabric material was modelled as an orthotropic elastic material due to its orthotropic nature. Following the same study, the foam materials were modelled as isotropic elastic materials. However, as discussed in *Section 2.2*, it must be noted that this approach was not entirely representative of the nonlinear viscoelastic behaviour associated with polyurethane foams. Table 3-1 and Table 3-2 summarize the material properties of such materials (Manjusha & Althaf, 2020).

Table 3-1: Mechanical properties of e-glass woven fabric (Manjusha & Althaf, 2020).

Epoxy E-Glass Woven Fabric Material Properties	
Density (ρ_{FRP}) [kg/m^3]	2000
Young's Modulus; 1-Axis (E_{11}) [GPa]	45
Young's Modulus; 2-Axis (E_{22}) [GPa]	10
Young's Modulus; 3-Axis (E_{33}) [GPa]	10
Poisson's Ratio; 12 (v_{12})	0.3
Poisson's Ratio; 23 (v_{23})	0.4
Poisson's Ratio; 13 (v_{13})	0.4
Shear Modulus; 12 (G_{12}) [GPa]	5
Shear Modulus; 23 (G_{23}) [GPa]	3.846
Shear Modulus; 13 (G_{13}) [GPa]	5

Table 3-2: Mechanical properties of low- and high-density PU foams adopted from (Manjusha & Althaf, 2020).

	Low-Density PU Foam	**High-Density PU Foam**
Density [kg/m^3]	31.9	192
Young's Modulus [MPa]	2.1	66.1
Poisson's Ratio	0.279	0.316
Shear Modulus [MPa}	0.82	25.114

3.1.2. Geometric Properties

Next the geometry of the GFRP sandwich panel needed to be defined. Refer to Table 3-3.

Table 3-3: Geometric properties of the selected bilayer GFRP sandwich panel from Manjusha & Althaf's study (2020).

Span			3 m		
Width			1 m		
Thickness	**Top Facesheet**		2 mm	**# of Plies**	5
				Ply Orientation	0°
	Core	**Top Layer**	35 mm		
		Bottom Layer	35 mm		
	Bottom Facesheet		2 mm	**# of Plies**	5
				Ply Orientation	0°

In defining the geometry of the GFRP sandwich panel, *ANSYS' DesignModeler* was used. In this manner the GFRP sandwich panel was drawn in section, through a total of 4 sketches. Each sketch was dedicated to a particular component (top facesheet, top core, bottom core, and bottom facesheet) making up the GFRP sandwich panel. This is shown in Figure 3-3. Note that the top and bottom facesheets were not assigned to a geometric thickness. The purpose of this was to then allow the *extrude* function to generate the facesheets as surface bodies, as opposed to solid bodies. More on the importance of such distinction is provided later, on the topic of *meshing*.

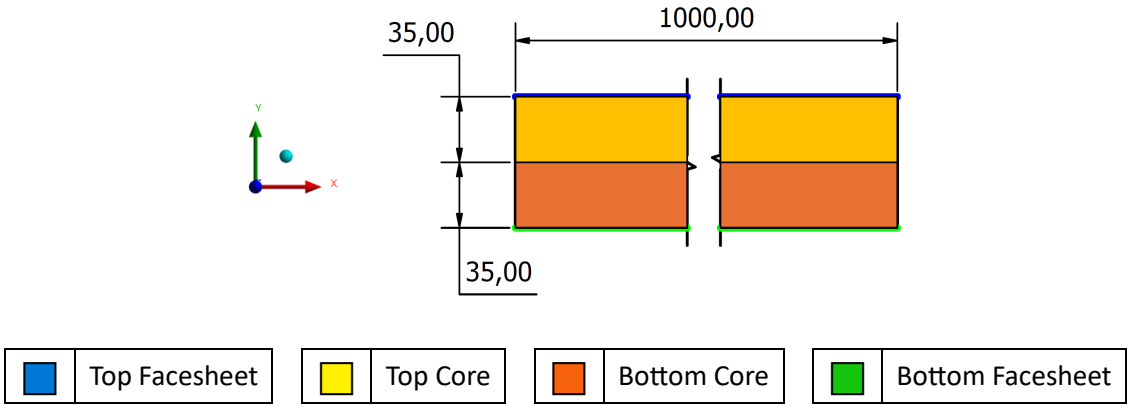

Figure 3-3: Geometry of GFRP sandwich panel was comprised of 4 independent sketches; top facesheet, top core, bottom core, bottom facesheet. Note that dimensions are in mm.

In adapting the aforementioned 2D sketches to a 3D environment, the *extrude* function was adopted in the z-axis. All bodies were extruded to 3000 mm. Extruding the top and bottom facesheets allowed for surface bodies to be generated. Extruding the core sketches allowed for solid bodies to be generated. Therefore, in total 4 bodies were noted to have been generated.

For the purposes of achieving mesh continuity, such bodies were defined as a *singular part*. This allowed for the *share topology* function to be applied to the system of components, thus allowing the program to interpret the individual components as one single entity. Note that this was only made possible as a result of a mating surface present between adjacent components. This allowed for subsequent *manual contact operations* within the *Static Structural* module to be avoided.

3.1.3. Finite Element Analysis

Next, the *Static Structural* module within *ANSYS Workbench* was considered. Within such module links were first created between the previously discussed *Engineering Data* module, and the *Geometry* module. In this regard, both the top and bottom facesheets were attributed the material properties of *epoxy e-glass woven fabric.* Additionally, they were also assigned a 2 mm thickness. The top and bottom cores were linked to the material properties of *low-density PU foam,* and the *high-density PU foam*, respectively.

In Manjusha et al.'s (2020) study, two different types of mesh elements were used in setting up the mesh. Shell elements were used in modelling the facesheets owing to a relatively large length-to-thickness ratio $\left(\frac{3000\ mm}{2\ mm} = 1500\right)$ and breadth-to-thickness ratio $\left(\frac{1000\ mm}{2\ mm} = 500\right)$. This was argued by Manjusha et al. (2020) to provide greater computational savings. The specific shell element used in modelling the facesheets was *shell 181;* a 4-node element with six degrees of freedom at each node: both translations and rotations along the x-, y-, and z-axes (ANSYS, Inc., 2011).

Solid elements were used to mesh the core components. As per Manjusha et al. (2020), these were chosen in favour of shell elements due to the relatively smaller length-to-thickness ratio $\left(\frac{3000\ mm}{70\ mm} = 43\right)$ and breadth-to-thickness ratio $\left(\frac{1000\ mm}{70\ mm} = 14\right)$. In this regard, the core components were meshed using *solid 186* elements; a 20-node solid element having three degrees of freedom per node: translations in the nodal x-, y-, and z-axes (ANSYS, Inc., 2011).

The application of the selected elements onto the geometric model was achieved through the *sweeping method*. The mesh was therefore generated by sweeping the profile along the span of the sandwich panel. This method of meshing was identified as being the most suitable method as a result of the associated model being extrudable.

Note that for further information pertaining to the difference between the different element types, and alternative potential methods of meshing, refer to *Appendix A.1*.

Next, the quality of the mesh was examined. In examining the quality, it was desirable for all the elements to coincide with their ideal form. This would allow numerical instabilities to be avoided within the numerical model (ANSYS, Inc., 2023). For this study, the ideal forms were a square for *shell181* elements and a tetrahedron for *solid186* elements. The element quality metric was applied to measure how closely each element matched its ideal form. This metric provided a score from 0 to 1, with 1 representing elements in their ideal form and 0 representing elements far from their ideal form. Further details pertaining to the theory behind such metric can be found in *Appendix A.1 – Element Quality Metric*.

In this manner, meshes with an average element quality less than 0.90 were discarded. This restriction resulted in an initial mesh size of 50 mm, as shown in Figure 3-4. This mesh size corresponded to an average element quality of ≈ 0.93.

Following, a simply supported panel was modelled, where pinned and roller conditions were given to the opposite short ends of the bottom facesheet. For the pinned end, this meant that translational movement was prohibited to occur in the orthogonal axis. Although this, rotations were allowed to take place about the x-axis. For the rolled end, translational movement was only allowed to take place within the z-axis. Additionally, such end also allowed rotations to occur about the x-axis.

Two different types of loads were applied; *standard earth gravity*, and *area load*. *Standard earth gravity* was applied to the system, globally. This was set to act in the negative y-axis, at 9.8066 m/s^2. The *area load* was applied only to the top facesheet. In Manjusha et al.'s study (2020), this was set to a magnitude of 0.75 kN/m^2, with the purpose of simulating a roof load.

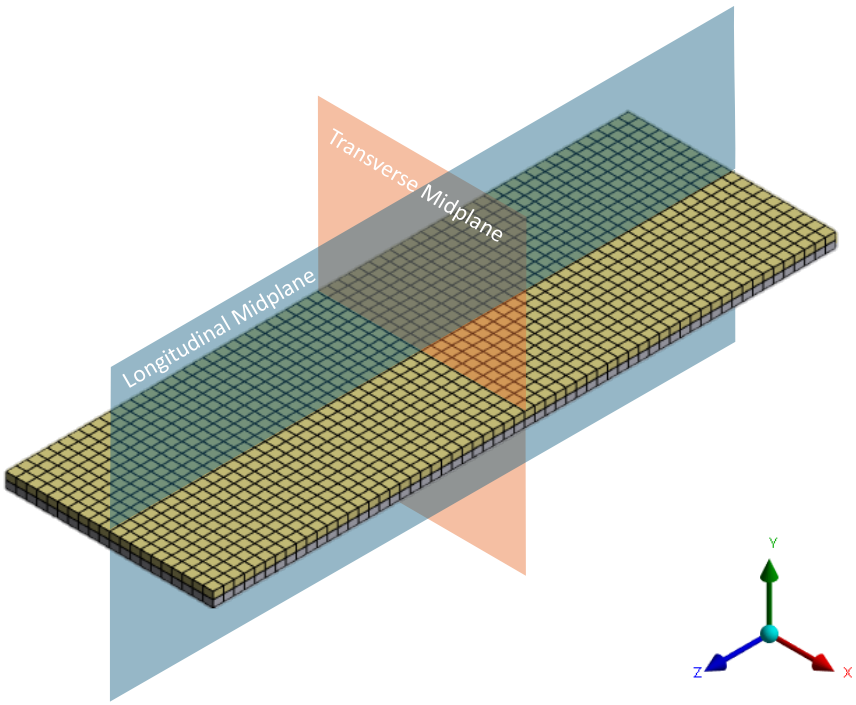

Figure 3-4: Isometric view of the initial mesh set up.

Next, the simulation was conducted. The resulting vertical deflection contour is depicted Figure 3-5. In this context, two sets of vertical downward deflection curved were observed. These curves reached their maximum values along the longitudinal midplane and the transverse midplane. The deflections recorded were 11.257 mm, and 11.718 mm, respectively, with the latter corresponding to the maximum vertical downward deflection exhibited by the panel. This occurrence was attributed to the panel's orthotropic properties. Although bidirectionality was observed, it was noted that the panel predominantly behaved unidirectionally. This was evidenced by the predominance of vertical deflection along the longitudinal plane.

Cross-referencing this to Manjusha's (2020) study, it was not specified which value of deflection was being referenced, be it the maximum deflection along the longitudinal plane, or the transverse plane. Therefore, it was assumed that the quoted deflection referred to the maximum vertical deflection along the longitudinal plane. This assumption was based on the predominant occurrence of deflection along this plane. As well as the fact that it was noted that the difference in vertical deflection along the longitudinal plane (- 0.88%), compared to Manjusha's study, was smaller than the difference in vertical deflection along the transverse plane (+ 1.03%).

In ensuring the validity of the maximum deflection at the longitudinal midplane, mesh refinements were conducted until convergence was noted to occur within the deflection values. Convergence was identified to occur when the change in deflection was less than ± 2.00%. In this regard, convergence occurred after one iteration which corresponded to an element size of 48 mm, and an average element quality of 0.97. The converged vertical downward deflection value was that of 11.258 mm. The change in deflection, calculated with respect to the penultimate vertical deflection, was noted to be (+) 0.0089% $\left(= \left(\frac{(-)11.258}{(-)11.257} - 1\right) * 100\right)$.

The final value of deflection was compared to that obtained in Manjusha et al.'s study (2020). Here, a change in vertical deflection of (-) 0.87% $\left(= \left(1 - \frac{(-)11.258}{(-)11.357}\right) * 100\right)$ was identified to be present. The discrepancy was noted to be less than 5.00%, therefore ensuring that the basic methodology adopted by Manjusha et al. (2020), was correctly established in this study. Note that result pertaining to the ultimate mesh size (= 48 mm) may be found in *Appendix A.2*.

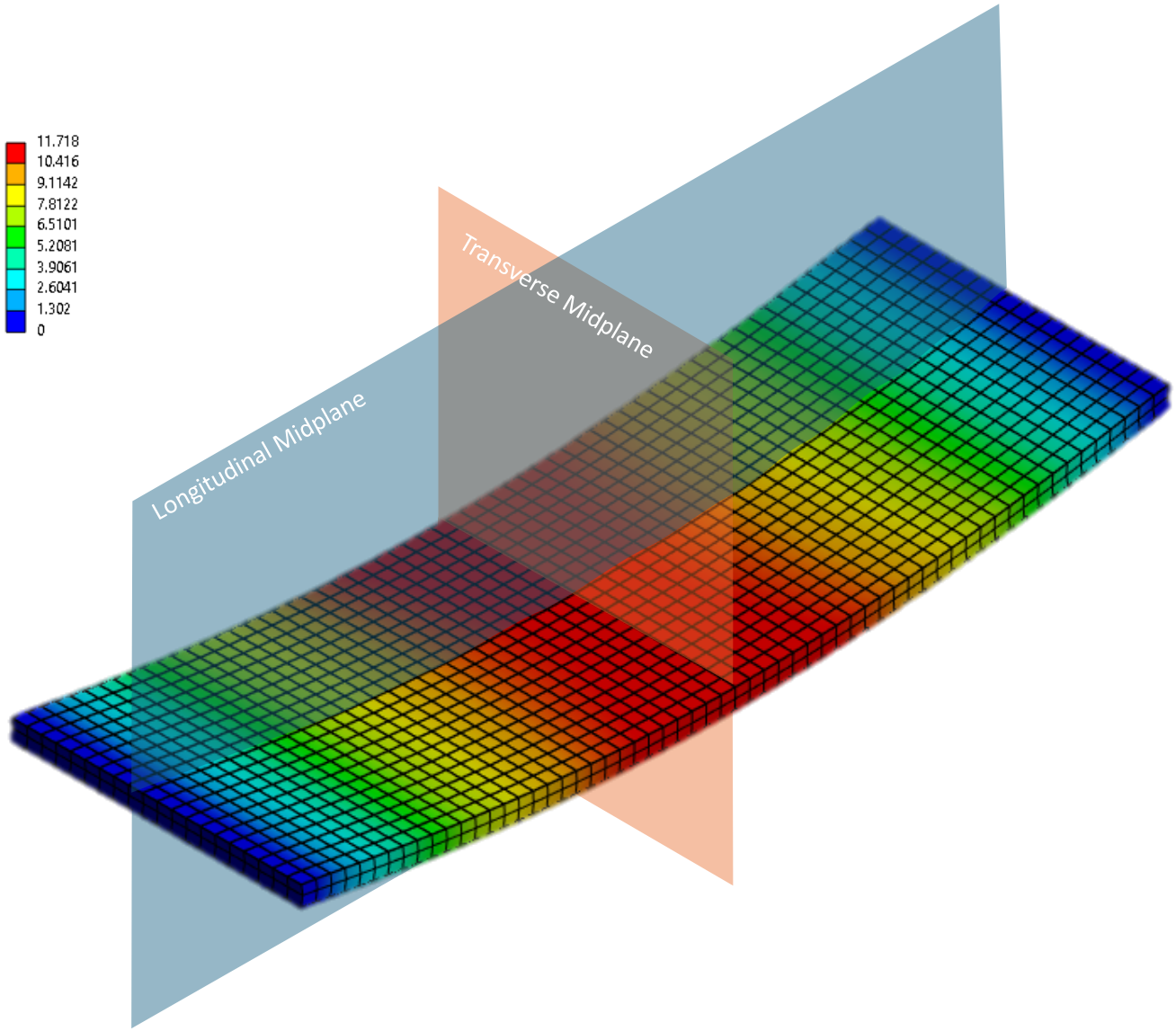

Figure 3-5: Vertical deflection contour depicts bidirectional behaviour along the longitudinal and transverse directions, corresponding to an initial mesh size of 50 mm. Note that units are in mm.

3.2. Main Study

This section served to describe the adaptation of the previously established methodology to the trapezoidally-stiffened GFRP sandwich panel. It also served to describe the steps applied in determining the relationship between the input and output variables, and the tools used in assisting with identifying the optimal panel design.

This section shared most of its methodology described in *Section 3.1*. Therefore, in this section, only modifications, and additions made to the aforementioned methodology were described. The flowchart shown in Figure 3-6 provides a general overview of the methodology followed in this section.

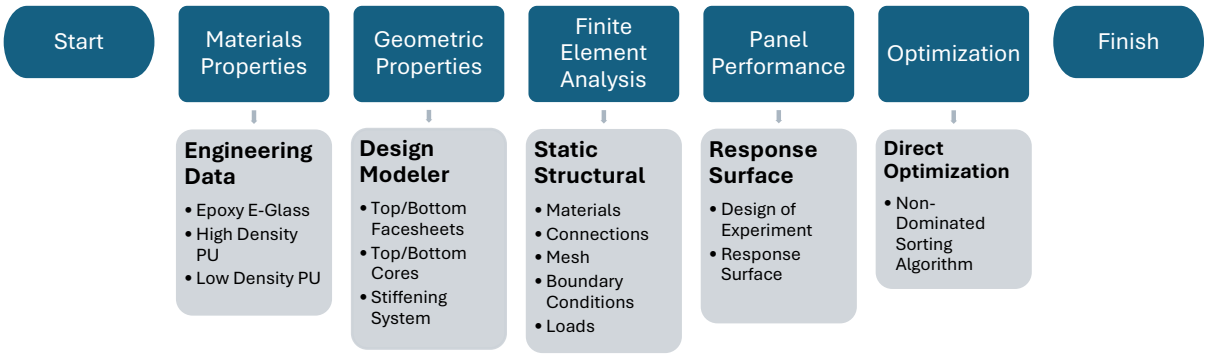

Figure 3-6: Flowchart summarizing the methodology adopted in conducting the main study.

3.2.1. Material Properties

Consider first the *Engineering Data* module. Difficulty was noted in adopting the same core materials specified in the preliminary study. This stemmed from the fact that research pertaining to the cost of the foam cores utilized in Manjusha et al.'s study (2020), proved to be difficult. This would have prohibited cost-optimization procedures from being conducted. Alternatively, the same concept was applied, albeit through the use of alternative PU foam cores, whose material properties were more accessible. In this regard, reference was made to a study conducted by Garrido et al. (2019). From such study, the material properties of the most dense, and the least dense PU foam cores were extracted. These are tabulated in Table 3-4.

Note that similarly as in *Section 3.1.1*, both the low- and high-density PU foam cores were modelled as isotropic elastic materials.

Table 3-4: Mechanical properties of low- and high-density PU foams adopted from (Garrido, Madeira, Proenca, & Correia, 2019).

	Low-Density PU Foam	**High-Density PU Foam**
Density (ρ_{LPU} | ρ_{HPU}) [kg/m^3]	35	120
Young's Modulus (E_{LPU} / E_{HPU}) [MPa]	9.2	63.4
Poisson's Ratio (v_{LPU} / v_{HPU})	0.3	0.3
Shear Modulus (G_{LPU} / G_{HPU}) [MPa]	3.53	24.32
Material Cost (c_{LPU} / c_{HPU}) [€/m^3]	253	426

In defining the unit cost associated with the epoxy e-glass woven fabric (c_{FRP}), the properties of the individual constituents were first identified. The relevant properties of such materials are exhibited in Table 3-5.

Table 3-5: Mechanical properties of epoxy and e-glass woven fabric, adopted from (EasyComposites, 2016) and (Garrido, Madeira, Proenca, & Correia, 2019), respectively.

	Epoxy	**E-Glass Woven Fabric**
Density (ρ_m / ρ_f) (kg/m^3)	1150	2570
Young's Modulus (E_m / E_f) [GPa]	4	70
Shear Modulus (G_m / G_f) [GPa]	1.54	27.00
Poisson's Ratio (v_m / v_f)	0.3	0.3
Unit Cost (c_m / c_f) [€/kg]	15.43	3.40

Next, the proportion of the constituents making up the composite material needed to be defined. This was achieved via the fibre-volume ratio[iv]. All corresponding calculations are included in *Appendix A.3*. In this regard 62.2% of the composite material was composed of fibre (V_f), whilst 37.8% of the composite material was composite of matrix (V_m). The unit cost of the facesheets was calculated as the sum of the product of the volume ratio and the unit cost, for each constituent. This was expressed in Eq. 3.1. Thus, the cost per unit mass of the epoxy e-glass woven fabric was noted to be €7.95.

$$c_{FRP} = V_f c_f + V_m c_m \qquad \text{Eq. 3.1}$$

[iv] For information pertaining to the fibre-volume ratio, refer to *Section 2.1*.

Note that similarly as in *Section 3.1.1*, the epoxy e-glass woven fabric was modelled as an orthotropic elastic material.

3.2.2. Geometric Properties

Next the geometric modelling of the stiffened GFRP sandwich panel was considered. Here, the same approach adopted in *Section 3.1.2* was adopted. The difference was that in addition to the sketches described in *Section 3.1.2*, an additional sketch was generated to cater for the stiffening system. The sketches making up the stiffened GFRP sandwich panel are shown in Figure 3-7.

Note that as seen from Figure 3-7, the trapezoidal stiffeners (shown in RED) were sketched on the faces of cores #2 and #4. This was done to allow the *share topology* function to be adopted, thus providing mesh continuity within the model. Independence was however noted to be present between the trapezoidal stiffeners, and cores *#1* and *#5*. This was mitigated via the implementation of *contact elements*, specifically *targe 170*, which simulated a bonded contact between the concerning components. Such elements were used owing to their property in allowing contact between shell and solid elements. The stiffness associated with such contact elements was calculated based on the *pure penalty function formulation*, more of which may be found in *Appendix A.4* (ANSYS, Inc., 2023).

Verification of the proper functioning of the *contact elements* was conducted through the *status contact tool*. This provided a graphical view (Figure 3-8) of the status of the concerning contact. Proper set up was identified to have been achieved if the indicator on the mating surface was RED in colour. This was denoted to imply fixity (termed *sticking* within *ANSYS Workbench*) between the faces of the selected components.

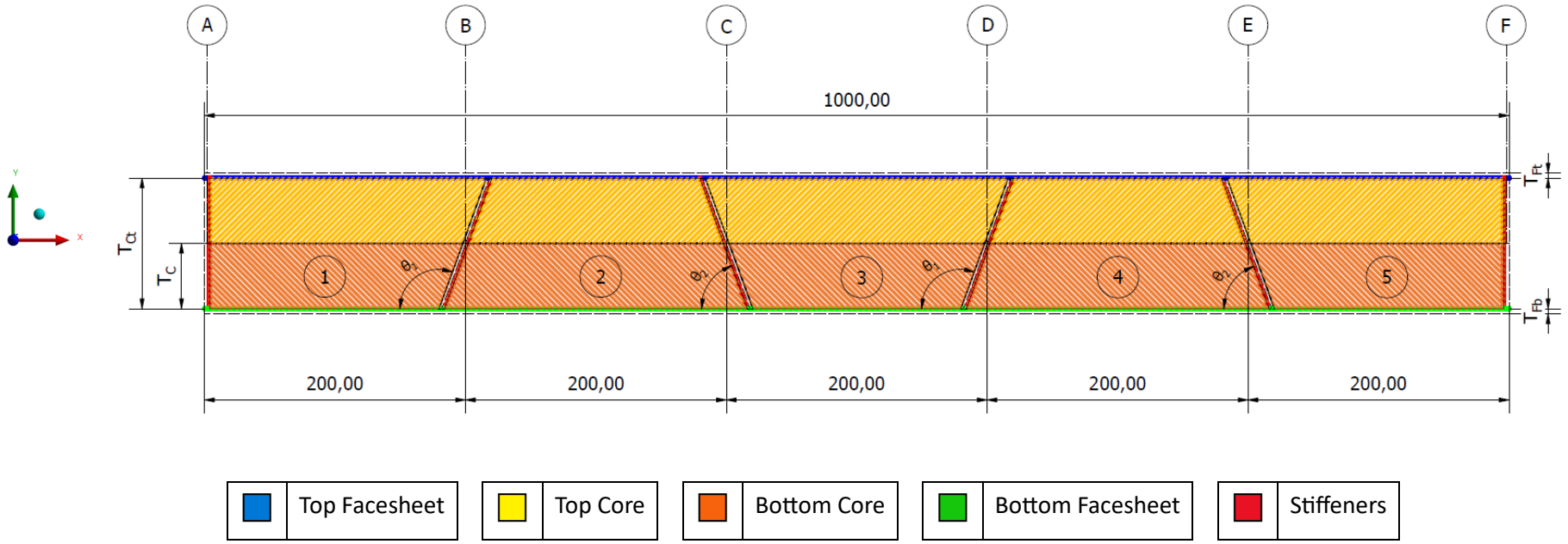

Figure 3-7: Geometry of GFRP sandwich panel was comprised of 5 independent sketches; top facesheet; top core, bottom core; bottom facesheet and, stiffening system. Note that dimensions are in mm

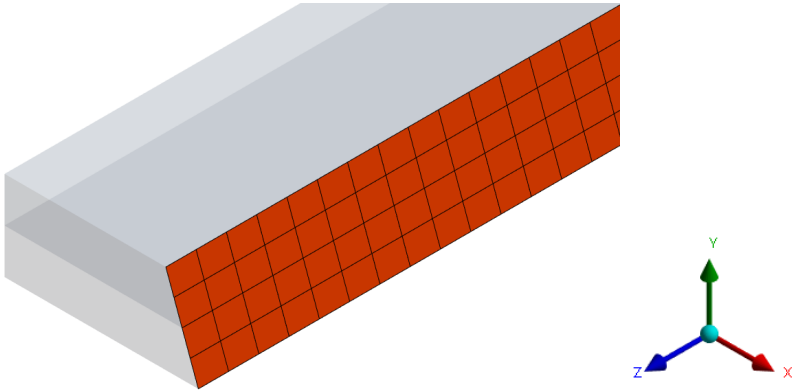

Figure 3-8: Red interface indicated fixity (termed "sticking" within ANSYS Workbench) between core #1 and stiffener B.

In total, the model was constituted of 18 bodies; 2 facesheets; 4 trapezoidal stiffeners; 2 edge stiffeners; 5 low-density PU cores, and; 5 high-density PU cores.

Next, parameterization of the geometric model was conducted. The parameters, and the associated parametric relationships are shown in Table 3-6.

Table 3-6: Summary of the geometric parameters.

Parameter	Symbol	Type	Input Value/Expression	Step Size
Facesheet Thickness (Top)	T_{Ft}	Independent	1.2 – 4.0 mm [3 – 10 plies]	0.4 mm
Facesheet Thickness (Bottom)	T_{Fb}	Dependent	T_{Ft}	NA
Total Core Thickness	T_{Ct}	Independent	50 -100 mm	10 mm
Core Thickness	T_C	Dependent	$\left(\frac{T_{Ct}}{2}\right)$	NA
Half Stiffener Thickness (Left)	T_{Sl}	Dependent	$\frac{\left(\left(ROUNDUP\left(\frac{0.7[T_{Ft}]}{0.4}\right)\right)*0.4\right)}{2}$	NA
Half Stiffener Thickness (Right)	T_{Sr}	Dependent	(T_{Sl})	NA
Stiffener Angle #1	ϑ_1	Independent	50° – 130°	10°
Stiffener Angle #2	ϑ_2	Dependent	$(180° - \theta_1)$	NA

Parameterization brought about a plethora of different panel configurations. For this reason, a designation system was devised in identifying the different configurations. Following is the generic form of the designation system devised: $\boldsymbol{A\vartheta_1 C T_{Ct} F T_{Ft}}$. Here ***A*** denoted the angle of the trapezoidal stiffening system; ***C*** denoted the total thickness of the core, and; ***F*** denoted the thickness of the facesheet.

3.2.3. Finite Element Analysis

Next the *Static Structural* module was set up. The aim of setting this module was to establish a foundation for the *Design of Experiment* (DOE) component within the *Response Surface* module to conduct simulations of specific panel configurations. More details on the *Response Surface* module can be found in *Section 3.2.4*. It was determined that the *Static Structural* module would best be set up on the panel with the largest geometric dimensions and complexity to identify the smallest mesh size applicable to all sandwich panel configurations. Therefore, the setup was based on panel *A50C100F4.0*, featuring the thickest core and facesheet options, along with a 50° stiffening angle. Note that a 130° stiffening angle would also have been suitable.

Within the *Static Structural* module, the same material-geometry linkages adopted in *Section 3.1.3*, were applied. Additionally, the material properties assigned to the facesheets were also applied to the panel's stiffening system.

In determining the panel's total mass (m_T) and materials cost (C_T), the mass (m_x) and volume (V_x) of the different components making up the panel needed to be parameterized. Note that the subscript notation used was as follows; *LPU* denoted low-density PU cores; *HPU* denoted high-density PU cores; *F* denoted facesheets, and; *S* denoted stiffeners. The parametric relationships developed in calculating the total mass and cost of the GFRP sandwich panel are shown in Table 3-7.

Table 3-7: Summary of the mass and cost-related parametric relationships.

Parameter	Symbol	Type	Expression
Mass of Sandwich Panel	m_T	Dependent	$\sum_{i=1}^{5}(m_{LPUi}+m_{HPUi})+\sum_{i=1}^{2}m_{Fi}+\sum_{i=1}^{6}m_{Si}$
Cost of Sandwich Panel	C_T	Dependent	$\sum C_{LPU}+C_{HPU}+C_{FRP}$
Cost of Low-Density PU	C_{LPU}	Dependent	$\sum_{i=1}^{5}(V_i c)_{LPU}$
Cost of High-Density PU	C_{HPU}	Dependent	$\sum_{i=1}^{5}(V_i c)_{HPU}$
Cost of FRP	C_{FRP}	Dependent	$\sum C_m+C_f$
Cost of Matrix	C_m	Dependent	$V_m c_m\left(\sum_{i=1}^{2}m_{Fi}+\sum_{i=1}^{6}m_{Si}\right)$
Cost of Fibre	C_f	Dependent	$V_f c_f\left(\sum_{i=1}^{2}m_{Fi}+\sum_{i=1}^{6}m_{Si}\right)$

While modelling the GFRP sandwich panel, the numerical model was halved along the longitudinal midplane, owing to symmetry in design. In this manner, the component of displacement normal to the plane of symmetry, at the plane of symmetry, was set to zero. This was done to allow increased savings in computational costs, as well as accuracy.

Next the composition of the mesh was considered. The same meshing philosophy adopted in *Section 3.1.3* was adopted. Thus, the facesheets and the stiffening system were both modelled as shell elements. The cores were modelled as solid elements. As opposed to the use of 4-nodal shell element, *shell 181*, 8-nodal shell elements, *shell 281*, were used in meshing the facesheets and the stiffening system. This was done to allow higher degrees of accuracy to be achieved. Note that meshing of the cores was achieved via solid elements, *solid 186*.

As in *Section 3.1.3*, these elements were meshed into the geometric model using the *sweeping method.* This was adopted owing to the extrudable design of the sandwich panel. Further information pertaining to the difference between the different element types, rationale behind the specific elements chosen, and meshing method, may be found in *Appendix A.1.*

The appropriate initial mesh size determined through the application of the same philosophy adopted in *Section 3.1.3* proved to be unsuccessful. This occurred due to the element capacity associated with the student license of *ANSYS Workbench* (ANSYS, Inc., 2023). For this reason, the acceptable average element quality was dropped to 0.85. In this regard, the largest initial mesh size was noted to be 23 mm. The mesh configuration for panel *A50C100F4.*0 is shown in Figure 3-9.

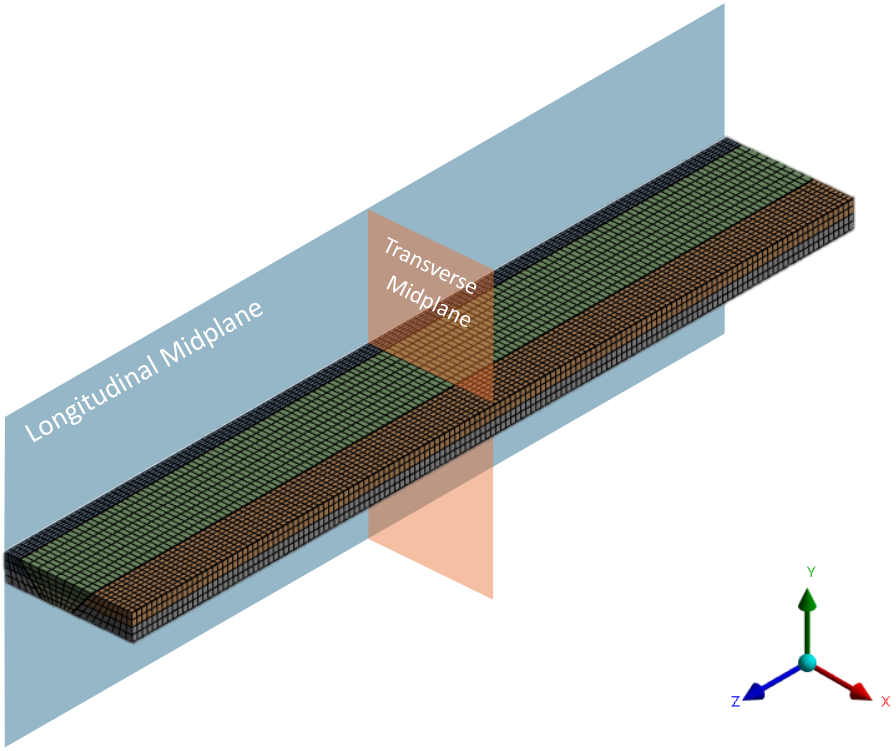

Figure 3-9: Isometric view of the initial mesh for configuration A50C100F4.0.

The same types of boundary conditions and loads as described in *Section 3.1.3* were applied. However, owing to optimizing the panel as a monolithic slab within domestic buildings, as per *EN 1991-1-1, Table 6.2*, an increased area load of 2.0 kN/m^2 was applied to the top facesheet (European Committee for Standardization, 2001).

Note that in case that large strains were noted to take place, the effects of geometric nonlinearity were considered in the analyses. In this regard, default settings were utilized, owing to the computational efficiency achieved in the convergence of results (ANSYS, Inc., 2021). More information on the theory behind the geometric nonlinearity, and the techniques utilised within *ANSYS Workbench* pertaining this topic may be found in *Appendix A.5*.

The output result was then generated. The maximum vertical deflection obtained by the panel was recorded (Δ_T). For the initial mesh size set up, this was noted to be 2.3775 mm. In ensuring validity of the output values, a mesh refinement study was conducted. The same procedure adopted in *Section 3.1.3* was applied, albeit for a convergence rate of ± 3.00%. Note that the convergence rate was increased by ± 1.00% owing to a limited number of elements allowed within the student license of *ANSYS Workbench* (ANSYS, Inc., 2023). The ultimate mesh size adopted was of 21 mm, and the associated converged deflection value was of 2.3924 mm. With respect to the penultimate vertical deflection, this provided a change in deflection of 0.62% $\left(= \left(\frac{(-)2.3775}{(-)2.3924} - 1\right) * 100\right)$.

3.2.4. Panel Performance

With the *Static Structural* module set up, the *Response Surface* module was considered next. The purpose of such module was to predict the performance of all panel configurations in terms of material cost, panel mass, and maximum vertical deflection. Within this module, the input variables (T_{Ft}, T_{Ct}, and ϑ_1), and the output variables (Δ_T, m_T, and C_T) were defined. For each input variable, a corresponding lower- and upper-bound was provided together with an associated step size, as shown in Table 3-6. This resulted in 432 sandwich panel configuration runs.

Next a technique was needed to evaluate the performance of all 432 sandwich panel configurations efficiently. Given the large number of configurations, individually changing each input variable, and recording the outcomes would have been labour-intensive. Therefore, *Response Surface* functions were utilized. These are machine learning algorithms that predict the performance of a system on the basis of an initial data set (ANSYS, Inc., 2023). In generating this data set, *Design of Experiment* (DOE) functions were considered. As shown in *Appendix A.6.* two DOE functions were considered. The selected DOE function was the *Face-Centred Central Composite Design*. This choice was made because it provided a sample set that included the performance of panel configurations at the maximum and minimum input variable levels. This approach mitigated the need for the machine learning algorithm to extrapolate beyond the range of the provided data.

Next the machine learning algorithm itself was selected. As described in *Appendix A.6.*, the *Kriging* model was chosen due to its ability to capture complex relationships with high accuracy. The *Kriging* model operates on the principle that panels with configurations similar to the panel whose performance is being predicted are likely to exhibit similar performance. In contrast, panels with dissimilar configurations are expected to perform differently. More information pertaining to the *Kriging* model, and alternative models considered can be found in *Appendix A.6.*

In ensuring the suitability of the selected *Response Surface* function, a comparative analysis was conducted. In this analysis, the performance of panel configurations that were previously simulated using the DOE function were evaluated using the *Kriging* model. As illustrated in Figure 3-10[v], the *Kriging* model demonstrated a good statistical representation of the evaluated data set. This indicated that the chosen *Response Surface* function was suitable for the study.

Next, data pertaining to configurations of constant facesheet, and core thickness were averaged. For each case, the uncertainty, that is, the spread in vertical deflection values owing to variations within the stiffener angle, were calculated. A three-dimensional plot of the predicted data set was then generated in terms of the output variables. Refer to Figure 3-11. Here, trendlines, denoted by $\boldsymbol{CT}_{Ct}$, and $\boldsymbol{FT}_{Ft}$ were set up to indicate configurations of constant core, and facesheet thickness, respectively.

In allowing for the effects of the input variables to be studied, explicit configurations pertaining to specific trends identified on such plot were further evaluated through the *Static Structural* module. For the concerning configurations, vertical displacement contours were generated, from which the maximum vertical deflection along the longitudinal plane (Δ) was extracted and compared to analytical solutions. Note that analytical solutions were conducted on the basis of the *Classical Sandwich Panel Theory*. For more information on this refer to *Section 2.3*.

Von Mises stress contours were also generated. These were generated as opposed to alternative stress contours in case that out-of-plane stresses derived from bidirectional behaviour occurred. As such, the Von Mises stress criterion was selected owing to providing a scalar value, representative of the combined effect of the multi-axial stress state.

[v] Plots pertaining to the accuracy of the predictive model with respect to panel mass, and material cost are shown in *Appendix A.7*. Note that for all output variables, a good degree of predictability was achieved via the *Kriging* model.

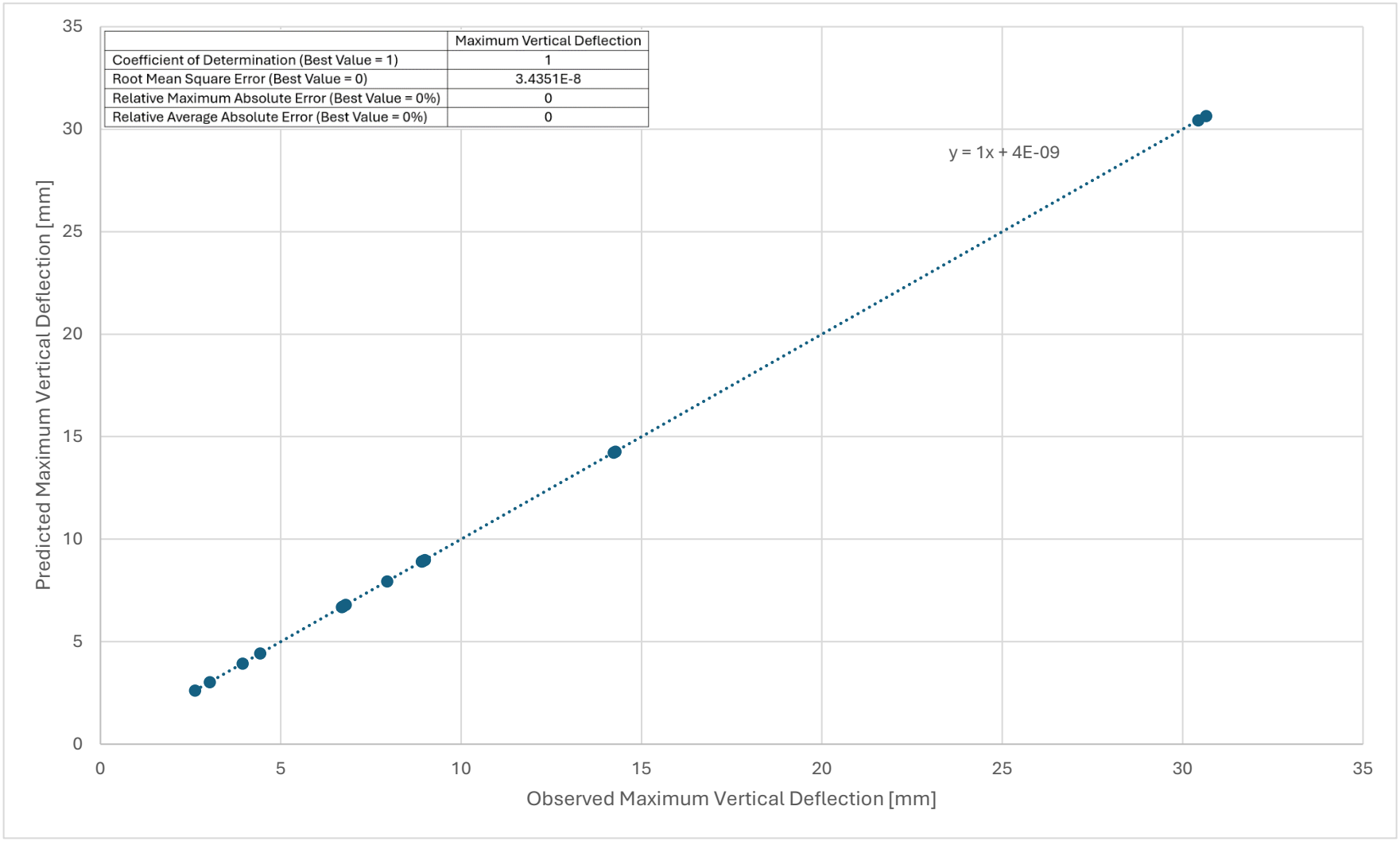

Figure 3-10: Graph of predicted vs observed maximum vertical deflection [mm].

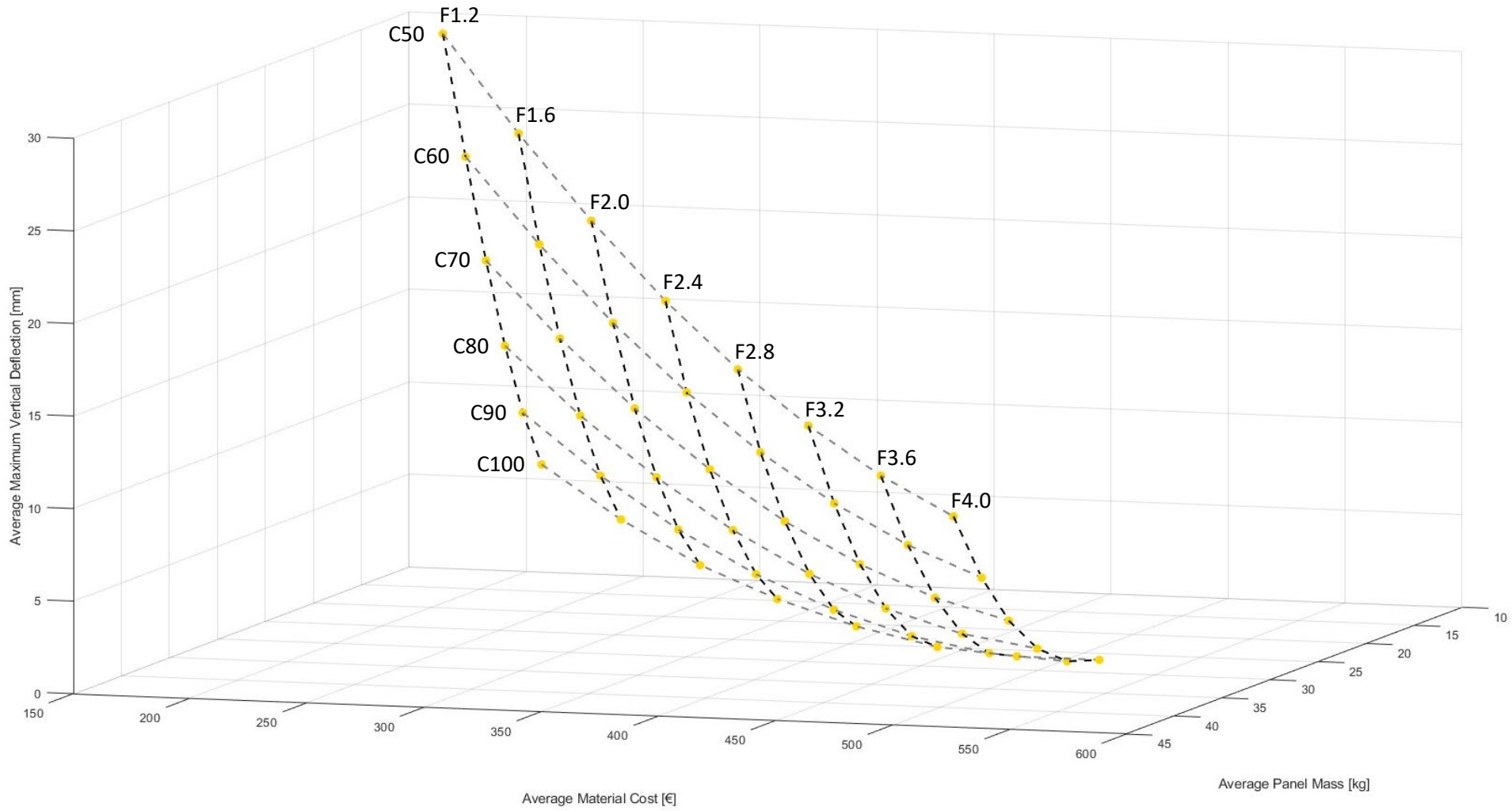

Figure 3-11: Graph of predicted maximum vertical deflection [mm] (z-axis) vs average material cost [€] (y-axis) vs average panel mass [kg] (x-axis) for configurations of constant core and facesheet thickness.

3.2.5. Optimization

In allowing for the identification of the optimal sandwich panel configuration to be facilitated, the *Direct Optimization* module was set up. The purpose of such module was to apply a filter, followed by a sorting algorithm to the data set predicted via the *Kriging* model thus identifying the panels of optimal configuration.

In filtering the data, a set of objectives and constraints pertaining to the output variables were set up. These are summarized Table 3-8. Configurations failing to satisfy the desired objectives and constraints were termed *infeasible;* those that met the requirements were termed *feasible*. Refer to Figure 3-12.

Next, the remainder of the data was sorted. Sorting was achieved via the application of a *non-dominated sorting algorithm;* a sorting algorithm whereby data points were sorted on their susceptibility of being dominated. A data point $\left(A\left(m_{T_1}, c_{T_1}, \Delta_{T_1}\right)\right)$ was set to dominate another data point $\left(B\left(m_{T_2}, c_{T_2}, \Delta_{T_2}\right)\right)$ if $\left(m_{T_1} \leq m_{T_2}\ and\ c_{T_1} \leq c_{T_2}\ and\ \Delta_{T_1} \leq \Delta_{T_2}\right)$ and $\left(m_{T_1} < m_{T_2}\ or\ c_{T_1} < c_{T_2}\ or\ \Delta_{T_1} < \Delta_{T_2}\right)$ were noted to be true. This process resulted in the division of the *feasible* data set into two subsets: *dominated* and *non-dominated*. Refer to Figure 3-13.

From the two sets, the *non-dominated* subset was identified as providing optimal configurations for vertical deflection. These optimal configurations were then evaluated in the *Static Structural* module, where the credibility of the results was ensured.

Table 3-8: Objective and constraints functions devised in filtering the predicted data set.

Parameter	**Objective**		**Constraint**		
	Type	**Target**	**Type**	**Lower Bound**	**Upper Bound**
Maximum Vertical Deflection (Δ_T)	Minimize	0	Lower Bound ≤ Values ≤ Upper Bound	0 mm	8.33 mm[vi]
Total Sandwich Panel Material Cost (C_T)	Minimize	0	Values ≥ Lower Bound	€ 0.00	NA
Total Sandwich Panel Mass (m_T)	Minimize	0	Values ≥ Lower Bound	0 kg	NA

[vi] The upper bound was determined by the deflection control limit $\frac{span}{360}$. This was adopted on the basis of similarly focused studies (Fam & Sharaf, 2010; Manjusha & Althaf, 2020), further discussed in *Chapter 2*.

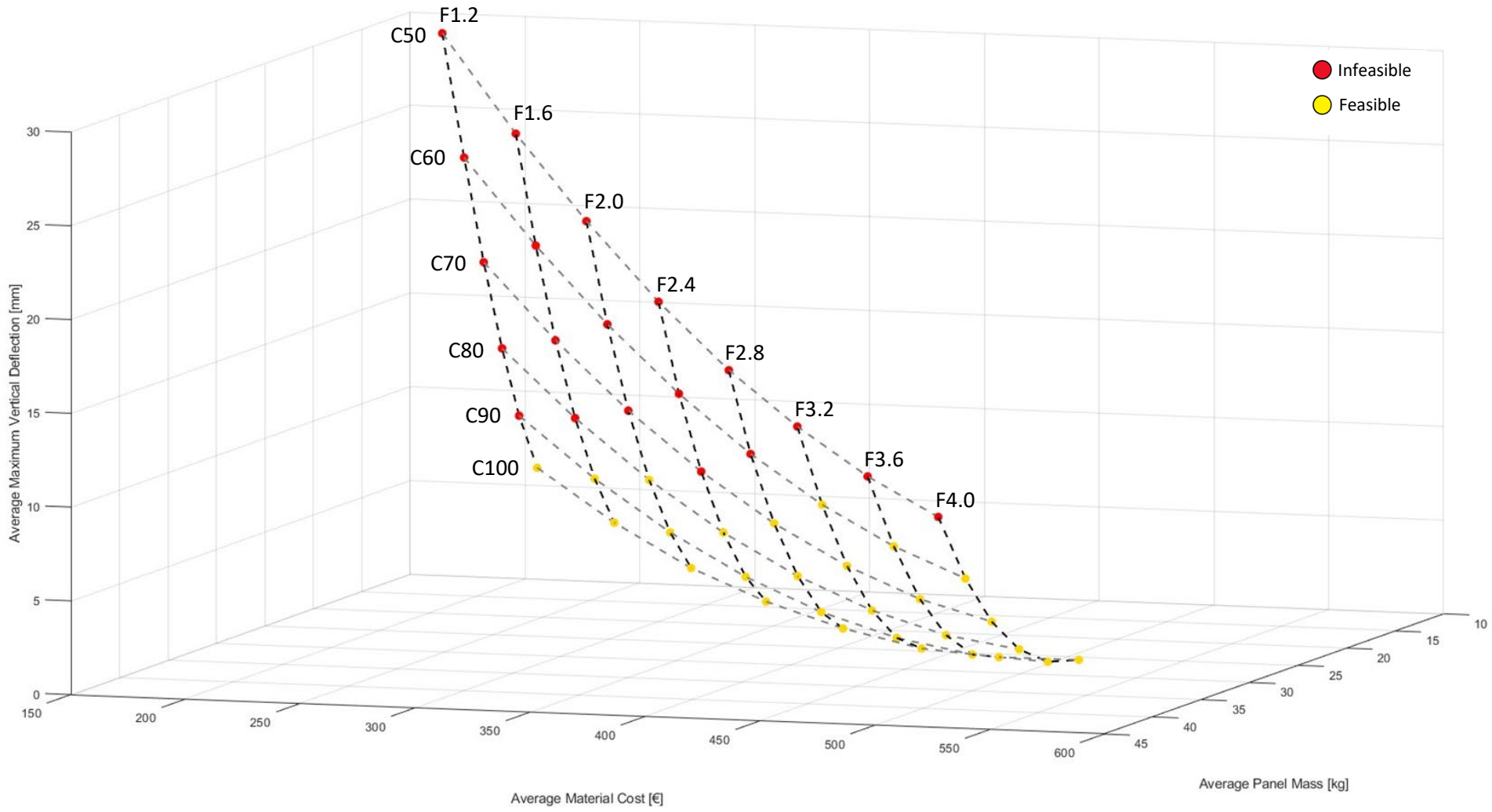

Figure 3-12: Graph of predicted average maximum vertical deflection [mm] (z-axis) vs average material cost [€] (y-axis) vs average panel mass [kg] (x-axis) for configurations of constant core and facesheet thickness. Configurations that failed to meet the set constraints were labelled 'infeasible' (RED), while those that met the constraints were labelled 'feasible' (YELLOW).

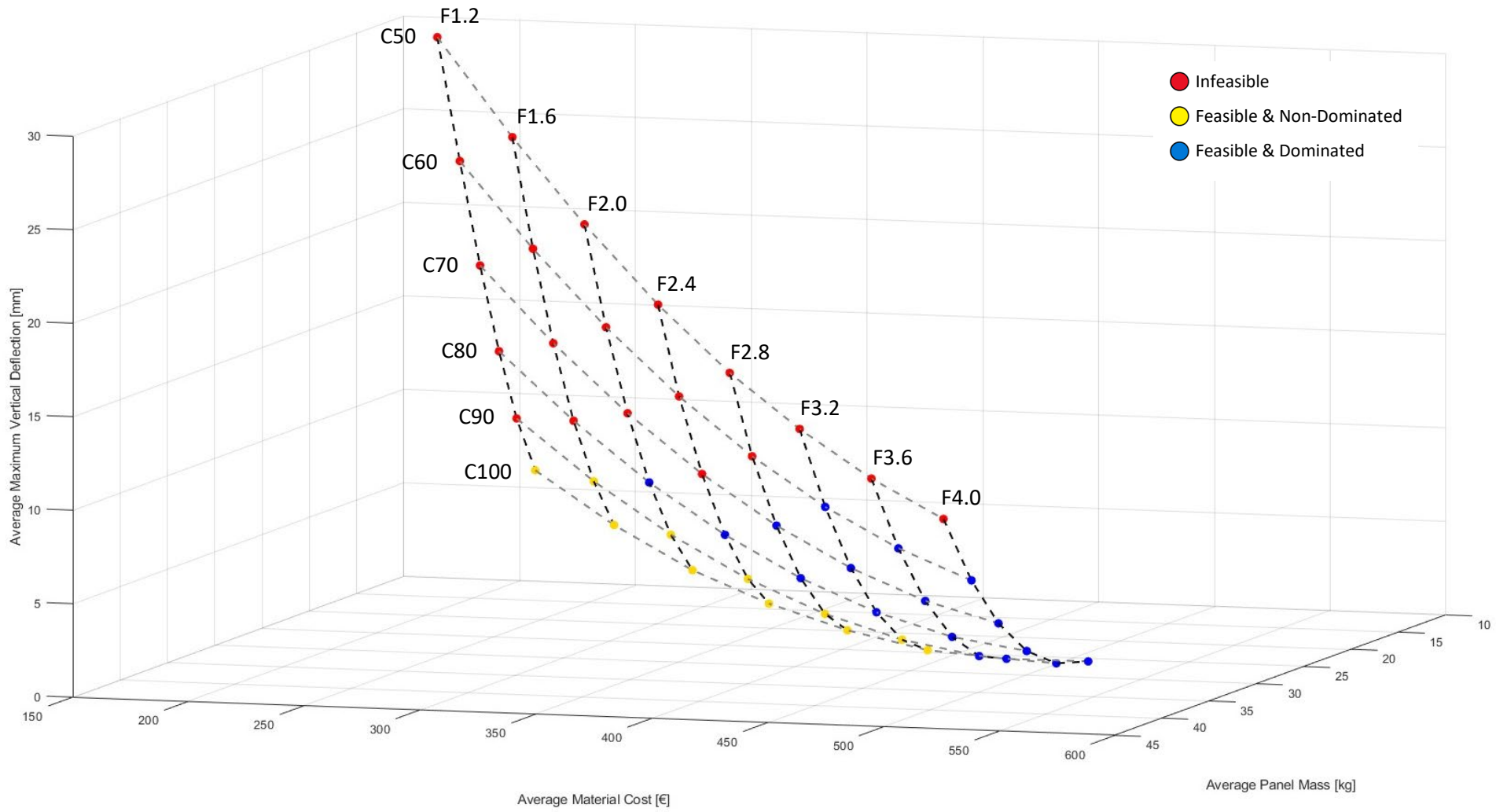

Figure 3-13: Graph of predicted average maximum vertical deflection [mm] (z-axis) vs average material cost [€] (y-axis) vs average panel mass [kg] (x-axis) for configurations of constant core and facesheet thickness. Configurations previously labelled as 'feasible' were further subdivided into 'non-dominated' (YELLOW) and 'dominated' (BLUE) data sets, on the basis of being dominated or not.

In this regard, owing to the applied filt*er, non-dominated sorting algorithm*, and the observed effects imparted by the input variables on the output variables, the optimal panel configuration was to be identified.

3.3. Concluding Remarks

The results from this chapter included a three-dimensional plot of the output variables, divided into three subsets: (i) *infeasible*, (ii) *feasible & dominated, (iii) feasible & non-dominated*. Additionally, as highlighted from this chapter, vertical deflection and Von Mises stress contours of specific panel configurations were also generated.

Based on Figure 3-13, the next chapter described the relationship between the output variables. It also analysed the impact of the input variables on the panel's performance using vertical deflection and Von Mises stress contours. Finally, the chapter revisited the three-dimensional plot from Figure 3-13 and observed trends, to identify the optimal sandwich panel configuration.

4. Results

This chapter is composed of two main sections. The first section focused on understanding the relationships among the output variables themselves. This was followed by an analysis where each output variable was individually evaluated with respect to the input variables. To aid this analysis, vertical deflection and Von Mises stress contours derived from the described numerical simulations were extensively used in conjunction with analytical calculations.

The second section utilized information from the *non-dominated sorting algorithm*, along with insights gained from the first section, to identify the optimal sandwich panel configuration.

Note that throughout this chapter, the designation system described in *Section 3.2.2* was used extensively. Variants of such system were also used. These included $\boldsymbol{C}T_{Ct}\boldsymbol{F}T_{Ft}$, $\boldsymbol{A}\vartheta_1\boldsymbol{F}T_{Ft}$, *and* $\boldsymbol{A}\vartheta_1\boldsymbol{C}T_{Ct}$, to refer to panel systems of constant; core and facesheet thickness; stiffener angle and facesheet thickness, and; stiffener angle and core thickness, respectively. In referring to panel configurations of constant; stiffener angle; core thickness, and; facesheet thickness, the notations $\boldsymbol{A}\vartheta_1$, $\boldsymbol{C}T_{Ct}$, and $\boldsymbol{F}T_{Ft}$, were used respectively.

Additionally, the same naming scheme established in *Section 3.2.2* was used in referring to the specific components within the GFRP sandwich panel.

4.1. Effect on Output Variables & Von Mises Stresses

4.1.1. Vertical Deflection

From the three-dimensional plot in Figure 3-13, two-dimensional plots of maximum vertical deflection vs panel mass (Figure 4-1), and material cost (Figure 4-2), respectively, were extracted. As in the case of Figure 3-13, trendlines denoted by $\boldsymbol{C}T_{Ct}$, and $\boldsymbol{F}T_{Ft}$ were set up to indicate configurations of constant core, and facesheet thickness, respectively. Note that for the purposes of this section, the associated legend in such figures is to be ignored. Such terms were related to the *non-dominated sorting algorithm* and were further defined in the discussion on the optimal panel configuration in *Section 4.2.*

As shown in Figures 4-1, and 4-2, minimizing the panel's maximum vertical deflection resulted in a consequential increase in material cost and panel mass. This trend was consistent across all cases except for panel configurations *C100F3.6*, and *C100F4.0*. For these configurations, the vertical deflection was predicted to be surpassed by panels with the same facesheet thickness but a 90 mm core. This was noted to be erroneous because as described in *Section 2.3*, increasing core thickness, led to an increase in the panel's second moment of area, and thus its flexural rigidity. Given the *Kriging* model's good statistical representation of the sample set from the *Face-Centred Central Composite Design* (refer to Section 3.2.4 – Figure 3-10), the error was suggested to be a function of

the DOE function selected. It is suggested that more elaborate DOE functions with larger sample sizes should have been considered as these would have provided the *Kriging* model with a more extensive data set, leading to more accurate predictions.

Nonetheless, as shown in Figures 4-1, and 4-2, the relationship between the output variables was curvilinear, suggesting that the enhanced performance in vertical deflection was less sensitive to increasing panel mass and material cost.

From these figures, it was also noted that the input parameters did not yield the same degree of influence on the panel's stiffness. A stepwise increase from a 50 mm core thickness was found to be 5.41% more effective than a stepwise increase from a 1.2 mm facesheet thickness. This was suggested to have occurred due to the greater degree of change in the panel's second moment of area when changing the core thickness, as opposed to the facesheet thickness.

The analytical expression Eq. 2.1 for a panel's flexural rigidity, *D*, discussed in S*ection 2.3*, was considered, with considerations also given to the flexural stiffness provided by the stiffening system ($E_F I_S$). Analysis conducted on all panel configurations showed that the governing term was $E_F I_F$. Its contribution was noted to vary from 88.6% to 96.7%, with the lower range associated with thicker core sections and the higher range associated with thicker facesheet sections. Eq. 4.1 was then considered, further defining I_F in terms of its basic constituents based on Figure 4-3.

$$I_F = \frac{2bT_{Ft}^3}{3} + 2bT_{Ft}T_C^2 + 2bT_{Ft}^2T_C \qquad \text{Eq. 4.1}$$

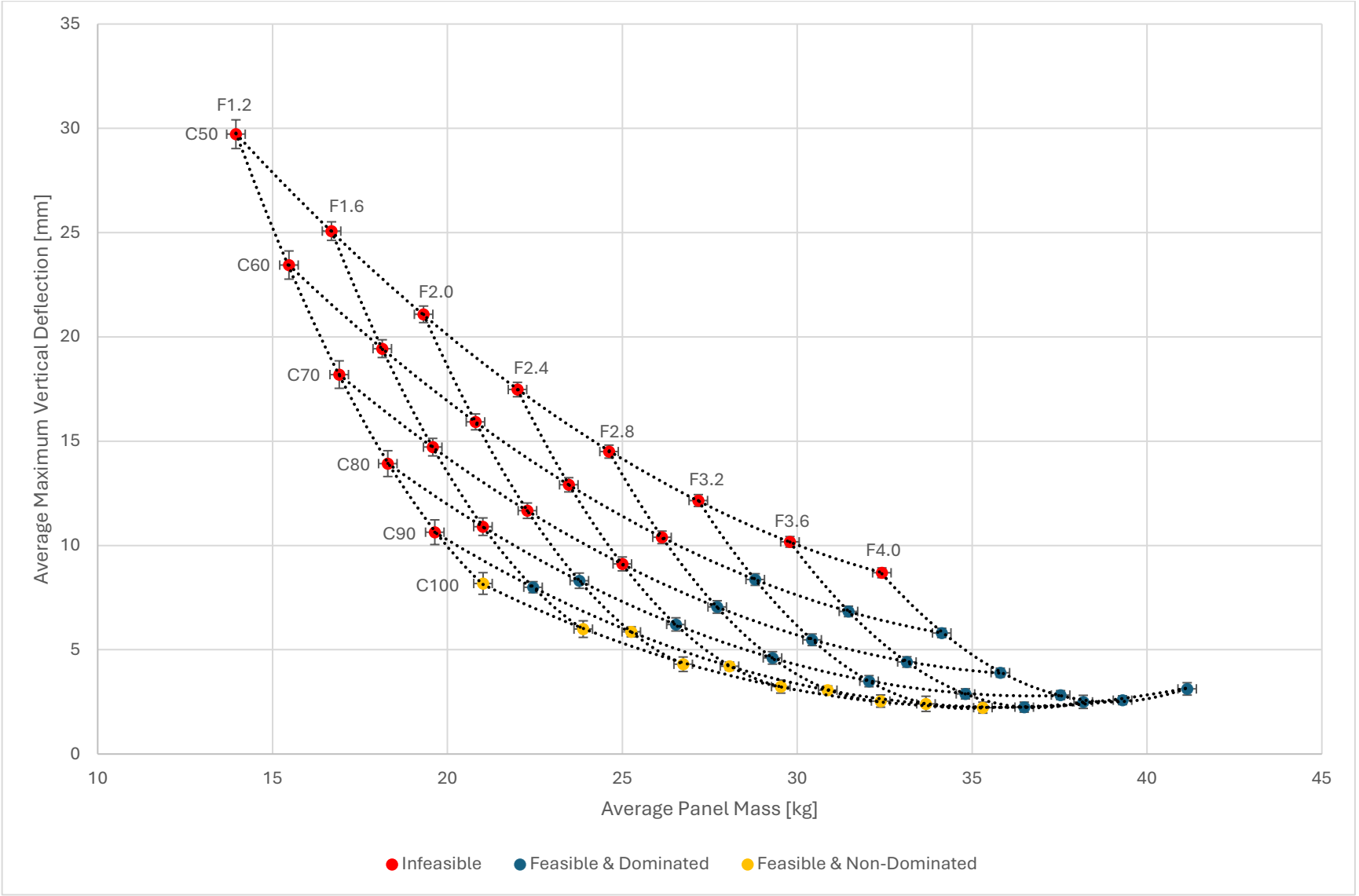

Figure 4-1: Graph of average maximum vertical deflection [mm] vs panel mass [kg] for configurations of constant core and facesheet thickness

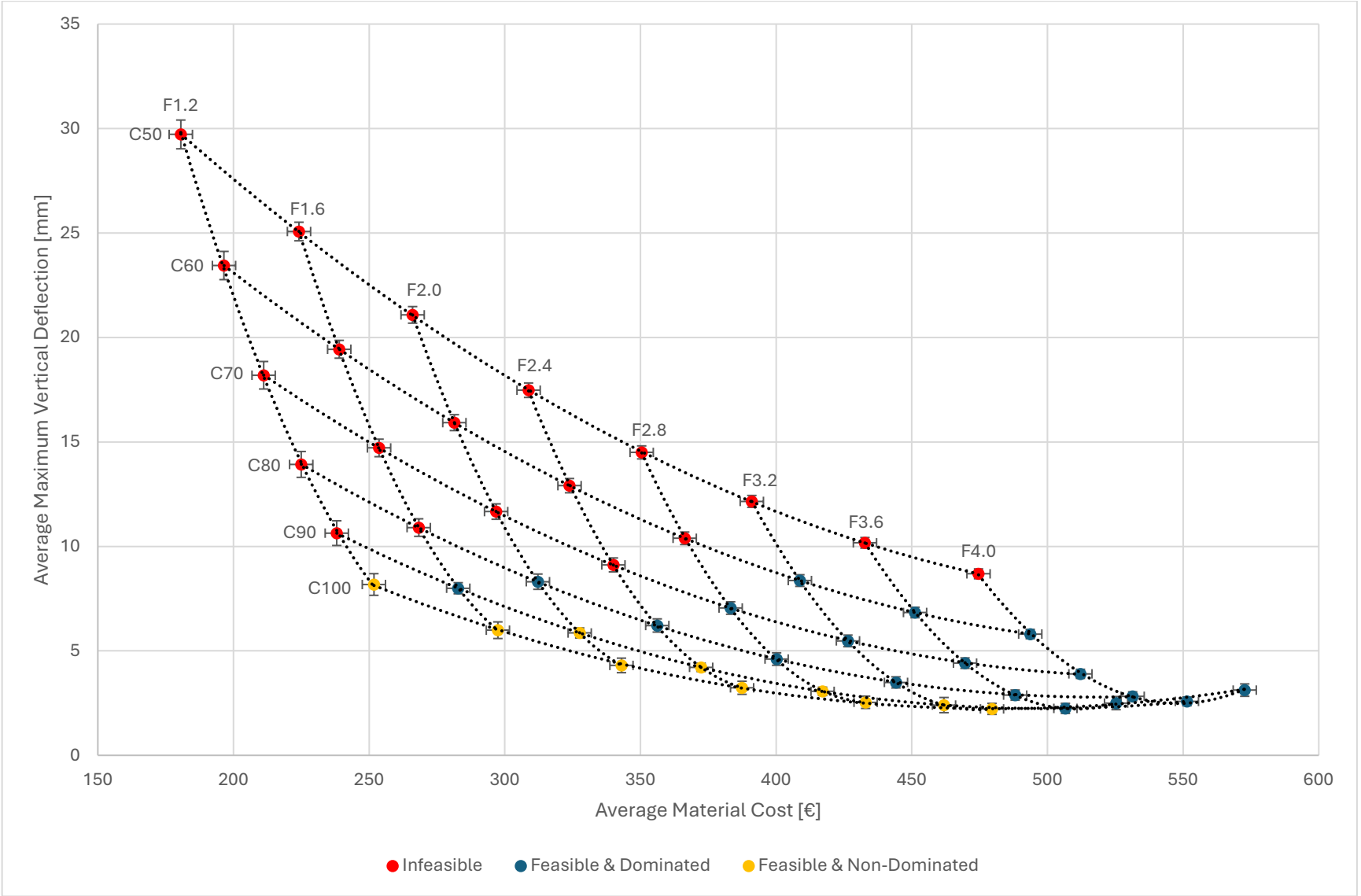

Figure 4-2: Graph of average maximum vertical deflection [mm] vs material cost [€] for configurations of constant core and facesheet thickness.

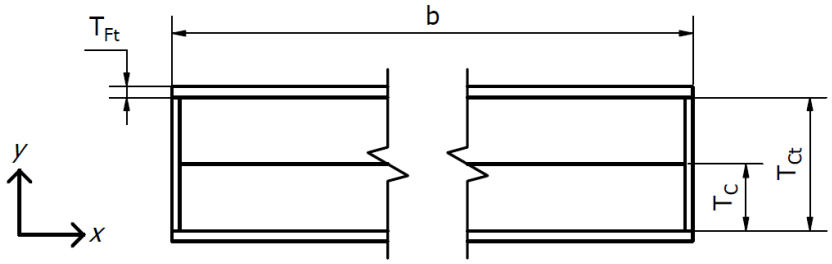

Figure 4-3: Broken schematic of the designed GFRP sandwich panel.

Evaluating Eq. 4.1 showed that $2bT_{Ft}T_C^2$ was the predominant term. Depending on the panel's configuration, its contribution varied from 85.6% to 97.6%. Due to the square associated with the core thickness and its high-value domain, it was deduced that the core thickness was the predominant variable in determining I_F, and consequently *D.* Hence, the increased effectiveness observed in changing the core thickness rather than the facesheet thickness.

Note that although a bilayer core has been considered in this dissertation, the neutral axis was still considered to act at the geometric centre of the sandwich panel. This decision was conducted on the basis that the actual shift associated with the neutral axis was found to be negligible.

Additionally, from Eq. 2.1, the contribution of the core varied from 0.4% to 2.7%. This implied that the core provided little-to-no effect in strengthening the sandwich panel.

The influence of the angle of the stiffening system on the panel's maximum vertical deflection was denoted in Figure 4-1, and 4-2 via the error bars. From such figures, the error bars were noted to vary in magnitude. The largest absolute change in vertical deflection was observed for panel *C50F1.2*, with a vertical deflection change of ± 0.65 mm when altering the angle of the stiffening system. However, relative to the panel's average maximum vertical deflection, this change represented the smallest contribution at ± 2.19%. In contrast, the smallest absolute change in deflection was noted for panel *C100F4.0*, with a vertical deflection change of ± 0.20 mm. Despite this, it represented the largest percentage contribution relative to the panel's average maximum vertical deflection, at 6.41%.

In verifying the observations highlighted by the *Kriging* model, further analysis was conducted through discrete FEA models on trendlines *F1.2*, and *C50*, respectively.

Figure 4-4 illustrated a representative vertical deflection contour derived from this analysis. The deflection contour shown applied to configuration *A90C50F1.2*. Due to minimal variation in vertical deflection contour trends across different panel configurations, the contour plot shown in Figure 4-4 sufficed for the purposes of this discussion. Deflection contours for the entire set of analysed configurations can be found in *Appendix B.2*.

Upon analysing the contour plot in Figure 4-4, it was noted that there were two main sets of deflection curves: one oriented longitudinally, and the other transversely. Both types of deflection displayed a curvilinear relationship, with the maximum vertical deflection along the longitudinal plane occurring at midspan, and the maximum vertical deflection along the transverse plane occurring at the free end of the panel. The latter coincided with the system's maximum vertical deflection, as indicated in Figure 4-4. It was identified that all configurations exhibited bidirectional behaviour, but vertical deflection predominantly occurred along the longitudinal plane.

As described in *Section 3.1.3*, this occurrence was attributed to the orthotropic nature of the GFRP sandwich panel, which manifests in two ways. First, the GFRP facesheets had fibres unidirectionally aligned along the longitudinal direction. This caused the panel's stiffness along the longitudinal direction to differ to that in the transverse direction. This concept was introduced in *Section 2.1*, where it was noted that the longitudinal stiffness provided by a GFRP laminate is similar in magnitude to that of the fibres themselves (i.e. $E_{11} = E_f = 70$ GPa), while the transverse stiffness is comparable to that of the matrix (i.e. $E_{22} = E_m = 4$ GPa).

This effect was further compounded by the implementation of the stiffening system. Since the stiffeners were introduced solely along the longitudinal direction, they increased the second moment of area in that direction, thereby further stiffening the panel along the longitudinal direction.

This meant that the bidirectional behaviour of the panel was therefore attributed to the difference in stiffness properties in the longitudinal and transverse directions, derived from both the material and geometric properties used.

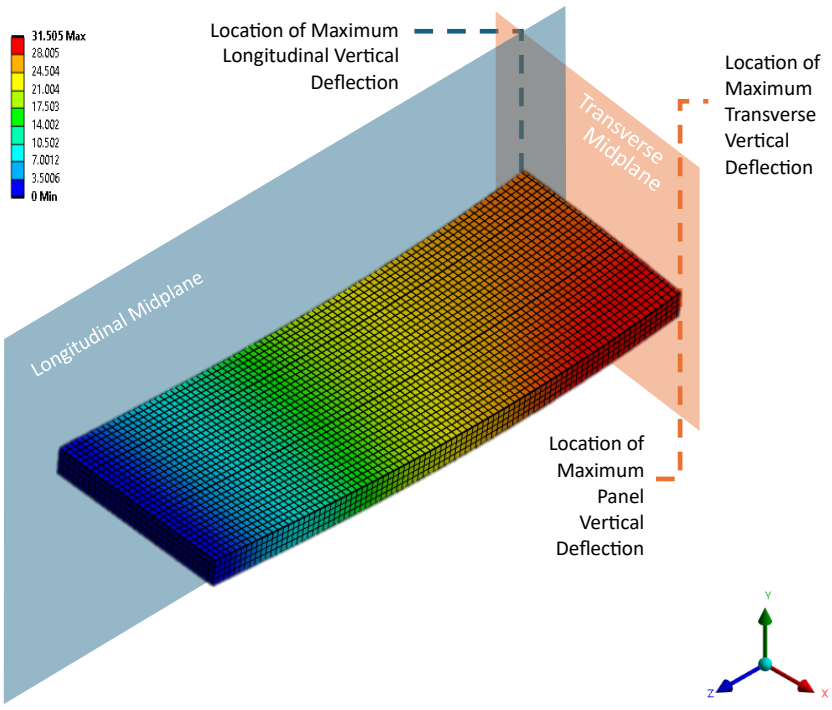

Figure 4-4: Typical total deflection contour. Shown specifically is of configuration A90C50F1.2. Note that units are in mm.

4.1.1.1. Core & Facesheet Thickness

Plots of the simulated maximum vertical deflections at the longitudinal midplane, along with their equivalent analytical solutions, were shown with respect to core thickness and facesheet thickness in Figures 4-5A and B, respectively. Note that a tabulated version of same results, including additional data pertaining to mesh quality, is shown in *Appendix B.1.* A reasonable agreement was observed between the simulated and analytical solutions, suggesting that the effects of geometric nonlinearity contributed negligibly to the panel's total vertical deflection. This conclusion was drawn because the *Classical Sandwich Panel Theory*, which disregards such effects, matched the simulation results well.

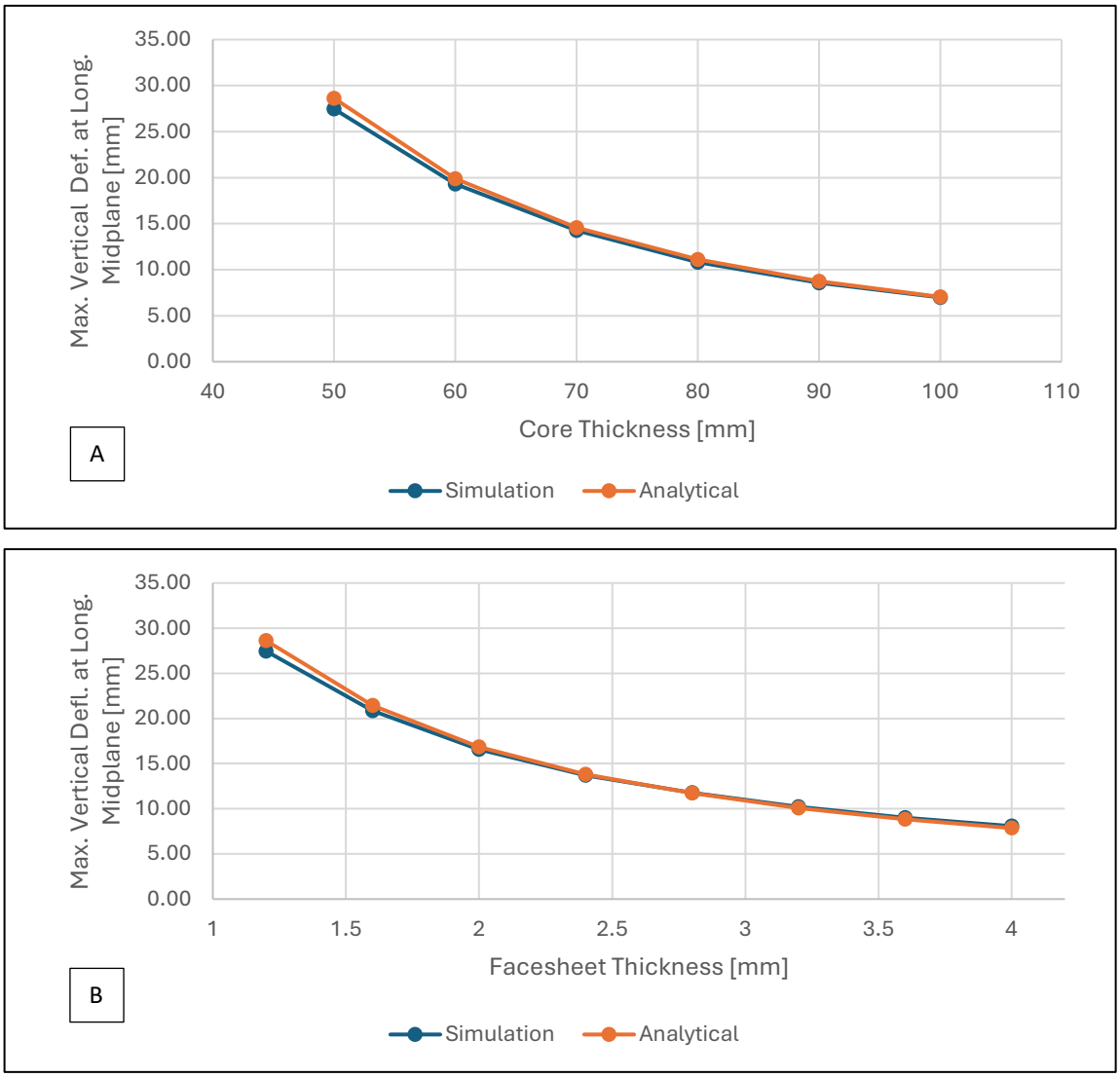

Figure 4-5: Graph of maximum vertical deflection at longitudinal midplane [mm] vs (A) core thickness [mm] for configuration A90F1.2 and; (B) facesheet thickness [mm] for configuration A90C50.

In both cases, the relationship between the maximum vertical deflection at the longitudinal midplane with respect to core thickness and facesheet thickness was observed to be curvilinear. These observations suggested that the effectiveness of the core and facesheet thickness on the panel's vertical deflection decreased with increased thickness values. This was consistent with the observations made by Manjusha et al. (2020).

In *Section 4.1.1*, it was determined that the flexural stiffness, D, of the panel was predominantly a function of $E_F I_F$. Furthermore, it was noted that I_F was primarily a function of $2bT_{Ft}T_C^2$. Analysis of this term showed that for a constant facesheet thickness, T_{Ft}, the second moment of area of the facesheet varied as a function of the square of the core thickness T_C. In this manner, it was this quadratic relationship that gave rise to the curvilinear relationship observed between the maximum vertical deflection along the longitudinal midplane and the core thickness shown in Figure 4-5A.

In the case of Figure 4-5B, for a constant core thickness, the term $2bT_{Ft}T_C^2$ became a linear function. For this reason, focus shifted on the second-most dominant term in Eq. 4.1, This was noted to be $2bT_{Ft}^2T_C$, whose contribution across all panel configurations varied from 2.34% to 13.69%. Examination of such term showed that for a constant core thickness, T_C, the panel's flexural rigidity varied linearly as a function of $2bT_{Ft}T_C^2$, and quadratically, as a function of $2bT_{Ft}^2T_C$. As a result of the latter function, a parabolic relationship was observed between the maximum vertical deflection along the longitudinal midplane and the facesheet thickness.

4.1.1.2. Stiffener Angle

In better understanding the influence of the angle of the stiffening system on the panel's performance, discrete analytical and finite element studies were conducted on configurations *C50F1.2*, *C50F4.0*, *C100F1.2*, *C100F4.0*. Refer to Figure 4-6, and Figures 4-7A, B, and C, respectively.

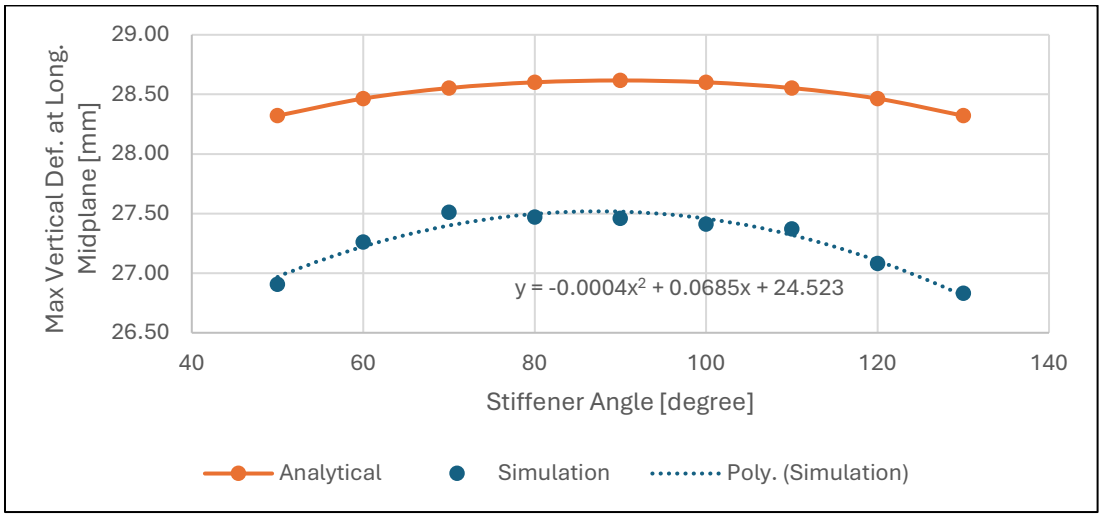

Figure 4-6: Graph of maximum vertical deflection at longitudinal midplane [mm] vs stiffener angle [degree] for configuration C50F1.2.

Note that a tabulated version of same results, including additional data pertaining to mesh quality, is shown in *Appendix B.1*

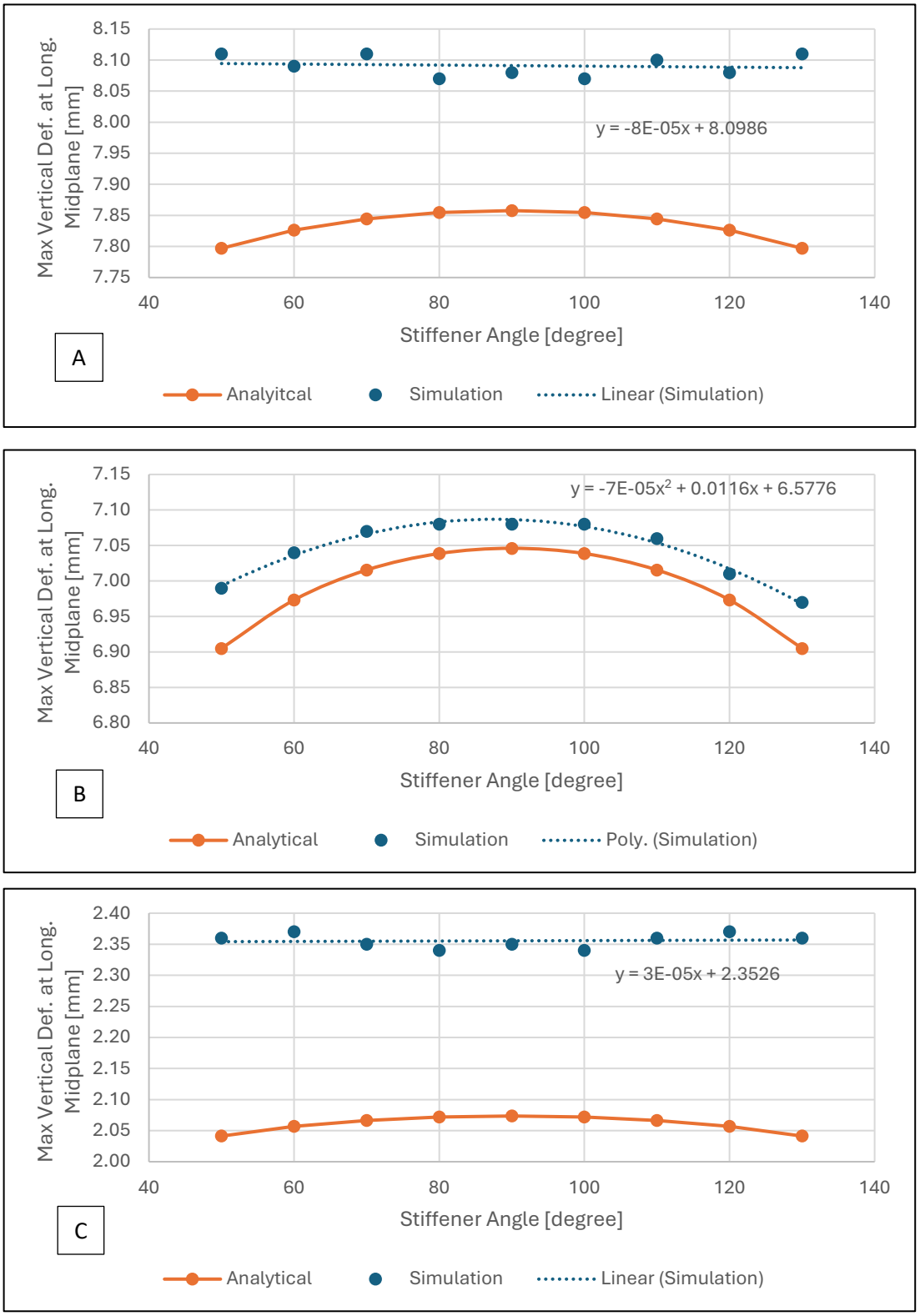

Figure 4-7: Graph of maximum vertical deflection at longitudinal midplane [mm] vs stiffener angle [degree] for configuration (A) C50F4.0, (B) C100F1. 2, and (C) C100F4.0.

Variation was noted between the analytical and simulated data sets in terms of the followed trend and range. Regarding the latter, reasonable agreement was found for data sets pertaining to configurations *C50F1.2 (*Figure 4-6*)*, *C50F4.0* (Figure 4-7A), and *C100F1.2* (Figure 4-7B), with differences ranging from 3.65% to 5.26%, 2.74% to 4.01%, and 0.59% to 1.23%, respectively. The only significant mismatch in magnitude was observed for configuration *C100F4.0* (Figure 4-7C), where the difference ranged from 12.94% to 15.61%. However, this magnitude of discrepancy was considered *relatively low* in some studies, such as that conducted by Correia et al.'s (2012), which compared results with experimental flexural data rather than vertical deflection finite element results.

With respect to the trend observed, solution sets for configurations *C50F1.2* (Figure 4-6), and *C100F1.2* (Figure 4-7B) were found to align. This alignment was noted due to the observed parabolic relationship in both solution sets. It indicated that the effectiveness of the stiffener angle increased as the corresponding angle approached extreme values within its domain. Symmetry was also observed about the 90^{o} angle, with a maximum occurring at 90^{o} and a minimum at 50^{o} and 130^{o}. This suggested that the following pairs of angles performed similarly; 50^{o} and 130^{o}, 60^{o} and 120^{o}, 70^{o} and 110^{o}, 80^{o} and 100^{o}.

Although not to the same extent, the analytical solutions for panel configurations *C50F4.0* (Figure 4-7A), and *C100F4.0* (Figure 4-7C) also showed a symmetric parabolic trend. In this case, changing the angle was found to have a minimal effect on the panel's stiffness. The analytical solutions estimated a maximum change in vertical deflection of 0.06 mm for panels *C50F4.0* and 0.03 mm for panels *C100F4.0*. This change was not observed in the simulated solutions, likely due to the relatively large convergence rate used (± 3.00%) in the mesh study. This limited the resolution needed to clearly define the effects of changing the angle of the stiffening system.

Comparing configurations *C50F4.0*, and *C100F4.0* to panel configurations of the same core thickness, but 1.2 mm facesheet thickness, i.e., configurations *C50F1.2*, and *C50F4.0*, respectively, showed that the range in magnitude for the change in vertical deflection due to changes in the angle of the stiffening system decreased by 80%, and 79%, respectively. This finding was consistent with that shown in Figure 4-1 and 4-2, where the error bars associated with configurations of lower facesheet thickness exhibited greater degrees of uncertainty.

This was suggested to have occurred due to the increased contribution of $E_F I_F$, and consequential reduction of $E_F I_S$, in Eq. 2.1 for panels with increasing facesheet thickness. In fact, comparing the contributions of $E_F I_S$ in Eq. 2.1, for configurations *A90C50F1.2*, and *A90C50F4.0*, showed a reduction of 1.59%, from 4.49% to 2.90%. The same applied to configurations *A90C100F1.2* and *A90C100F4.0*, where a reduction of 2.62% was noted, from 8.65% to 6.03%.

Regarding the symmetric parabolic relationship observed, this was noted to be a consequence of the length of the trapezoidal stiffener, L_S, being a function of trigonometric ratios.

Figure 4-8 depicts a schematic of a typical panel configuration, with Detail Z providing further definition to the geometry of the edge and trapezoidal stiffener. The stiffening system consisted of edge stiffeners and trapezoidal stiffeners. The former were independent of ϑ_2, so their area was the product of their length (T_{Ct}) and breadth (T_S). In contrast, the length of the trapezoidal stiffeners, L_S, depended on ϑ_2. This made L_S a function of trigonometric ratios, $\left(\frac{T_{Ct}}{sin\theta_2}\right)$. The application of the aforementioned angle-pairs within this expression demonstrated that angles within each pair resulted in identical values of L_S. This meant that the angle-pairs; 50° and 130°, 60° and 120°, 70° and 110°, 80° and 100°, provided identical panels, albeit mirrored horizontally.

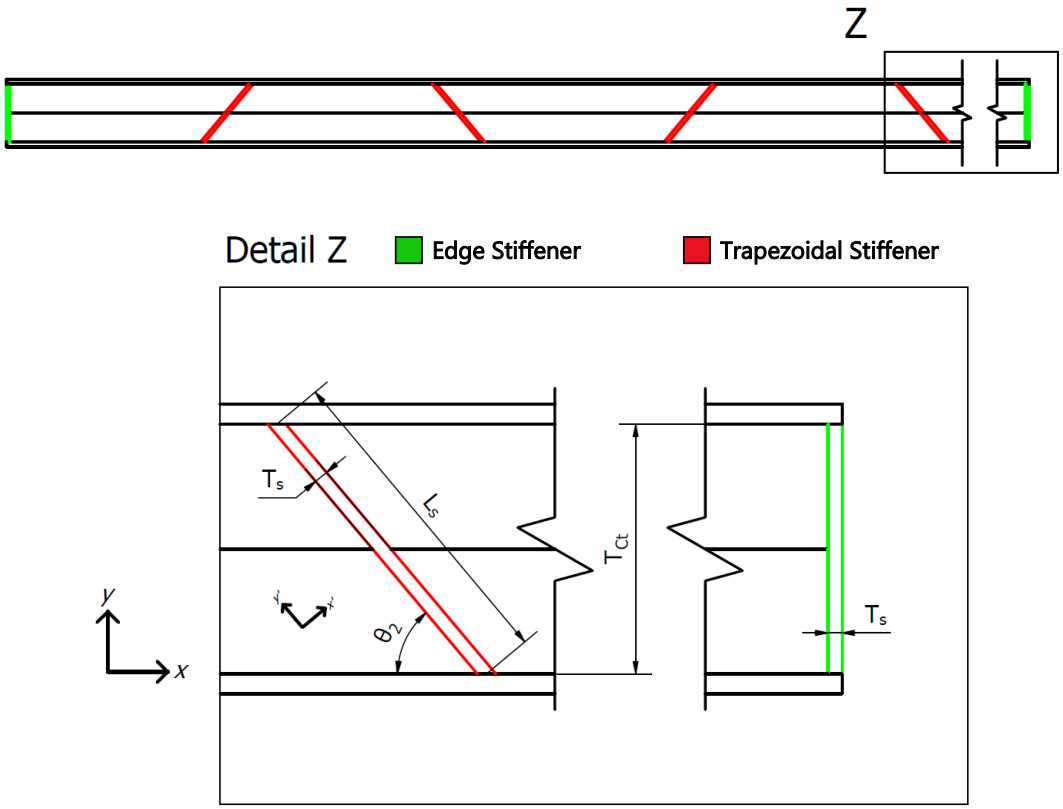

Figure 4-8: Geometric detailing of trapezoidal stiffener

Although it was true that the angle of the stiffener was noted to provide the largest absolute change in deflection for panel *C50F1.2*, with a deflection range of 0.78 mm (simulated), and 0.30 mm (analytical), this change was for practical purposes, noted to have been very small. This was attributed to the limited effect of the stiffener angle on increasing the panel's stiffness, *D*. In fact, for panel *C50F1.2* changing the angle from 90° to 50° increased the panel's stiffness by 0.24%, whilst for panel *C100F4.0*, this increased by 0.33%. Consequently, considering geometric simplification and the associated reductions in labour intensity and production costs provided by an orthogonal stiffening system, the optimal stiffener angle for minimizing vertical deflection was found to be 90°. In this regard, it was suggested that for a more flexible panel design, greater improvements in deflection may have been achieved.

4.1.2. Material Cost & Panel Mass

As conducted in *Section 4.1.1*, in further analysing the relationship between the panel's material cost and mass, the relevant two-dimensional plot was extracted from Figure 3-13. As in the case of Figure 3-13, trendlines denoted by $\boldsymbol{C}T_{Ct}$, and $\boldsymbol{F}T_{Ft}$ were set up to indicate configurations of constant core, and facesheet thickness, respectively. Refer to Figure 4-9. Note that for the purposes of this subsection, the associated legend in such figures is to be ignored. Such terms are related to the *non-dominated sorting algorithm*, and further defined in the discussion on the optimal panel configuration and will be referred to in S*ection 4.2*.

As observed from the material cost vs panel mass plot, a directly proportional relationship was identified to be present. This was expected owing to the linear cost expression described in *Section 3.2.2*, Table 3-7. From Figure 4-9, it was noted that the input parameters did not exert the same degree of influence on the panel's mass and material cost. In this regard, it was identified that a stepwise increase in facesheet thickness was 1.8 times the cost increase of a stepwise increase in core thickness, and 2.7 times the mass increase of a stepwise increase in core thickness. This was attributed to the lower cost per unit volume and density associated with the core materials. This implied that in minimizing the material cost and panel mass, increments in core thickness were noted to precede those in facesheet thickness.

As seen from the error bars in Figure 4-9, the effectiveness of the angle of the stiffening system, for different core and facesheet thicknesses was noted to have remained the same on both axes. The average change in material cost, and panel mass derived from changes in the angle of the stiffening system were noted to be ± €4.28, and ± 0.26 kg, respectively. With respect to a panel's overall material cost and mass, these were noted to contribute minimally. For illustration purposes, considering the lightest and cheapest panel configuration considered in this dissertation, i.e. *C50F1.2*, the largest possible contribution provided by the angle of the stiffening system on the panel's overall material cost, and mass was 2.37%, and 1.86%, respectively.

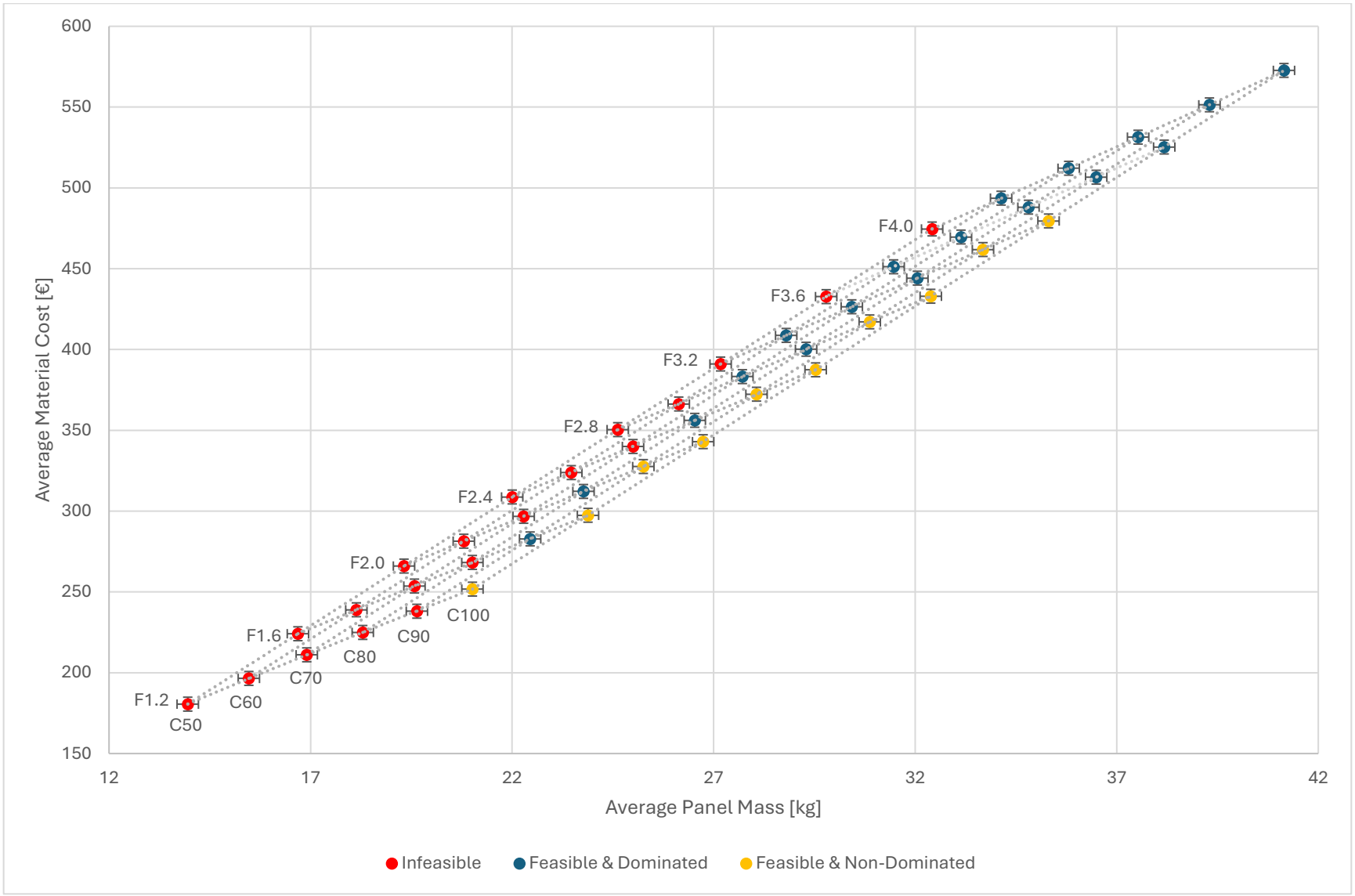

Figure 4-9: Graph of average material cost [€] vs average panel mass [kg] for configurations of constant core and facesheet thickness.

4.1.3. Von Mises Stress

In further assessing the behaviour of the input parameters, corresponding Von Mises stress contours were analysed. For this purpose, configuration *A90C50F1.2* was set as the reference configuration. The following pairs were assessed in studying the effects of core thickness, facesheet thickness, and stiffener angle, respectively; *A90C70F1.2* and *A90C100F1.2*; *A90C50F2.0* and *A90C50F4.0*, and; *A50C50F1.2* and *A70C50F1.2*. Note that only half of the angle domain was considered in the case of the stiffener angle. This decision was made due to the suggested symmetry in performance around the 90^{o} angle, as discussed in *Section 4.1.1.2*.

Additionally, configurations *A50C100F1.2* and *A50C50F4.0* were also studied. This was done to determine the effects of the angle of the stiffening system on panel configurations with relatively large core and facesheet thickness values.

For the purposes of this discussion, only stress contours corresponding to minimum and maximum input parameters were shown. This was done as it was noted that the effects imparted by, for instance, configuration *A90C70F1.2*, were the same as those imparted by configuration *A90C100F1.2,* although to a lesser degree. For this reason, discussing the effects imparted by the maximum input parameters with respect to the minimum parameters was noted to be sufficient in providing a coherent understanding of the effects imparted by the input variables. The complete set of stress contours can be observed in *Appendix B.3*.

Also note that due to the nature of loading and boundary conditions, at its longitudinal midplane, the panel was noted to be subjected to pure bending at its midspan, and shear at its boundaries

4.1.3.1. Panel Components

For each panel configuration, contours of the bottom facesheets were shown in plan. Contours of the top facesheet were also generated; however, owing to similarities in both pattern and stress magnitudes, it was decided not to exhibit these in this section. They could be found in *Appendix B.3*. For either the bottom or the top facesheet, due to symmetry present in both axes, the associated Von Mises stress contours depicted only a quarter of the panel in plan. Additionally, also note that the bottom facesheet stress contours pertaining to configurations *A50C100F1.2* and *A50C50F4.0* were not included with the rest of the configurations shown in Figure 4-10. This was done because little-to-no difference was present in such contours compared to their respective 90^{o} configurations. For this reason, the Von Mises stress contours pertaining to such configurations may be found in *Appendix B.3.*

Furthermore, for the purposes of this discussion, only the contour associated with stiffener *E* was discussed. This was conducted in relation to its adjacent core, core *#5*. The selection of such stiffener and core was based on monitoring the stress behaviour of the worst-conditioned trapezoidal stiffener and its adjacent core. Given that out-of-plane stresses were induced due to the panel's bidirectional behaviour, stiffener *E* was noted to be the worst-conditioned trapezoidal stiffener. With this understanding and owing to symmetry along the longitudinal plane, stiffener *B* and core *#1* would have also sufficed.

The following discussion delved into the general trends shown for the different components making up the GFRP sandwich panel. Due to similarities between the analysed configurations, the trends observed were noted to be applicable to all configurations.

Consider the bottom facesheets (Figures 4-10A – D). As expected, and as previously described in S*ection 2.2*, the facesheets were noted to predominantly function in resisting the bending moment applied. In fact, the maximum stress in the bottom facesheet was consistently noted to occur at the transverse midplane. However, in regions near a stiffener, stress values were observed to be lower. This reduction in stress was attributed to a localized increase in the second moment of area of the facesheets caused by the presence of the stiffener.

Additionally, varying values of stress were observed transversely across the panel. The trend indicated that the free end of the panel was consistently subjected to higher stress states. As shown in the stress contour near the boundary in Figures 4-10A – D, the rate of change of stress in the transverse direction was nonlinear. These phenomena were attributed to the findings discussed in *Section 5.2.1,* where the panel's orthotropic behaviour, resulting from its material and geometric properties, led to its bidirectional behaviour.

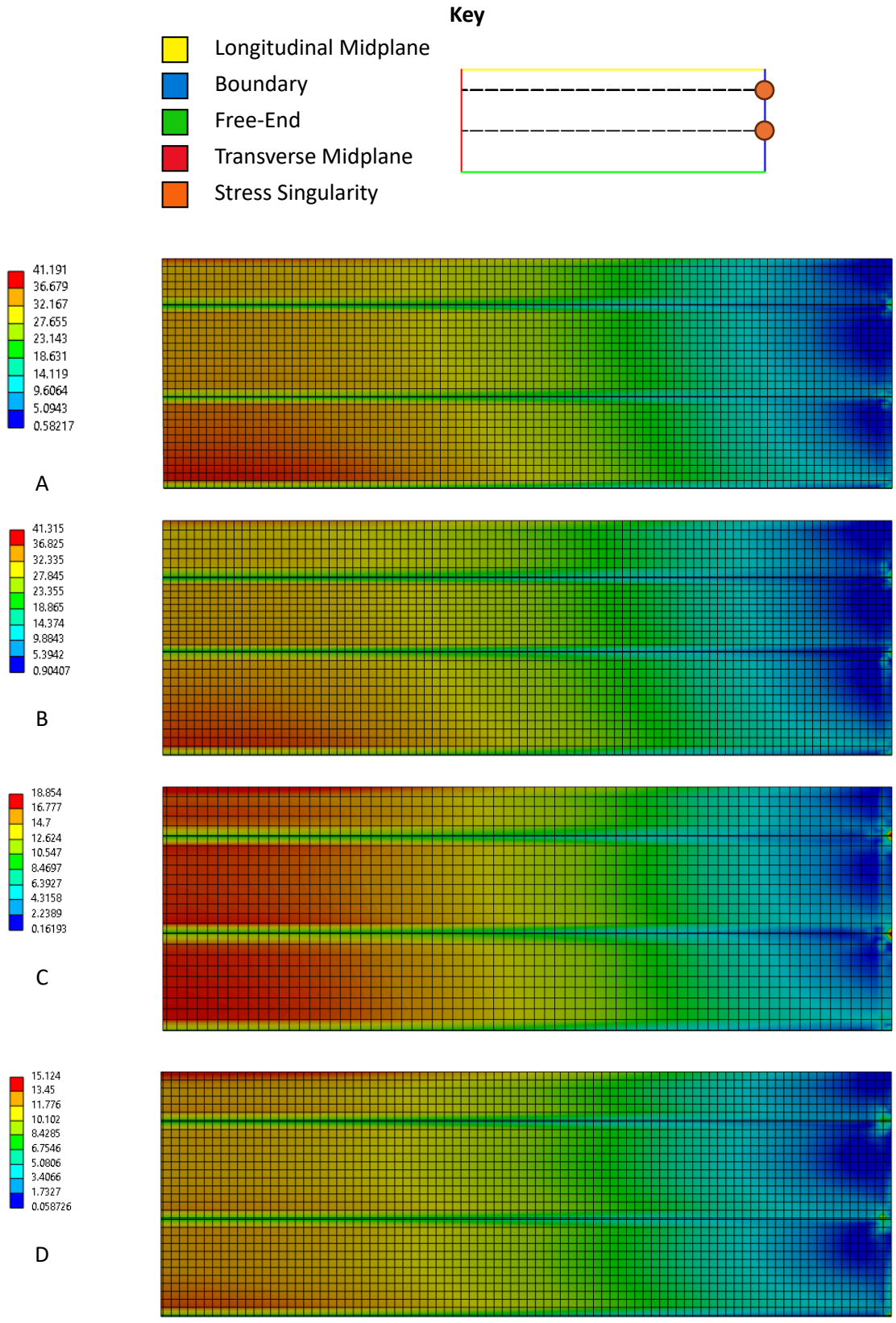

Figure 4-10: Von Mises stress (MPa) contour of bottom facesheet for configuration: (A) A90C50F1.2; (B) A50C50F1.2; (C) A90C100F1.2; (D) A90C50F4.0.

It is important to note that stress singularities were present in the bottom facesheet. These singularities existed at the boundaries and were derived from the simplified 2D modelling of the stiffening system. For the purposes of this discussion, the stress values associated with these singularities were ignored. This was reflected in the accompanying legends in Figures 4-10A – D.

As shown in Figures 4-11A – F, green colour bands were consistently noted to be present along the longitudinal direction, for stiffener *E*. This differed from what occurred for bottom facesheet, in which a high-stress state was identified solely at the midspan, not consistently at both ends. This implied that the stiffener functioned in resisting both shear and bending.

As described in the case of the bottom facesheet, stress singularities were also present in stiffener *E*. These singularities were also located at the boundaries and were identified to have occurred for the same reason stated before. For the purposes of this discussion, the stress values associated with these singularities were ignored. This was reflected in the accompanying legends in Figures 4-11A – F.

Next, the Von Mises stress contours of core *#5* (Figures 4-12A – F) were considered. As expected, and as described in *Section 2.2*, such cores predominantly functioned in shear. This was evident from the increasing stress values observed closer towards the panel's boundary. Additionally, higher stress values were attributed to the bottom core. As described in Eq. 2.5 in *Section 2.3*, this occurred due to the increased stiffness of the bottom core. Despite this, the stress values across the cores were very small in relation to those observed in the surrounding components. In all cases, these were smaller than 0.6 MPa.

The fact that the Von Mises stresses within the core were so small implied that the shear force at the boundary was predominantly passing through the stiffener and not the core. This, along with the fact that the core no longer separated the facesheets as it would have in an unstiffened GFRP sandwich panel, indicated that the core had little-to-no structural functionality in this configuration. However, Tuwair et al. (2015) argued that the core still played a pivotal role within the GFRP sandwich panel. It provided adjacent restraint to the stiffening system and the top facesheet, helping to mitigate buckling of these components. In light of this, concerns were raised about whether the findings of Manjusha et al. (2020), which were applied in this dissertation, were applicable to a stiffened GFRP sandwich panel, and whether the implemented core configuration was the optimal configuration for satisfying the new structural function of providing adjacent restraint.

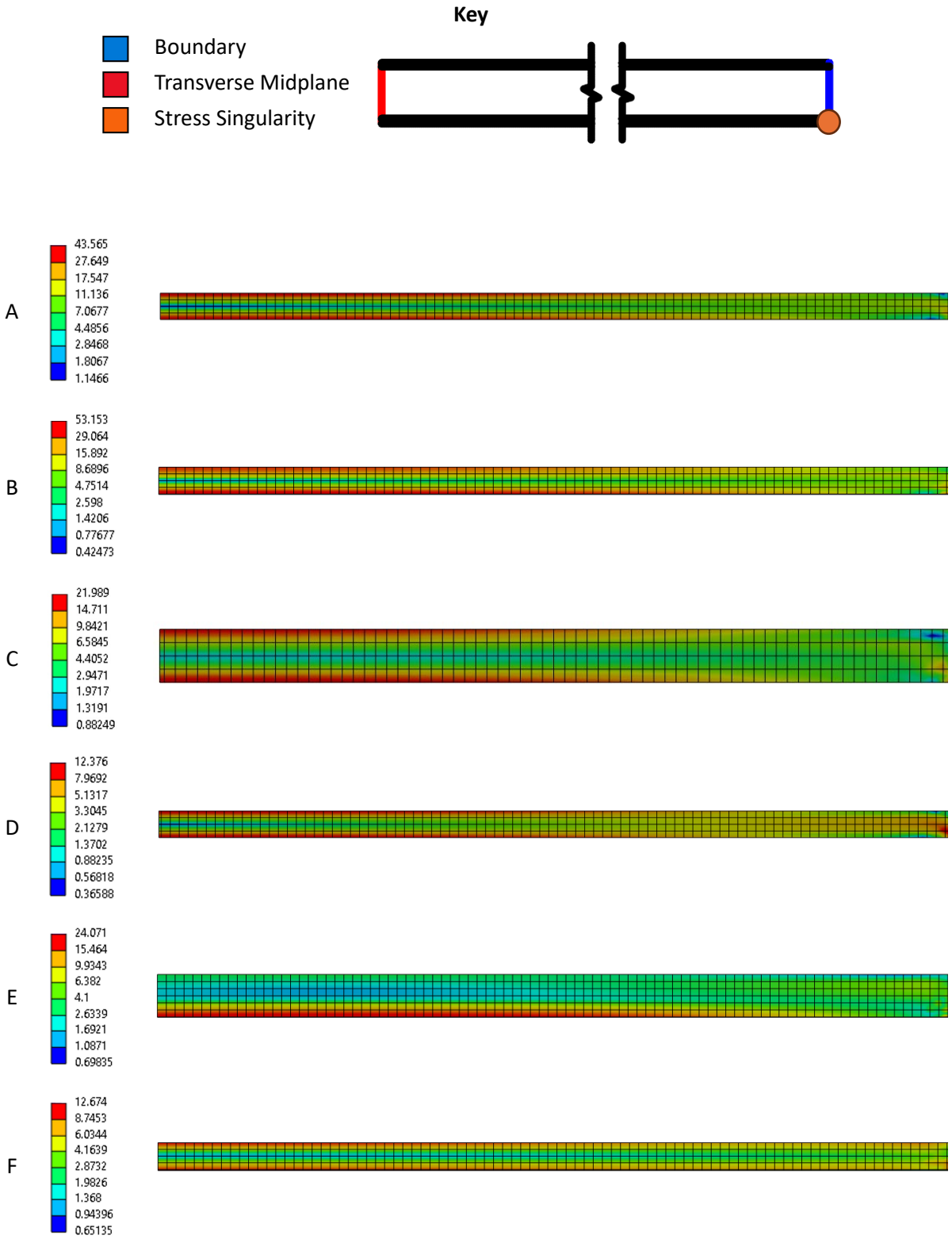

Figure 4-11: Von Mises stress (MPa) contour of stiffener E: (A) A90C50F1.2; (B) A50C50F1.2; (C) A90C100F1.2; (D) A90C50F4.0; (E) A50C100F1.2; (F) A50C50F4.0

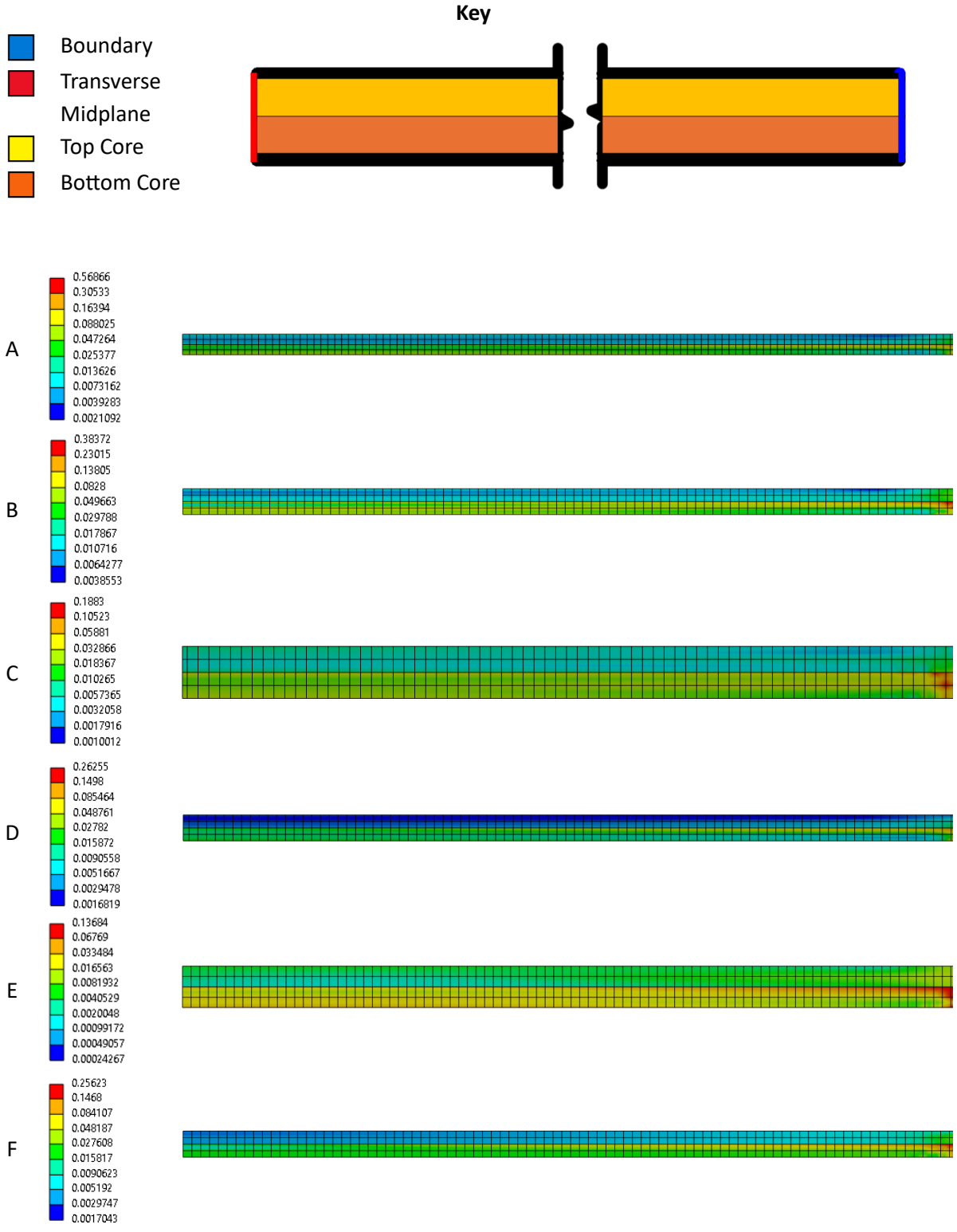

Figure 4-12: Von Mises stress (MPa) contour of core #5: (A) A90C50F1.2; (B) A50C50F1.2; (C) A90C100F1.2; (D) A90C50F4.0; (E) A50C100F1.2; (F) A50C50F4.0.

4.1.3.2. Component Comparison

The focus of this subsection was to determine the effects of the input variables on the panel's components, in terms of Von Mises stresses. This was done through a comparative analysis, with panel *A90C50F1.2* serving as the reference panel. Comparative analysis was conducted by considering the change in maximum Von Mises stress for corresponding components in different panel configurations. In this regard, the same components described in *Section 4.1.3.1* were reconsidered. The results were presented as a ratio with respect to the reference panel in Figure 4-13.

Comparisons between the reference configuration (Figures 4-10A, 4-11A, and 4-12A), panel *A90C100F1.2* (Figures 4-10C, 4-11C, and 4-12C), and panel *A90C50F4.0* (Figures 4-10D, 11D, and 12D), showed that panels with maximum core or facesheet thickness exhibited a global reduction in stress states, with all concerning components showing a decrease in stress.

The degree of reduction varied among the different components. For panel *A90C50F4.0*, the bottom facesheet and stiffener *E* showed larger reductions in stress state compared to the same components in panel *A90C100F1.2*. The reductions relative to panel *A90C100F1.2* were observed to be 9.05% for the bottom facesheet, and 22.07% for stiffener *E*. For core *#5*, panel *A90C100F1.2* showed larger stress reductions compared to panel *A90C50F4.0*, with a noted difference of 7.57%.

These observations suggested that increasing facesheet thickness was more effective in reducing stresses in the facesheet and stiffening system. The latter was expected owing to the proportionality defined between the facesheet and the stiffener thickness, where increasing facesheet thickness resulted in increased stiffener thickness. Refer to *Section 3.2.2*, Table 3-6.

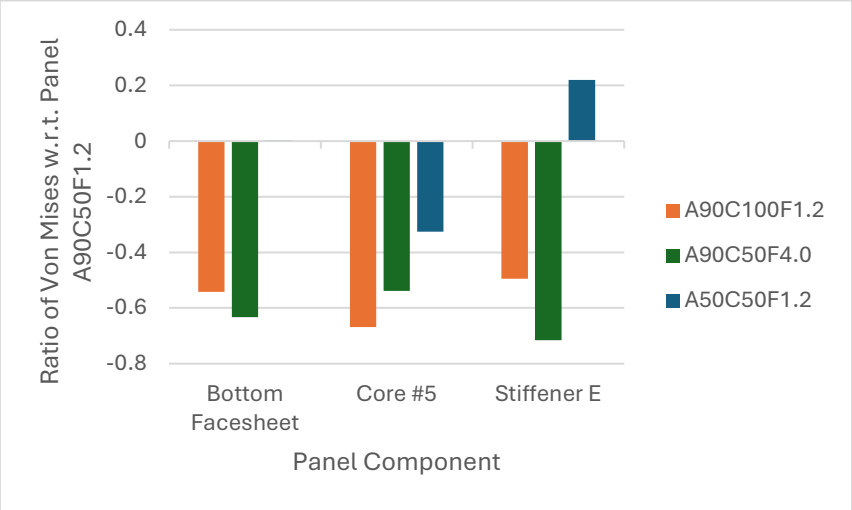

Figure 4-13: Comparative Von Mises analysis for the top facesheet, core #5, and stiffener E, for panels A90C100F1.2, A90C50F4.0, and 50C50F1.2 with respect to panel A90F50F1.2.

In the case of the facesheets, Eq. 2.3, described in *Section 2.3,* suggested that this occurred due to the larger $\frac{y}{D}$ ratio associated with stepwise increments in core thickness compared to stepwise increments in facesheet thickness. In fact, when calculated for the respective panel configurations, panel *C100F1.2* was found to have a $\frac{y}{D}$ ratio 35.03% larger than that of panel *C50F4.0*.

On the other hand, it also suggested that increasing core thickness was more effective in reducing the stresses in the cores. In fact, Eq. 2.5, described in *Section 2.3,* indicated that this was due to the higher $\frac{S}{D}$ ratio associated with stepwise increments in core thickness compared to facesheet thickness.

When comparing the stress contours of panel *A50C50F1.2* (Figures 4-10A, 4-11A, and 4-12A) with respect to the reference panel, little difference was noted in the trends shown. However, significant changes in stress state were observed in the concerning components. These changes were summarized in Figure 4-13, via the blue bar graphs. The largest change in stress state was observed in core *#5*, where the maximum stress decreased by 32.5%. Stiffener *E*, on the other hand, showed an increase in stress state of 22.01%, while the stress state of the bottom facesheet remained unchanged. This observation suggested that a portion of the force that originally passed through the core in the reference configuration was, for panel *A50C50F1.2*, being transferred into the stiffening system. This phenomenon was consistent with observations by Mohamed et al. (2015).

The same was noted in the case of configurations *A50C100F1.2* (Figure 4-11E, and 12E) and *A50C50F4.0 (*Figure 4-11E, and Figure 4-12F), albeit for their respective 90^{o} configurations. The difference observed between these configuration pairs, and the previously discussed configuration pair, was in the degree of stress change shown. In the case of configuration *A50C100F1.2*, the stress reduction shown in the core was 27.3%, whilst for panel *A50C50F4.0*, this was 2.41%. These corresponded to an increase in the maximum stress state of stiffener *E.* For panel *A50C100F1.2*, this increase was 9.47%, whilst for panel *A50C50F4.0*, this was 2.41%. This suggested that the effect of the angle of the stiffening system was a function of core and facesheet thickness, with higher weighting given to the latter. This was conceptually similar to what was described in *Section 4.1.1.2*, where the effectiveness of the angle of the stiffening system on the panel's vertical deflection diminished with increased facesheet thickness.

In this scenario, due to significant changes in stress state caused by variations in the angle of the stiffening system, the optimal angle was identified as a function of facesheet thickness. For relatively thick facesheets, where the angle's contribution was minimal, the optimal angle was found to be 90^{o}. This aligned with the rationale presented in Section *4.1.1.2*. However, for panels with relatively thin

facesheets, where the angle of the stiffening system had a significant impact (such as in panel *C50F1.2*), the optimal angle was noted to be 50^{o} (or 130^{o} by symmetry).

4.2. Determination of Optimal Panel Configuration

This section delves into the rationale applied in determining the optimal panel configuration from a total of 432 configurations. In achieving this, a three-step process was applied.

In structural engineering, when designing flooring systems, engineers seek to minimize the vertical deflection of the concerning system in pursuit of safety (ultimate limit state) and comfort (serviceability limit state). Owing to this dissertation's commitment in furthering the body of knowledge with respect to the implementation of GFRP sandwich panels within domestic environments, a maximum vertical deflection of 8.33 mm $\left(= \frac{L}{360} = \frac{3000}{360}\right)$ was imposed. Panel configurations noted to have exceeded this vertical deflection were disqualified from the optimisation process. These were denoted in Figures 3-13, 4-1, 4-2, and 4-9, in red, and by the term *infeasible*. Panel configurations noted not to have exceeded this vertical deflection value were further analysed via the *non-dominated sorting algorithm*. In Figures 3-13, 4-1, 4-2, and 4-9 these panels were denoted in blue and yellow, and labelled *feasible.*

As seen from Figures 3-13, 4-1, and 4-2, it was noted that configurations, such as *C90F2.0,* although successful in exhibiting a vertical deflection of less than 8.33 mm, were identified to have been outperformed, i.e. dominated, by alternative panel configurations. Consider configuration *C80F2.0*, and configuration *C100F1.2,* whose output variables were noted by (€312.19, 23.77 kg, 8.31 mm) and (€251.74, 21.02 kg, 8.18 mm), respectively. Configuration *C80F2.0* was dominated by panel *C100F1.2*, in that panel *C100F1.2* was noted to be lighter, cheaper and stiffer. The panel configurations noted to have been *non-dominated* were all identified to be optimal panel configurations for their associated maximum vertical deflection value. In this manner, the panels termed *feasible* were either classified as *dominated* or *non-dominated*. In Figures 3-13, 4-1, 4-2, and 4-9, configurations labelled as *feasible* and *dominated* were represented in blue, while configurations labelled as *feasible* and *non-dominated* were represented in yellow.

Note that, as identified in *Section 4.1.1*, error was noted to be present within the predicted data set. In turn, this caused configurations to be labelled *dominated* as opposed to *non-dominated*, and vice versa. Nevertheless, this was not found to have hindered the ultimate selection of the optimal panel configuration.

In identifying the optimal panel, configurations from the *non-dominated* set were considered. Here, observations noted in the previous subsections were applied. These were tabulated in Table 4-1.

Table 4-1: Summary of observations identified in this dissertation pertaining to the effects of the input variables on the output variables.

#	Observation	Section #
1	In increasing the panel's stiffness, increments in core thickness were identified to be more effective than increments in facesheet thickness.	4.1.1.1
2	Angles ≠ 90^o were noted to increase the stiffness of the panel. In this regard, a symmetric parabolic relationship was shown, with maximum stiffness being imparted at ϑ_1 = 50^o (and by symmetry, 130^o).	4.1.1.2
3	Effectiveness of stiffening system on the panel's vertical deflection was noted to reduce with increasing values of facesheet thickness. In any case, it was noted that for all panel configurations the absolute change in deflection recorded for all panel configurations, was for practical purposes, insignificant.	4.1.1.2
4	Increases in core thickness were noted to be both more mass-efficient, and cost effective compared to increases in facesheet thickness.	4.1.2
5	Variations in the angle of the stiffening system had no appreciable effect on the panel's mass and associated material cost.	4.1.2
6	Compared to the reference configuration, increases in facesheet thickness were found to bring higher stress reductions in the facesheet and in the stiffening system than increases in core thickness.	4.1.3.2
7	Compared to the reference configuration, increases in core thickness were found to bring higher stress reductions in the core than increases in facesheet thickness.	4.1.3.2
8	Compared to the reference configuration, varying the angle of the stiffening system (ϑ_1 ≠ 90^o) was found to reduce the stress state in the core, increase it in the stiffening system, and maintain it in the facesheets.	4.1.3.2
9	Stress reductions derived form varying the angle of the stiffening system were noted to diminish for increasing core and facesheet thicknesses, with facesheet thickness having had a more significant impact. Consequently, this meant that for relatively thick facesheets, the optimal stiffener angle was 90^o, while for thinner facesheets, it was 50^o (or 130^o by symmetry).	4.1.3.2

Based on the observations in Table 4-1, preference was given to panels with increasing core thickness and minimal facesheet thickness. This was because, as described in the table, stepwise increments in core thickness resulted in greater increases in panel stiffness, while also being mass-efficient and cost-effective. Additionally, these increments reduced stresses in the core, further mitigating the risk of core failure[vii]. In this manner, the optimal core-facesheet configuration was noted to be the configuration from the *feasible* and *non-dominated* set, with the thickest core, and thinnest facesheet.

[vii] This was discussed in *Section 2.5* to be the predominant mode of failure for GFRP sandwich panels.

This dissertation has demonstrated that determining the optimal stiffener angle should be based on Von Mises stresses rather than vertical deflection. As was shown in *Section 4.1.1.2*, the impact of the stiffening system on the panel's vertical deflection was insignificant for practical purposes. Therefore, selecting the optimal stiffener based on Von Mises stresses meant that it depended on the thickness of the facesheet. Specifically, if a panel configuration from the *feasible & non-dominated* set had a minimal facesheet thickness, the optimal angle was identified to be 50^{o} (or 130^{o}, by symmetry). Conversely if no configuration in this set had a relatively thin facesheet, the optimal angle was determined to 90^{o}.

Referring to Figures 3-13, 4-1, 4-2, and 4-9, a panel with a facesheet thickness of 1.2 mm and a core thickness of 100 mm was identified within the dataset. Based on the described rationale, given the panel's facesheet thickness of 1.2 mm, the optimal stiffener angle was determined to be 50^{o} (or 130^{0}, by symmetry).

4.3. Concluding Remarks

Based on this understanding, the panel configuration that satisfied all criteria was identified as panel *A50C100F1.2* (or by symmetry, *A130C100F1.2*). Hence, these findings indicated that for use as a monolithic slab in domestic environments, the optimal trapezoidally-stiffened, bilayer GFRP sandwich panel consisted of a 100 mm core with an upper 50 mm layer of low-density PU foam, and a lower 50 mm layer of high-density PU foam. Additionally, it included a 1.2 mm GFRP facesheets, and a GFRP stiffening system, inclined at 50^{o} (or by symmetry, 130^{o}). In optimizing the panel in terms of vertical deflection, panel mass, and material cost, the resulting values were noted to be 8.12 mm, 20.96 kg (6.97 kg/m^2), and €256.73 (85.58 €/m^2).

However, it was important to highlight that due to several limitations and simplifications encountered in this dissertation, further research is needed to provide a definite answer to the research question it aimed to address. Therefore, the concluding chapter of this dissertation summarized the dissertation's research objectives and contributions to knowledge, discussed its limitations, and suggested avenues for future research.

5. Conclusion

Due to their high strength-to-weight ratio, GFRP sandwich panels may prove to be a novel solution within the construction industry, particularly in weight-sensitive cases. The main goal of this dissertation was to contribute to the body of knowledge regarding the development and application of composite materials in construction. This study specifically investigated the structural behaviour of GFPR sandwich panels, without considering their environmental impact. Given that core failure is the predominant failure mode of such panels, this was achieved by investigating novel core-strengthening techniques in GFRP sandwich panels used as monolithic slab members in domestic environments.

To address this, this dissertation aimed to answer the following research question:

"What would be the optimal configuration for a trapezoidally-stiffened, bilayer GFRP sandwich panel, used as a monolithic slab, in domestic environments?"

This dissertation identified two main objectives. The first objective was to study the effects imparted by the core thickness, facesheet thickness, and the angle of the panel's stiffening system on the panel's vertical deflection, mass, material cost, and Von Mises stresses. The second was to optimize a standard-sized trapezoidally-stiffened, bilayer GFRP sandwich panel in terms of vertical deflection, panel mass, and material cost, while also considering Von Mises stresses. This was done to assess how variations in these input variables impact the panel's performance.

5.1. Design of GFRP Sandwich Panel

The design of the GFRP sandwich panel that was optimized was conducted on the basis of current literature pertaining to the development of stiffened core material systems, and multilayer core systems. This was done with the aim of developing a hybrid core material system. The designed hybrid GFRP sandwich panel was based on a standard 3 m by 1 m panel configuration, constituting of a bilayer core, sandwiched between top and bottom GFRP facesheets. The core was composed of a high-density PU foam at the bottom, and a low-density PU foam at the top, and designed to include a total of six stiffeners; two edge stiffeners, and four trapezoidal stiffeners.

5.2. Effect of Input Variables

The three input variables considered in this dissertation were; core thickness, facesheet thickness, and stiffening system's angle. Their effects were studied with respect to the panel's vertical deflection, panel mass, material deflection, and Von Mises stress contours through finite element analysis.

5.2.1. Vertical Deflection

In terms of vertical deflection, the contribution of stiffening the GFRP sandwich panel varied depending on whether the increments were in core thickness or facesheet thickness. Specifically, a 5.41% difference in vertical deflection was observed when increasing core thickness stepwise from 50 mm compared to a stepwise increase in facesheet thickness from 1.2 mm. This difference was analytically attributed to the core thickness having a greater influence on the panel's second moment of area.

Varying the angle of the stiffening system was found to exhibit a parabolic relationship with the panel's vertical deflection. For each panel considered, this relationship was symmetric about the 90^{o} angle, reaching a minimum at 50^{o} and 130^{o}. This also indicated that panels of the following pairs were geometrically symmetric; 50^{o} and 130^{o}, 60^{o} and 120^{o}, 70^{o} and 110^{o}, 80^{o} and 100^{o}.

The effectiveness of the angle of the stiffening system was found to be predominantly a function of facesheet thickness. In fact, comparative analysis of configuration pairs *C50F1.2* and *C50F4.0*, and *C100F1.2* and *C100F4.0*, revealed that the range in magnitude for the change in vertical deflection due to change in the angle of the stiffening system decreased by 80%, and 79%, respectively. This reduction was analytically attributed to a decrease in the contribution of the stiffening system to the panel's overall rigidity. Specifically, the stiffness contribution reduced by 2.90% from configuration *C50F1.2* to *C50F4.0*, and by 2.62% from configuration *C100F1.2* to *C100F4.0*.

In any case, it was identified that even for the configuration providing the largest absolute change in deflection (*C50F1.2*), the magnitude of this change was, for practical purposes, insignificant. The absolute deflection change was 0.78 mm (simulated) and 0.30 mm (analytical). This minimal impact across all panel configurations was attributed to the limited effect of the stiffener angle on increasing the panel's stiffness. In fact, for panel *C50F1.2*, changing the angle from 90^{o} to 50^{o} increased the panel's stiffness by 0.24%.

For this reason, as well as the geometric simplifications and associated reductions in labour intensity and production costs provided by an orthogonal stiffening system, the optimal stiffener angle for minimize vertical deflection was found to be 90^{o}.

5.2.2. Panel Mass & Material Cost

As it pertains to the material cost of the GFRP sandwich panel, it was identified that stepwise increments in facesheet thickness (i.e., 1.2 – 4.0 mm, at 0.4 mm steps) were 1.8-fold more expensive than in core thickness (i.e., 50 – 100 mm, at 10 mm steps). Additionally, it was also noted that, relative to a stepwise increase in core thickness, a 2.7-fold increase in panel mass was noted for a stepwise increase in facesheet thickness. This was attributed to the lower cost per unit volume, and density associated with the core materials relative to the facesheet and stiffener material. Variations in the stiffener angle were found to have had no significant effect on the panel's mass and material costs, with the maximum increase attributed to changing the angle of the stiffening system being 2.37%, and 1.86%, respectively.

5.2.3. Von Mises Stress

Analysis of the Von Mises stress contours revealed that increasing facesheet and core thicknesses led to a global reduction in stress levels across the panel. However, the extent of reduction varied among different components. Specifically, panel *A90C50F4.0* showed significant stress reductions in the bottom facesheet (9.05%), and stiffener *E* (22.07%) compared to panel *A90C100F.2*. Conversely, panel *A90C100F1.2* exhibited greater stress reductions in core *#5* (7.57%) relative to panel *A90C50F4.0*. These findings indicated that increasing facesheet thickness was more effective in reducing stresses in the facesheet and stiffening system, whereas increasing core thickness was more effective in reducing stresses in the core.

Lower stress levels were also observed in core *#5* when a stiffener angle of 50^{o} was adopted. Specifically, panels *A50C50F1.2*, *A50C100F1.2*, and *A50C50F4.0* consistently exhibited reduced stress states in core *#5* compared to their counterparts with a 90^{o} stiffener angle. These reductions were noted to be 32.5%, 27.3%, and 9.47%, respectively. However, this reduction in core stress was accompanied by increases in stress in stiffener *E*. Specifically, panels *A50C50F1.2, A50C100F.2,* and *A50C50F4.0* showed increases of 22.01%, 9.47%, and 2.41%, respectively.

This demonstrated that when the stiffener angle deviated from 90^{o}, reductions in the stress state of the core were accompanied by increases in stress within the stiffening system. Additionally, it indicated that the extent of stress reduction in the cores depended on the thickness of the facesheets, with thicker facesheets minimizing the influence of the stiffener angle.

In all configurations where the stiffener angle was varied, no significant change was observed in the stress state of the bottom facesheet. This observation suggested that when altering the stiffener

angle, a degree of the force that previously passed through the core in an orthogonal stiffener system was now redirected through the stiffening system.

In this manner, the optimal angle was identified as a function of facesheet thickness. For relatively thick facesheets, the optimal angle was found to be 90°, while for relatively thin facesheets, this was found to be 50° (or by symmetry, 130°)

5.3. Optimal Panel Design

In identifying the optimal panel configuration for the purposes of domestic buildings, a three-step process was applied. First, owing to the design of a monolithic slab within domestic environments, the deflection limit was set to $\frac{L}{360}$. This was adopted on the basis of similarly focused studies, highlighted in the literature review. In this manner, panel configurations whose vertical deflection exceeded 8.33 mm $\left(= \frac{3000\ mm}{360}\right)$ were omitted from selection. These were termed *infeasible*. Next, on the basis of the *non-dominated sorting algorithm*, which was defined in *Section 3.2.5*, configurations noted to have been dominated were discarded. These were termed *feasible & dominated*, while their counterparts were termed *feasible & non-dominated*. In determining the optimal panel configuration from the latter solution set, the same observations identified in this dissertation pertaining to the effects of the input variables on the output variables, were applied. Increments in core thickness were favoured to increments in the facesheet thickness. This was because, as discussed in *Section 5.2.1* and *Section 5.2.2,* stepwise increments in core thickness resulted in greater increases in panel stiffness, while also being mass-efficient and cost-effective. It also resulted in reduced stresses in the core, thus further mitigating the risks of core failure.

Based on the findings of *Section 5.2.1* and *Section 5.2.3*, it was determined that the optimal stiffener angle should be based on Von Mises stresses rather than vertical deflection. Consequently, the optimal stiffener angle was found to be a function of facesheet thickness. In this manner, if a panel with minimal facesheet thickness was identified within the *feasible & non-dominated* solution set, the optimal stiffener angle would be 50° (or by symmetry, 130°). Otherwise, the optimal angle would be 90°.

In this regard, from the *feasible & non-dominated* solution set, a panel with a facesheet thickness of 1.2 mm and a core thickness of 100 mm was identified. As such, the optimal stiffener angle was determined to be 50° (or by symmetry, 130°).

5.4. Research Question

In answering the research question, the optimal configuration for a trapezoidally-stiffened, bilayer GFRP sandwich panel used as a monolithic slab in domestic environments was identified as *A50C100F1.2* (and by symmetry *A130C100F1.2)*. This configuration consisted of a 100 mm core with an upper 50 mm layer of low-density PU foam, and a lower 50 mm layer of high-density PU foam. Additionally, it included 1.2 mm thick top and bottom GFRP facesheets, and a GFRP stiffening system, inclined at 50^{o} (and by symmetry, 130^{o}). In optimizing the panel in terms of vertical deflection, panel mass, and material cost, the resulting values were noted to be 8.312 mm, 20.96 kg (6.97 kg/m^2), and €256.73 (85.58 €/m^2)

5.5. Limitations & Further Research

Although for the scope of this dissertation, it has been identified that panel *A50C100F1.2* (and by symmetry panel *A130C100F1.*2) was the optimal panel configuration, it must be noted that further research is to be conducted in verifying such a claim. The following serve to provide further explanation in this regard.

- Software
    - In this dissertation, owing the use of the student version of *ANSYS Workbench* (ANSYS, Inc., 2023), limitations were noted to had been set on the number of elements authorized for meshing. Consequently, this imposed simplifications in the design of the panel, particularly within the stiffening system, as well as limitations on the degree of accuracy achieved within the generated numerical models. In this regard, further research through more detailed stiffener designs, and higher quality meshes, would need to be done in further verifying the findings of this dissertation.
- Material Nonlinearity
    - Due to the nonlinear viscoelastic stress-strain relationship of the polyurethane foam, further research is to include a nonlinear material analysis, with special interest given to the effects of creep.
- Modifications to Panel Design
    - In this dissertation, the stiffener spacing-thickness ratio used was noted to have been applicable to a system of orthogonally-aligned longitudinal stiffeners. It was noted that in further contributing to the mass- and cost-reductions of the panel designed in this dissertation, the stiffener spacing-thickness ratio pertaining to a system of trapezoidal longitudinal stiffeners is to be investigated. In this manner, in the case that higher stiffener spacing-thickness ratios were to be achieved, mass- and cost-

reductions are noted to take place to the trapezoidally-stiffened, bilayer GFRP sandwich panel, owing to a decrease in the number of stiffeners required.

  - The optimal panel configuration was based on a bilayer core system. The introduction of the stiffening system changed the role of the core, from predominantly resisting the applied shear to providing adjacent restraint to the top facesheet and the stiffening system. Therefore, further research is needed to identify the optimal core configuration for the core's new function.

- Laboratory Testing
  - The nature of the work conducted in this research was purely based on FE models, and analytical calculations. A comparative analysis of the results obtained should be made with respect to laboratory tests. This is to be done to further substantiate the validity of the numerical modelling conducted in this dissertation, as well as to outline observations that were missed in this dissertation, owing to the simplifications adopted.

Bibliography

Abbood, I. S., Odaa, S. a., Hasan, K. F., & Jasim, M. A. (2021). Properties Evaluation of Fiber Reinforced Polymers & their Constituent Materials used in Structures - A Review. *Materials Today: Proceedings* (pp. 1003-1008). Elsevier.

Allen, H. G. (1969). Formulae for Analysis. In H. G. Allen, *Analysis and Design of Structural Sandwich Panels* (pp. 227-244). London: Pergamon Press.

Allen, H. G. (1969). Sandwich Beams. In H. G. Allen, *Analysis and Design of Structural Sandwich Panels* (pp. 8-47). London: Pergamon Press.

ANSYS, Inc. (2011). Element Classifications. In I. ANSYS, *ANSYS Mechanical APDL Element Reference* (pp. 5-42). Canonsburg: ANSYS, Inc.

ANSYS, Inc. (2021). Nonlinear Structural Analysis. In I. ANSYS, *Structural Analysis Guide* (pp. 217-316). Canonsburg: ANSYS, Inc.

ANSYS, Inc. (2023, May 15). Ansys® Academic Student 2023 R2. Canonsburg, Pennsylvania, United States.

ANSYS, Inc. (2023). Contact. In I. ANSYS, *Mechanical User's Guide* (pp. 1262-1329). Canonsburg: ANSYS, Inc.

ANSYS, Inc. (2023). Quality Group. In I. ANSYS, *ANSYS Meshing User's Guide* (pp. 115-153). Canonsburg: ANSYS, Inc.

ANSYS, Inc. (2023). Using Design of Experiments. In I. ANSYS, *DesignXploter User's Guide* (pp. 81-98). Canonsburg: ANSYS, Inc.

Aref, A. J., Alampalli, S., & He, Y. (2004). Performance of a Fiber Reinforced Polymer Web Core Skew Bridge Superstructure. Part I: Field Testing & Finite Element Simulations. *Composite Structures, 69*(4), 491-499.

Arruda, M., & Lopes, B. (2020). Pre-Design Guidelines for GFRP Composite Sandwich Panels. *Engineering Solid Mechanics*, 169-186.

Barbero, E. J. (2018). Materials. In E. J. Barbero, *Introduction to Copmosite Materials Design* (pp. 37-70). Florida: CRC Press.

Barbero, E. J. (2018). Micromechanics. In E. J. Barbero, *Introduction to Composite Materials Design* (pp. 107-146). Florida: CRC Press.

Barbero, E. J. (2018). Ply Mechanics. In E. J. Barbero, *Introduction to Composite Materials Design* (pp. 151-169). Florida: CRC Press.

Callister, W. D. (2007). Composites. In W. D. Callister, *Materials Science & Engineering: An Introduction* (pp. 577-620). John Wiley & Sons, Inc.

Callister, W. D. (2007). Introduction. In W. D. Callister, *Materials Sceience & Engineering: An Introduction* (pp. 1-13). John Wiley & Sons, Inc.

Campbell, F. C. (2010). Introduction to Composite Materials. In *Structural Composite Materials* (pp. 1-29). Cleveland: ASM International.

Correia, J. R., Garrido, M., Gonilha, J. A., & Branco, F. A. (2012). GFRP Sandiwch Panels with PU Foam & PP Honeycomb Cores for Civil Engineering Structural Applications. *International Journal of Structural Integrity*, 127-147.

EasyComposites. (2016, July 29). Epoxy Laminating Resin EL2. Stroke onTrent, Staffordshire, England.

Elliot, A. J., Windle, A., Eeckhaut, G. J., & Ludwig, W. (2002). In-situ Deformation of an Open-Cell Flexible Polyurethane Foam Characterised by 3D Computed Microtomography. *Journal of Materials Science*, 1547-1555.

European Committee for Standardization. (2001). Actions on Structures - Part 1-1: General Actions - Densities, Self-Weight, Imposed Loads for Buildings. In E. C. Standardization, *EN 1991-1-1 (2002)* (pp. 21-22). European Committee for Standardization.

Fam, A., & Sharaf, T. (2010). Flexural Performance of Sandwich Panels Comprising Polyurethane Core & GFRP Skins & Ribs of Various Configuraitons. *Composite Structures, 92*(12), 2927-2935.

Garrido, M. (2016). *Composite Sanwich Panel Floors for Building Rehabilitation.* Lisbon: Universidade de Lisboa.

Garrido, M., Madeira, J., Proenca, M., & Correia, J. (2019). Multi-Objective Optimization of Pultruded Composite Sandwich Panels for Building Floor Rehabilitation. *Construction & Building Materials*, 465-478.

Jones, R. M. (1999). Introduction to Composite Materials. In R. M. Jones, *Mechanics of Composite Materials* (pp. 1-25). Florida: CRC Press.

Kampner, M., & Grenestedt, J. L. (2007). On Using Corrugated Skins to Carry Shear in Sandwich Beams. *Composite Structures, 85*(2), 139-148.

Keller, T., Haas, C., & Vallee, T. (2008). Structural Concept, Design, and Experimental Verification of a Glass Fiber-Reinforced Polymer Sandwich Roof Structure. *Journal of Composites for Construction*, 1-15.

Keller, T., Rothe, J., de Castro, J., & Osei-Antwi, M. (2013). GFRP-Balsa Sandwich Bridge Deck: Concept, Design, and Experimental Validation. *Journal of Composites for Construction*.

Kooistra, G. W., & Wadley, H. N. (2007). Lattice Truss Structures from Expanded Metal Sheet. *Materials & Design*, 507-514.

Mamalis, A. G., Spentzas, K. N., Pantelelis, N. G., Manolakos, D. E., & Ioannidis, M. B. (2008). A New Hybrid Concept for Sandwich Structures. *Composite Structures, 83*(4), 335-340.

Manalo, A., Aravinthan, T., Fam, A., & Benmokrane, B. (2016). State-of-the-Art Review on FRP Sandwich Systems for Lightweight Civil Infrastructure. *Journal of Composites for Construction*, 1-16.

Manjusha, M., & Althaf, M. (2020). Numerical Analysis on Flextural Behaviour of GFRP Sandwich Roof Panel with Multilayer Core Material. *5th International Conference on Modeling & Simulation in Civil Engineering*, *490*, pp. 1-15. Kerala.

Mastali, M., Valente, I. B., & Barros, J. A. (2013). New Composite Slab System for the Structural Rehabilitation of Traditional Buildings. *11th International Symposium of Fiber Reinforced Polymers for Reinforced Concrete Structures.*

Mohamed, M., Anandan, S., Huo, Z., Birman, V., Volz, J., & Chandrashekhara, K. (2015). Manufacturing & Characterization of Polyurethane Based Sandwich Composite Structures. *Composite Structures*, 169-179.

Noel, M., & Fam, A. (2021). Empirical Design Equation for Compression Strength of Lightweight FRP Sandwich Panel Walls. *Journal of Architectural Engineering*.

Osei-Antwi, M., de Castro, J., Vassilopoulos, A. P., & Keller, T. (2013). FRP-Balsa Composite Sandwich Bridge Deck with Complex Core Assembly. *Journal of Composites for Construction*.

Reis, E. M., & Rizkalla, S. H. (2008). Material Characteristics of 3-D FRP Sandwich Panels. *Construction & Building Materials, 22*(6), 1009-1018.

Roth, L. (2006). Novartis Campus Main Gate & Car Park. Basel, Switzerland.

Sharaf, T., & Fam, A. (2015). Numerical Modelling of Sandwich Panels with Soft Core & Different Rib Configurations. *Reinforced Plastics & Composites, 31*(11), 771-784.

TOPOLO. (2022, October). *PP Honeycomb Panels*. Retrieved from TOPOLO: https://topolocfrt.com/product/high-gloss-pp-honeycomb-panels/

TOPOLO. (2023, May). *PU Foam Sandwich Panels*. Retrieved from TOPOLO: https://topolocfrt.com/product/high-gloss-pp-honeycomb-panels/

Tuwair, H., Volz, J., ElGawady, M., Chandrashekhara, K., & Birman, V. (2015). Finite Element Modeling of Hybrid GFRP Sandwich Bridge Deck Panels Filled with Polyurethane Foam. *5th International Conference on Construction Materials: Performance, Innovations and Structural Implications.*

Vijayan, S. D., Sivasuriyan, A., Devarajan, P., Stefanska, A., Wodzynski, L., & Koda, E. (2023). Carbon Fibre-Reinforced Polymer (CFRP) Composites in Civil Engineering Application - A Comprehensive Review. *Buildings*, 1-26.

Wicks, N., & Hutchinson, J. W. (2001). Optimal Truss Plates. *International Journal of Solids and Structures*, 5165-5183.

Appendices

Appendix A.1.

This appendix aims to provide a basic understanding of different element types, meshing methods and mesh quality metrics.

First consider the term *element* within *finite element analysis* (FEA). An element serves as the fundamental unit used to discretize a continuous structure into smaller, manageable parts for computational analysis. These elements collectively form a mesh, which represents the geometry of the original structure. Each element is defined by a set of nodes (vertices), where physical quantities such as deflection, are computed.

Element Types

This section was derived from ANSYS, Inc. (2011)

In FEA, various types of elements exist, each with its own characteristics and applicability. Table A.1-1 provides a breakdown of these element types. It is important to note that this section only considers 2D and 3D elements, as used in this dissertation.

At the highest level, elements in FEA are categorized by dimensionality: 2D elements lie within an X-Y plane, while 3D extend into an X-Y-Z space. This extra dimension allows 3D elements to provide more information than 2D elements, particularly along the thickness direction. These categories further encompass specific types. 2D elements include triangular and quadrilateral shapes, while 3D elements encompass tetrahedral, hexahedral, forms. Note that additionally, 3D elements also include pyramidal and prismatic forms, however these are less commonly used. Elements are classified as linear or parabolic based on their nodal arrangement; linear elements have nodes only at vertices, whereas parabolic elements feature nodes at both vertices and midpoints.

Element Selection

This section was derived from ANSYS, Inc. (2011)

The selection of the optimal element type for a given solution is noted to be a multivariable problem, with the main functions being geometry, accuracy requirements, computational efficiency, and mesh quality.

Table A.1-1: Typical 2D and 3D elements, including both their linear and parabolic variants (enterfea, 2019)

Element			
Dimension	**Shape**	**# Nodes**	**Schematic**
2D	Triangular Elements	3 Nodes	
		6 Nodes	
	Quadrilateral Elements	4 Nodes	
		8 Nodes	
3D	Tetrahedral Elements	4 Nodes	
		10 Nodes	
	Hexahedral Elements	8 Nodes	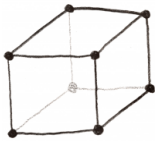
		20 Nodes	

	Linear Elements
	Parabolic Elements

As discussed in the section prior, at the highest level, elements are classified as either 2D or 3D. In structural analysis, the decision to use 2D or 3D elements depends on the aspect ratio of the structure. For thin structures, the stresses in the thickness direction are very small and can be assumed to be zero (this is referred to as a *plane stress* situation). This makes 2D elements ideal for meshing thin structures, as they sufficiently capture the require data without considering the thickness direction. Compared to their 3D equivalents, using 2D elements allows for fewer elements to be required, resulting in computational savings. On the other hand, for thick structures, solid elements are more suitable. The additional dimension allows these elements to provide data along the thickness direction, which is particularly important for analysing thick structures.

As discussed, elements can take various shapes. Depending on the complexity of a given structure, some elemental forms are more easily applicable than others. Triangular elements (for 2D) and tetrahedral elements (for 3D) are particularly well-suited for fitting complex geometries. This is because their geometries are simpler compared to their counterparts; quadrilateral elements for 2D, and hexahedral elements for 3D. Conversely for simpler geometries, quadrilateral and hexahedral elements are more applicable, require fewer elements and thus being less computationally intensive.

The choice between linear and quadratic elements is a function of several variables, one of which is the required accuracy. For applications demanding higher precision, parabolic elements are preferred. This preference is due to the additional nodes in parabolic elements, enabling higher-order interpolation functions that more accurately approximate variations in field variables, unlike linear elements restricted to linear interpolation. This enables for faster convergence rates to be achieved when using parabolic elements, being that, for a fewer number of elements, finer details can be acquired. This reduces computational cost, while maintaining accuracy.

Preliminary Study

In the preliminary study, the methodology applied by Manjusha et al. (2020) was adopted.

Main Study

In determining whether 2D or 3D elements were to be selected, focus was shifted on the bodies making up the GFRP sandwich panel. In this regard, these were noted to be ten; two facesheets, two cores; and 6 stiffeners

Being that the selection was primarily a function of aspect ratio, focus was shifted on the aspect ratio pertaining to the facesheets, the cores, and the stiffeners. In the case of the facesheets, high length-to-thickness $\left(\frac{3000\ mm}{4\ mm} = 750\right)$, and breadth-to-thickness $\left(\frac{1000\ mm}{4\ mm} = 250\right)$ ratios were noted to be present. For this reason, it was noted that plane stress conditions were present within the facesheets. Therefore, assuming that the stresses along the thickness direction were negligible, 2D elements

were noted to provide a quality mesh, as well as computational efficiency in deriving the desired results.

As for the core bodies, their respective length-to-thickness, and breadth-to-thickness ratio was noted to be 30 $\left(= \frac{3000\ mm}{100\ mm}\right)$ and 10 $\left(= \frac{1000\ mm}{100\ mm}\right)$, respectively. In comparison to the ratios calculated prior, it was clear that the degree of thickness exhibited by the cores was much larger. Additionally, it was also of importance to monitor the behaviour of the cores along the thickness direction. For these reasons, it was noted that adopting 2D elements in this regard would have not sufficed. For this reason, 3D elements were opted instead.

In regard to the stiffening system, in a similar fashion to that described in the case of the facesheets, plain stress conditions were noted to be present for the different bodies making up the stiffening system. As such it was noted that 2D elements would provide a quality mesh, as well as computational efficiency in deriving the concerning results.

In determining between the type of 2D and 3D elements to adopt in modelling the facesheets, the core, and the stiffening system, attention was given to the complexity of the GFRP sandwich panel. In this regard, in the case of all the components, no holes, internal voids, tapers, or irregular surfaces were noted. This rendered the GFRP panel simple in form. Owing to such simplicity, accuracy, as well as computational efficiency was noted to be achieved via the implementation of quadrilateral elements for the facesheets, and hexahedral elements for the cores.

The selection between opting for linear or parabolic 2D and/or 3D elements was based on the degree of accuracy desired in the numerical solution. In this manner, analytical analysis conducted prior highlighted a very fine variation in results owing to changing the angle of the stiffening system. For this reason, it was therefore decided to opt for the parabolic variant of the selected elements.

Specifically, the elements chosen were *shell281*, and *solid186*. The specific elements chosen were both noted to satisfy the previously described elemental criteria set up. However, *shell281* was specifically selected owing to its property in accounting for nonlinear analysis, as was element *solid186.* As an element, *shell281* is an 8 nodal element, with 6 degrees of freedom at each node: translations in the x-, y-, and z-axis, and rotations about the x-, y-, and z-axis, and rotations about the x-, y-, and z-axis. This element was chosen over *shell181* (the 2D element chosen in Manjusha's study [2020]) being that *shell281* is the parabolic variant of *shel181*. As described, this was therefore selected with the intention of achieving higher degrees of accuracy to those required in Manjusha et al.'s (2020) study.

As for *solid186*, this was noted to be a 20 nodal element, with 3 degrees of freedom per node: translations in the x-, y-, and z-axis.

Shell281 element and s*olid186* are depicted in Figure A.1-1A, and B, respectively.

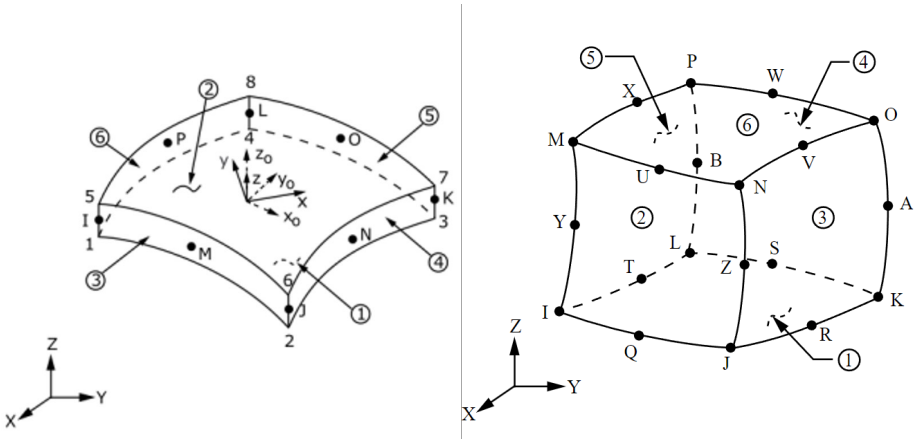

Figure A.1-1: (A) Shell281, and (B) solid183 (ANSYS, Inc., 2011).

Methods of Meshing

This section was derived from ANSYS, Inc. (2011)

Having identified the appropriate meshing elements for the panel, the next step was to determine the method for applying these mesh elements to the panel. This section describes different meshing methods and the rationale behind the selected method. The most commonly applied meshing methods include:

- Sweep Method
- Multi-Zone Method
- Patch Conforming Method
- Patch Independent Method

In the sweep method, mesh elements are applied to the body by sweeping them along a specified path or surface. This allows for the generation of high-quality meshes for bodies with geometry elongated in a specific direction.

In cases whereby the geometry does not follow an extruded form, the multi-zone method may be used. This method segments the geometry into individual components that follow an extruded form. In this way, the advantages pertaining to the sweep method are also found to be applicable to the multi-zone method.

In the patch conforming method, discrete portions (patches) of the surface are meshed independently. Elements are generated from the surface of the structure and move inwards. At some point, these patches intersect, at which point, a smooth transition is ensured by merging the independent meshes into a conformal volume mesh. This technique is suitable for complex geometries where the sweep method is not applicable, and splitting the structure in adopting the multi-zone method does not yield in the simplification of the structure.

Alternatively, for very high geometric complexities, the patch independent method may be the best meshing option. Similar to the patch conforming method, discrete portions of the surface are mesh independently, but without concern for neighbouring patches. As a result, conformality is not enforced across the boundaries of different mesh patches, leading to gaps and/or misalignment between mesh elements. This lack of conformity can result in inaccuracies in the simulation, especially in areas where interaction between different regions is critical.

Main Study

Among all the techniques discussed, the sweep method was identified as the most applicable. This conclusion was based on the fact that the geometry resembled a rectangular prism, a shape that is well-suited for extrusion.

In this regard, the sweeping method was to be applied in meshing the facesheets and the stiffening system via *shell281* elements. Additionally, the same method of meshing was to also be applied to *solid183* elements in meshing the cores.

Element Quality Metric

This section was derived from ANSYS, Inc. (2023)

In determining the quality of the mesh, reference was made to the element quality metric. The element quality metric is a composite quality metric. It follows the basic concept that, it is a desirable trait for an element to coincide with its ideal form; an equilateral triangle for triangular elements; a square for quadrilateral elements; a regular tetrahedron for tetrahedral elements, and; a cube for hexahedral elements. This is because, elements that match their ideal form provide numerical stability and accuracy in the results derived from the numerical model. Conversely, elements that deviate from their ideal form can lead to instability and inaccurate results.

The element quality metric ranges from 0 to 1, with 1 representative of elements in their ideal form, and 0 representative of elements of negative area/volume.

For two-dimensional elements, this is expressed as follows:

$$Quality = C\left(\frac{area}{\sum(EdgeLength)^2}\right)$$

Whilst for three-dimensional elements, this is expressed as:

$$Quality = C\left[\frac{volume}{\sqrt{[\sum(EdgeLength)^2]^3}}\right]$$

Where *area* and *volume* refer to the surface area and the volume of a 2D and 3D element, respectively, and *EdgeLength* refers to the total length of the edges of a given element. Additionally, the parameter *C* is noted to be a constant, whose value is based on element type. These constants are denoted in Table A.1-2.

Table A.1-2: Value of constant C for different element types (ANSYS, Inc., 2023).

Element		**Value of C**
Dimension	**Geometry**	
2D	Triangle	6.92820323
	Quadrilateral	4.0
3D	Tetrahedron	124.70765802
	Hexahedron	41.56921938

Extended Bibliography

ANSYS, Inc. (2011). Element Library. In I. ANSYS, *ANSYS Mechanical APDL Element Reference* (pp. 103-1410). Canonsburg: ANSYS, Inc.

ANSYS, Inc. (2023). Quality Group. In I. ANSYS, *ANSYS Meshing User's Guide* (pp. 115-153). Canonsburg: ANSYS, Inc.

enterfea. (2019, February 28). *What are the Types of Elements Used in FEA?* Retrieved from enterfea: https://enterfea.com/what-are-the-types-of-elements-used-in-fea/

Manjusha, M., & Althaf, M. (2020). Numerical Analysis on Flextural Behaviour of GFRP Sandwich Roof Panel with Multilayer Core Material. *5th International Conference on Modeling & Simulation in Civil Engineering*, *490*, pp. 1-15. Kerala.

Appendix A.2.

Figure A.2-1 depicts the vertical deflection contour corresponding to an ultimate mesh size of 48 mm, a mesh quality of 0.97, and a convergence rate of (+) 0.0089%. The maximum vertical deflection at the longitudinal midplane was labelled.

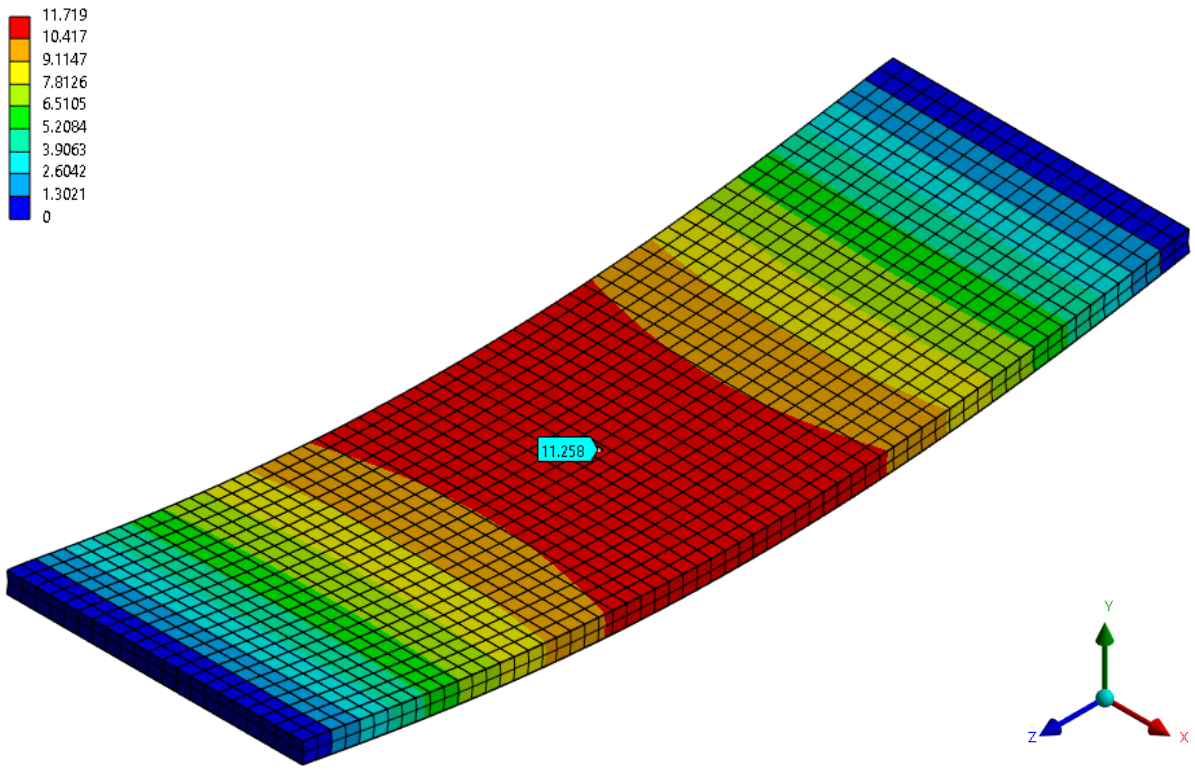

Figure A.2-1: Ultimate vertical deflection contour corresponding to a mesh size of 48 mm. Units are in mm.

Appendix A.3.

In determining the price per unit mass of the selected GFRP material, the degree of contribution provided by the constituents making up the GFRP material; that is, the degree of reinforcement, and matrix present within the GFRP material needed to be identified.

In determining the percentage contributions of the matrix and the reinforcement, the fibre volume ratio was utilised. This is a tool which allows one to measure the degree of fibre volume present within the FRP material as a fraction of the entire FRP volume. This is expressed as follows:

$$V_f = \frac{v_f}{v_{FRP}} \qquad \text{Eq. A.3.1}$$

Where:

V_f is the fibre volume ratio;

v_f is the volume of fibres;

v_{FRP} is the volume of the FRP.

The volume of the FRP may be expressed in terms of the fibre and matrix volume (v_m) as follows:

$$v_{FRP} = v_f + v_m \qquad \text{Eq. A.3.2}$$

Assuming a value of unity with the volume of the FRP (v_{FRP} = 1.0), congruency was noted to be present between the pairs V_f and v_f, and V_m and v_m. This was reflected in Eq. A.3.1. as follows:

$$1 = V_f + V_m \qquad \text{Eq. A.3.3}$$

As described in *Section 2.1*, this is an important tool because the mechanical properties of any composite material are a function of the fibre volume ratio. Table A.3-1 provides typical material properties, and their relation to the fibre volume ratio. All of these equations were obtained from Kopeliovich (2023).

Table A.3-1: Typical material properties expressed as a function of the fibre volume ratio (Kopeliovich, 2023).

Material Property	**Equation**	**Designation**
Longitudinal Modulus of Elasticity (E_{11})	$E_{11} = (1 - V_f)E_m + V_f E_f$	Eq. A.3.4
Transverse Modulus of Elasticity (E_{22})	$\frac{1}{E_{22}} = \frac{V_m}{E_m} + \frac{V_f}{E_f}$	Eq. A.3.5
Shear Modulus (G_{23})	$G_{23} = \frac{G_f G_m}{V_f G_m + V_m G_f}$	Eq. A.3.6
Poisson's Ratio (μ_{12})	$\mu_{12} = V_f \mu_f + V_m \mu_m$	Eq. A.3.7

Where:

E_m is the matrix modulus of elasticity

E_f is the fibre modulus of elasticity

G_m is the matrix shear modulus of elasticity

G_f is the fibre shear modulus of elasticity

μ_m is the matrix Poisson's ratio

μ_f is the fibre Poisson's ratio

From the equations provided in Table A.3-1, all of the material properties were noted to be a function of both V_f and V_m. The only exception was noted on the case of Eq. A.3.4. This was noted to be a function of V_f. On the basis that all concerning material properties were defined (refer to Table A.3-2), it was identified that rearranging Eq. A.3.4. in terms of V_f would allow for V_f to be calculated. The following exhibits the rearranged equation in terms of V_f and the subsequent calculation pertaining to V_f.

$$V_f = \frac{E - E_m}{E_f - E_m}$$

$$V_f = \frac{45 - 4}{70 - 4}$$

$$V_f = 0.622$$

The matrix volume ratio, V_m, was calculated via Eq. A.3.3. to be 0.378.

Table A.3-2: Material properties of the selected constituents (matrix and fibre), as well as the properties of the FRP being emulated. The far-right column indicates the source from which the material properties were extracted from.

Material	Constituent	Young's Modulus [GPa]	Shear Modulus [GPa]	Poisson's Ratio	Cost [kg/€]	Source
Matrix	Epoxy	4.00	1.54	0.3	15.43	(EasyComposites)
Fibre	E-Glass Woven Fabric	70.00	27.00	0.3	3.40	(Garrido, Madeira, Proenca, & Correia, 2019)
FRP	Epoxy E-Glass Woven Fabric	E_{11} = 45.00 E_{22} = 10.00	3.846	0.3	NA	(Manjusha & Althaf, 2020)

In verifying that the proper fibre and matrix constituents were selected, the remainder of the material properties were calculated. Proper selection of the fibre and matrix constituents was noted to have been achieved if a discrepancy of less than 0.5% was noted between the estimated material properties, and the actual material properties of the FRP. Table A.3-3 summarizes the estimated, and actual material properties for the FRP being emulated.

Table A.3-3: Comparison between the properties of the selected FRP (actual), and the emulated FRP (estimated).

	Epoxy E-Glass Woven Fabric		**Percentage Diff.**
	Actual	**Estimated**	
Transverse Modulus of Elasticity (E_{22}) [GPa]	10.00	9.99	0.1%
Shear Modulus, (G_{23}) [GPa]	3.842	3.846	0.1%
Poisson's Ratio, (μ_{12})	0.3	0.3	0.0%

As shown in Table A.3-3, the percentage difference between the mechanical properties of the emulated FRP material and the actual FRP material was within 0.5% for all properties considered. This indicated that the selected fibre and matrix constituents accurately represented the properties of the FRP material being emulated.

With the proper selection of constituents confirmed, the cost of the epoxy e-glass woven fabric was calculated by summing the products of the volume ratios and unit costs for each constituents.

$$c_{FRP} = V_f c_f + V_m c_m$$

$$c_{FRP} = (0.622 * 3.40) + (0.378 * 15.43)$$

$$c_{FRP} = 7.95\ €/kg$$

Therefore, the cost per unit mass of the epoxy e-glass woven fabric was calculated to be €7.95.

Extended Bibliography

EasyComposites. (n.d.). Epoxy Laminating Resin EL2. Stroke onTrent, Staffordshire, England.

Garrido, M., Madeira, J., Proenca, M., & Correia, J. (2019). Multi-Objective Optimization of Pultruded Composite Sandwich Panels for Building Floor Rehabilitation. *Construction & Building Materials*, 465-478.

Kopeliovich, D. (2023, December 13). Estimations of Composite Materials Properties.

Manjusha, M., & Althaf, M. (2020). Numerical Analysis on Flextural Behaviour of GFRP Sandwich Roof Panel with Multilayer Core Material. *5th International Conference on Modeling & Simulation in Civil Engineering*, *490*, pp. 1-15. Kerala.

Appendix A.4.

Note that entirety of this section was derived from ANSYS, Inc. (2023)

This appendix delves into the concept of *contact stiffness*. In describing this, it is best to first illustrate its importance.

Consider a system of two rigid bodies that have been perfectly bonded together at the mating surfaces. This enables such bodies to act as one single entity. Because of this, no relative movement is allowed to occur between the bodies. In this manner, because the bodies have been perfectly bonded, the stiffness at contact is noted to be infinitely stiff.

In FEA however, this simplification results in numerical instability. For this reason, a finite stiffness value is assigned to the nodes present at the contact area. Now, difficulty is identified in identifying the magnitude of stiffness assigned to such nodes. On one hand, assigning too large of a value may result in numerical instability. On the other hand, assigning too small of a value may result in one body penetrating into the other. In light of this, various techniques have been developed in assigning a finite value of stiffness to the concerning nodes, striking a balance between numerical stability, and minimization in penetration.

In this regard, consider the *Pure Penalty Contact Formulation*. This formulation adopts a penalty-based approach, with the aim of enforcing the applied contact constraints. This normal force is calculated using the following formula:

$$F_n = k_N x_p$$

Where F_n is the normal force; k_N is the contact stiffness, and; x_p is the penetration. These terms are diagrammatically illustrated in Figure A.4-1. The determination of the contact stiffness, k_N, is an iterative process, based on the described equation.

In determining k_N, first an initial guess for the contact stiffness is made. On the basis of simulating a perfect bond, and thus approximate infinite stiffness, this is typically chosen to be very large. Doing so allows for the concerning bodies not to significantly interpenetrate.

Next, the initial penetration is determined. This is achieved via the difference in coordinate points associated with the nodes present at the mating surfaces.

With k_N and x_p determined, the magnitude of the penalty force is calculated, F_n and applied to the same nodes at the mating surface. The updated position of such nodes is noted, and the new penetration, x_p, is calculated.

The updated penetration magnitude is compared against a convergence criterion. If the relative change in penetration is noted to be below a specified tolerance, then the contact stiffness, k_N, is noted to have been identified.

Otherwise, either the initial value of k_N is adjusted, and the process is repeated using the initial penetration value, or the same value of k_N initially selected is maintained, and node positions are updated until convergence in penetration is achieved. The latter approach is typically adopted more frequently.

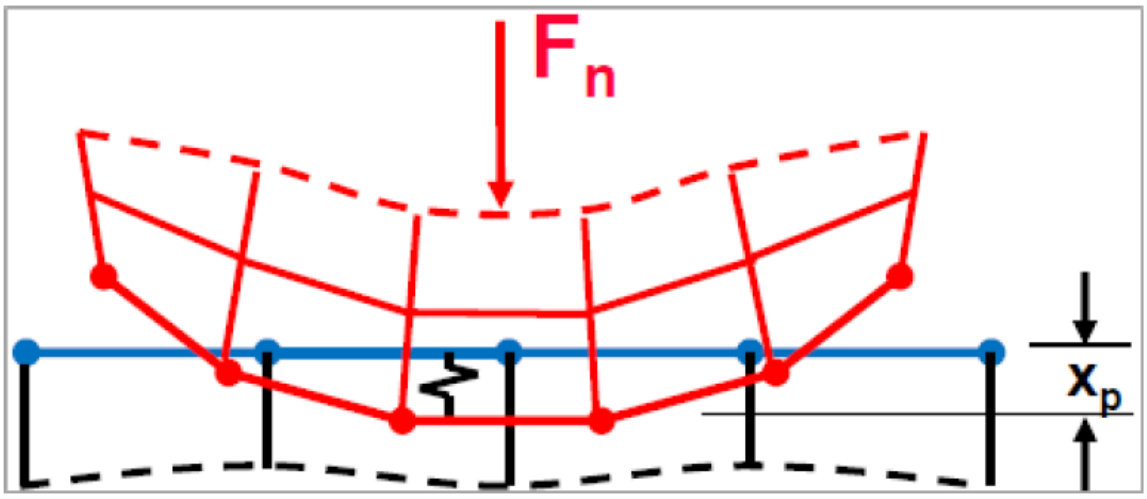

Figure A.4-1: In the context of two independent surfaces that have been perfectly bonded, the normal force, F_n (a function of k_N) and the penetration, x_p, are illustrated (ANSYS, Inc., 2023).

Extended Bibliography

ANSYS, Inc. (2023). Contact. In I. ANSYS, *Mechanical User's Guide* (pp. 1262-1329). Canonsburg: ANSYS, Inc.

Appendix A.5.

Note that entirety of this section was conducted on the basis of ANSYS, Inc. (2021)

This appendix provides a basic understanding of the theory behind geometric nonlinearity in finite element analysis. Geometric nonlinearity occurs when structures undergo significant deformations or displacements, rendering small deformation theories insufficient.

There are four main types of geometric nonlinearities: a) large strain, b) large rotation, c) stress stiffening, and d) spin softening. This appendix will solely focus on large strain geometric nonlinearity, as it was the primary concern of this dissertation.

To illustrate the effects of large strain geometric nonlinearity, consider a slender cantilever, of length L_0, subjected to a point load, P, at its free end. Refer to Figure A.5-1A. When the load is applied, a bending moment is generated, causing the cantilever to deflect. Due to the slenderness of the cantilever, it is not very stiff and thus deflects significantly. This deflection changes the perpendicular distance from the applied load to the support, reducing the magnitude of the applied moment. The new perpendicular distance is denoted as L_1, and depicted in Figure A.5-1B.

The aim of this example was to illustrate that when a structure undergoes significant shape changes, the magnitude of the resulting shear force and/or bending moment also changes for the same magnitude of applied load.

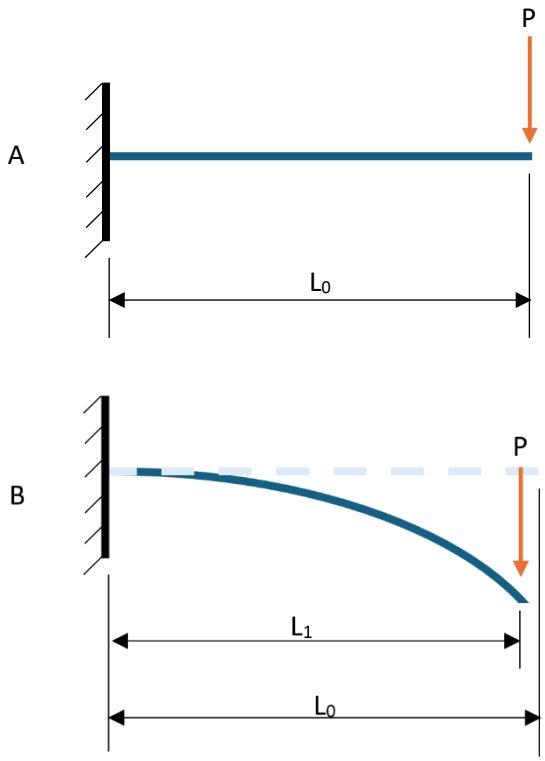

Figure A.5-1: Schematic of a cantilever beam in: (A) undeflected position, and (B) deflected position.

Theory of Geometric Nonlinearity

To describe the theory behind geometric nonlinearity, consider a point on an arbitrarily shaped body. Assume the position vector of this point in space is ***X***. When a load is applied to the body, it may translate, deform, or both. Let the new position of the point be defined by the position vector ***x***. The displacement of the point, ***u***, from its initial position to its new position is determined as follows:

$$\boldsymbol{u} = \boldsymbol{x} - \boldsymbol{X}$$

This is illustrated diagrammatically in Figure A.5-2.

Next, let the partial derivative of the vector in the new configuration, with respect to the original configuration be defined by the deformation gradient, *F*, as follows:

$$F = \frac{\partial x}{\partial X}$$

If the body solely translates, the vector ***x*** becomes a linear function of the vector ***X***, shown as:

$$\boldsymbol{x} = \boldsymbol{u} + \boldsymbol{X}$$

In this case, the deformation gradient equals the identity tensor ***I***. However, if the body deforms, the deformation gradient is no longer equal to the identity tensor, because ***x*** is no longer a linear function of ***X***. This implies that the deformation gradient is fundamental in determining whether the body has been stretched or compressed (i.e., strained).

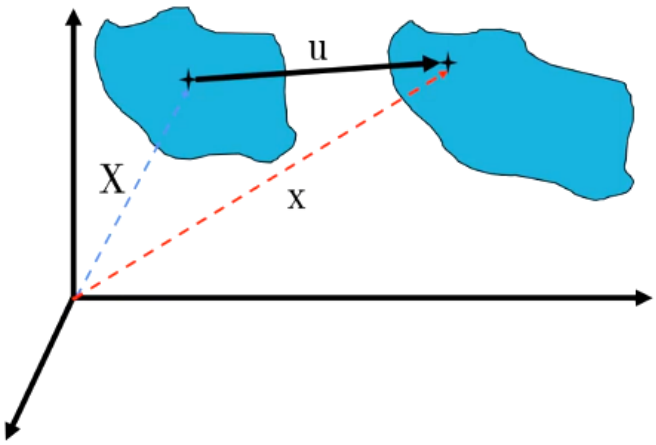

*Figure A.5-2: Arbitrarily shaped body has initial position vector denoted by **X**, and the new position vector denoted by **x**. Change in the position is denoted by **u** (ANSYS, Inc., 2021).*

In finite element analysis, various techniques have been devised to quantify strain. For the purposes of this appendix, focus is given to the Lagrange strain. The Lagrange strain (ε) quantifies the change in length of a unit material through the following relationship:

$$\varepsilon = \frac{1}{2}(F^T F - I)$$

Expressing the deformation gradient, *F*, in terms of **u**, and substituting into the equation for ε yields the following definitions for the individual Lagrange strain components:

		1st Term		**2nd Term**
ε_{xx}	$=$	$\frac{\partial u_x}{\partial X}$	$+$	$\frac{1}{2}\left[\left(\frac{\partial u_x}{\partial X}\right)^2+\left(\frac{\partial u_y}{\partial X}\right)^2+\left(\frac{\partial u_z}{\partial X}\right)^2\right]$
ε_{yy}	$=$	$\frac{\partial u_y}{\partial Y}$	$+$	$\frac{1}{2}\left[\left(\frac{\partial u_x}{\partial X}\right)^2+\left(\frac{\partial u_y}{\partial X}\right)^2+\left(\frac{\partial u_z}{\partial X}\right)^2\right]$
ε_{zz}	$=$	$\frac{\partial u_z}{\partial Z}$	$+$	$\frac{1}{2}\left[\left(\frac{\partial u_x}{\partial X}\right)^2+\left(\frac{\partial u_y}{\partial X}\right)^2+\left(\frac{\partial u_z}{\partial X}\right)^2\right]$
ε_{xy}	$=$	$\frac{1}{2}\left(\frac{\partial u_x}{\partial X}+\frac{\partial u_y}{\partial X}\right)$	$+$	$\frac{1}{2}\left[\frac{\partial u_x}{\partial X}\frac{\partial u_x}{\partial Y}+\frac{\partial u_y}{\partial X}\frac{\partial u_y}{\partial Y}+\frac{\partial u_z}{\partial X}\frac{\partial u_z}{\partial Y}\right]$
ε_{xz}	$=$	$\frac{1}{2}\left(\frac{\partial u_x}{\partial Z}+\frac{\partial u_z}{\partial X}\right)$	$+$	$\frac{1}{2}\left[\frac{\partial u_x}{\partial X}\frac{\partial u_x}{\partial Z}+\frac{\partial u_y}{\partial X}\frac{\partial u_y}{\partial Z}+\frac{\partial u_z}{\partial X}\frac{\partial u_z}{\partial Z}\right]$
ε_{yz}	$=$	$\frac{1}{2}\left(\frac{\partial u_y}{\partial Z}+\frac{\partial u_z}{\partial Y}\right)$	$+$	$\frac{1}{2}\left[\frac{\partial u_x}{\partial Y}\frac{\partial u_x}{\partial Z}+\frac{\partial u_y}{\partial Y}\frac{\partial u_y}{\partial Z}+\frac{\partial u_z}{\partial Y}\frac{\partial u_z}{\partial Z}\right]$

As shown, each strain components consists of two parts; a linear component and a quadratic component. When deformations are very small, the derivatives of the displacements will also be very small, and their squares will be even smaller, making them negligible. Thus, for small deformations, the quadratic term can be ignored. This simplifies the Lagrange strain components to a function of only the linear terms. These are expressed hereunder:

$$\varepsilon_{xx}=\frac{\partial u_x}{\partial X}$$

$$\varepsilon_{yy}=\frac{\partial u_y}{\partial Y}$$

$$\varepsilon_{zz}=\frac{\partial u_z}{\partial Z}$$

$$\varepsilon_{xy}=\frac{1}{2}\left(\frac{\partial u_x}{\partial X}+\frac{\partial u_y}{\partial X}\right)$$

$$\varepsilon_{xz}=\frac{1}{2}\left(\frac{\partial u_x}{\partial Z}+\frac{\partial u_z}{\partial X}\right)$$

$$\varepsilon_{yz}=\frac{1}{2}\left(\frac{\partial u_y}{\partial Z}+\frac{\partial u_z}{\partial Y}\right)$$

As deformation increase however, the contribution of the quadratic term to the strain of a given component becomes more significant. Ignoring this term can lead to errors whose magnitude increases quadratically.

Having established this, consider how this theory affects the governing equation for a body in static equilibrium, expressed as follows:

$$[K]\{u\} = F$$

Where; *K* is the stiffness of the system; *u* is the displacement of the system, and; *F* is the applied external force.

Since the stiffness of the structure depends on displacement in the case of large deformations, the governing equation must be modified to account for this. Therefore, in the case of large strain geometric nonlinearity, the governing equation becomes:

$$[K(u)]\{u\} = F$$

Extended Bibliography

ANSYS, Inc. (2021). Nonlinear Structural Analysis. In I. ANSYS, *Structural Analysis Guide* (pp. 217-316). Canonsburg: ANSYS, Inc.

Appendix A.6.

Note that entirety of this section was conducted on the basis of ANSYS, Inc. (2023)

This appendix served to describe the functionality of the *Response Surface* module and its components, namely the *Design of Experiments* (DOE) and *Response Surface* component.

The primary aim of the *Response Surface* module was to analyse the effects of input variables on output variables for a given system. Traditionally, this was achieved by changing each input variable individually and recording the outcomes. However, for large number of permutations, this method was noted to be both labour-intensive and time-consuming.

To address this, *Response Surface* functions were used. These are machine learning algorithms that predict the performance of a system on the basis of an initial data set. This data set is generated via a *Design of Experiment* function

In light of this, the first section of this appendix discusses two different DOE functions: the *Face-Centred Central Composite Design* (FCCCD), and the; *Box-Behnken Design* (BBD). The second section covers two *Response Surface* methods: the *2nd Order Polynomial Regression*, and the *Kriging* method.

Design of Experiment

Before discussing the different DOE functions considered, it is important to clarify the nomenclature used. All possible input variable combinations lie within a design space, which corresponds dimensionally to the number of input variables. For example, a system with three input variables has a three-dimensional design space, where each axis represents one input variable.

Within this space, the maximum and minimum values for each input variable are denoted by +1 and -1, respectively. Values between these extremes are assigned a value between +1 and -1 through linear interpolation.

For illustration purposes, consider the input variables in this dissertation: facesheet thickness, core thickness, and stiffener angle. The ranges for each are summarized in Table A.6-1.

Table A.6-1: The domain of the input variables considered in this dissertation, together with their associated step size are tabulated.

Parameter	**Symbol**	**Input Value**		**Step Size**
		Minimum (= -1)	**Maximum (= +1)**	
Facesheet Thickness (Top)	T_{Ft}	1.2 mm	4.0 mm	0.4 mm
Total Core Thickness	T_{Ct}	50 mm	100 mm	10 mm
Stiffener Angle #1	ϑ_1	50°	130°	10°

Since three input variables were considered, the design space was three dimensional. The range of each axis was from -1 to +1, with -1 denoted the minimum value and +1 denoted the maximum value of the input variable. For instance, for the facesheet thickness axis, -1 corresponded to a thickness of 1.2 mm and +1 corresponded to a thickness of 4.0 mm. The same principle applied to the other input variables.

The rest of this discussion considered DOE functions with respect to a three-dimensional design space

Face-Centred Central Composite Design

The *Face-Centred Central Composite Design* is an experimental design that uses 15 data points based on predefined input variables. Figure A.6-1 illustrates the locations of these data points within a three-dimensional design space.

For each input variable, the FCCCD considers all possible combinations at their maximum and minimum levels: (1, 1, 1), (1, 1, -1), (1, -1, 1), (1, -1, -1), (-1, 1, 1), (-1, 1, -1), (-1, -1, 1), and (-1, -1, -1), totalling 8 data points. Considering such data points allows for the selected machine learning algorithm to determinate the degree of linearity between the input variables, and the output variables. It additionally allows the generated sample-set to inhibit data pertaining to the relationship of the input variables between themselves. Finally, by including points at the extreme corners of the design space, it allows for a broad coverage of the design space to be achieved, thus minimizing any errors derived from the selected machine learning algorithm as a result of extrapolating the given data beyond its extremities.

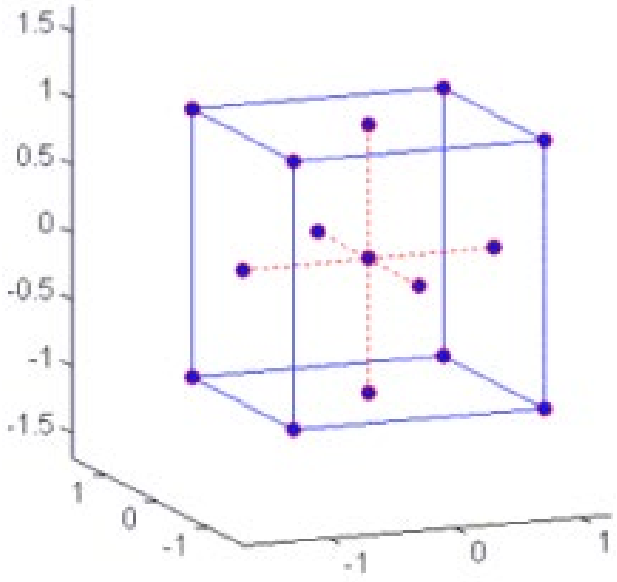

Figure A.6-1: Sample set pertaining to the Face-Centred Central Composite Design (ANSYS, Inc., 2023).

The FCCCD also includes face-centred data points where one input variables is at +1 or -1 while the other two are at their centre levels (0). These points are: (1, 0, 0), (0, 1, 0), (0, 0, 1), (-1, 0, 0), (0, -1, 0), (0, 0, -1), totalling 6 data points. Considering such data points allows for curvature, if any, in the response surface to be accounted for. Additionally, they also account in providing data at intermediate levels for each input variables, thus filling the gaps between the high and low levels explored by the previously discussed data points.

Finally, FCCCD also considers the centre point of the design space at (0, 0, 0). By considering such data point, a reference point is provided in validating the model, ensuring that the selected machine learning algorithm accurately predicted the response at the midpoint of the input variables.

The main advantages of the FCCCD are that it allows for the design space to be thoroughly explored, as evidenced by considering combinations at their extreme levels. Although this, with respect to the *Box-Behnken Design*, because more combinations are considered in the FCCCD, this experimental design is identified to be more computationally intensive, requiring more time to conduct.

Box-Behnken Design

The *Box-Behnken Design* is an experimental design that analyses 13 data points based on predefined input variables. Figure A.6-2 illustrates the locations of these data points within a three-dimensional design space.

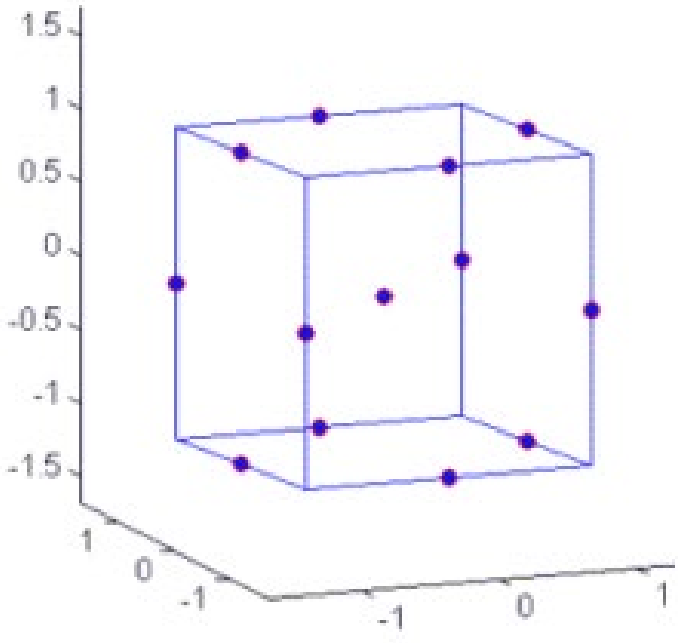

Figure A.6-2: Sample set pertaining to the Box-Behnken Design (ANSYS, Inc., 2023).

Unlike the FCCCD, which considers all possible design points at their maximum and minimum levels, the BBD conducts analysis at the midpoints of the edges of the experimental space. These points include: (1, 1, 0), (1, -1, 0), (-1, 1, 0), (-1, -1, 0), (1, 0, 1), (1, 0, -1), (-1, 0, 1), (-1, 0, -1), (0, 1, 1), (0, 1, -1), (0, -1, 1), and (0, -1, -1). This approach allows the BBD to estimate interaction terms in the response surface model more effectively, enhancing the estimation of relationships between different input variables.

Additionally, similar to the FCCD, the BBD includes a design point at the centre of the design space (0, 0, 0). This serves the same function as in the FCCCD, i.e., to serve as a reference point in validating the data set derived by the machine learning algorithm.

The main advantage of the BBD is its efficiency in estimating the design space while reducing the number of design points from 15 in the FCCCD to 13. This makes data generation through the BBD less computationally intensive and more time efficient.

However, because the BBD does not consider the maxima and minima of the input variables, the design space is not as thoroughly explored as in the FCCCD. This limitation places greater emphases on the selected machine learning algorithm's ability to extrapolate the provided data set.

Response Surface

The aim of the *Response Surface* component was to predict the entirety of the output response, on the basis of the provided data set generated by the *Design of Experiment* function. In this section, reference was first made to *2nd Order Polynomial Regression*, followed by the *Kriging* model.

2nd Order Polynomial Regression

In *2nd Order Polynomial Regression*, the relationship between the output variables takes the following form:

$$y = a_0 + a_1 x + a_2 x^2$$

Where a_i are the coefficients to be estimated.

However, owing to catering for the presence of three input variables, and three output variables, for each output variable (i = 1, 2, 3), the model above is modified to take the following form:

$$y_i = a_{0i} + a_{1i}x_1 + a_{2i}x_2 + a_{3i}x_3 + a_{4i}x_1^2 + a_{5i}x_2^2 + a_{6i}x_3^2 + a_{7i}x_1x_2 + a_{8i}x_1x_3 + a_{7i}x_2x_3$$

In this manner; x_1, x_2, and x_3 are linear terms; x_1x_2, x_1x_3, and x_2x_3 are interactions terms, and; x_1^2, x_2^2, and x_3^2 are quadratic terms. Calculating the coefficients yields the relationship between the input variables and the output variables. These are determined as follows:

$$a_i = (X^T X)^{-1} X^T Y_i$$

Where X is the design matrix containing all the polynomial terms; X^T is the transpose of the same design matrix, and Y_i is the vector of the i-th output variables values.

The advantage of adopting this technique is that, relative to the *Kriging* model (to be discussed in the following section), it is a relatively simple model, in that the coefficients of the polynomial provide clear insights into the relationship between the variables, thus making interpretation of the model relatively easier. Because it is a relatively simpler model, it is not as computationally expensive.

However, because this polynomial regression is restricted to the second order, it is limited to quadratic relationships. For this reason, applying this technique may not suffice in the case that the true relationship is more complex. Additionally, it is noted that the extrapolation of data beyond what has been provided in the data set may lead to unreliable predictions.

Kriging Model

The *Kriging* model is a geostatistical interpolation technique, typically used for spatial data analysis and prediction. It is based on the assumption that design points closer to the unknown design point are more likely to have similar values compared to those that are farther away.

Using this assumption, the *Kriging* model estimates the value at an unsampled location by computing a weighted average of the observed design points, where the weights are determined based on their distance to the unsampled design point. This is mathematically expressed as follows:

$$G(x_0, y_0, z_0) = \sum_{i=1}^{n} \lambda_i g(x_i, y_i, z_i)$$

Where $G(x_0, y_0, z_0)$ is the predicted value of the design point; $g(x_i, y_i, z_i)$ is the observed data at design point i, and λ_i represents the weight assigned to each design point. The weights λ_i are determined using the covariance matrix:

$$\begin{bmatrix} \sigma_{11} & \sigma_{12} & \sigma_{13} & \cdots & \sigma_{1m} \\ \sigma_{21} & \sigma_{22} & \sigma_{23} & \cdots & \sigma_{2m} \\ \sigma_{31} & \sigma_{32} & \sigma_{33} & \cdots & \sigma_{3m} \\ \vdots & \vdots & \vdots & \ddots & \vdots \\ \sigma_{n1} & \sigma_{n2} & \sigma_{n3} & \cdots & \sigma_{nm} \end{bmatrix} \begin{bmatrix} \lambda_1 \\ \lambda_2 \\ \lambda_3 \\ \vdots \\ \lambda_n \end{bmatrix} = \begin{bmatrix} \sigma_{10} \\ \sigma_{20} \\ \sigma_{30} \\ \vdots \\ \sigma_{n0} \end{bmatrix}$$

Where σ_{nm} is the covariance between design points n and m, and σ_{n0} is the covariance between design point i and the new design point 0.

Once the weights λ_i are computed, they are applied to the corresponding design points to calculate the weighted average, which allows for the prediction of the value at the new design point to be achieved.

Compared to the *2nd Order Polynomial Regression* model, the *Kriging* model can offer more accurate predictions due to its superior handling of irregular data. However, *Kriging* requires computation of a larger number of linear equations and spatial correlations, making it more computationally intensive. Additionally, *Kriging* is less interpretable than the *2nd Order Polynomial Regression* model because it relies on spatial correlations rather than explicit functional relationships. In both models however, extrapolating beyond the range of observed data can result in unreliable predictions and increased uncertainty in the results.

Selection of Design of Experiment & Response Surface Function

In determining the optimal DOE function and corresponding *Response Surface* function, focus was initially shifted on the latter owing to its dependency on the DOE function. It was observed that both the *2nd Order Polynomial Regression* model and the *Kriging* model, while useful, have limitations in accuracy when extrapolating beyond the range of observed data. Therefore, it was crucial to select a DOE function that thoroughly explored the extremes of the design space, thus mitigating errors.

Among the discussed DOE functions – *Face-Centred Central Composite Design* and *Box-Behnken Design* – only the FCCCD was found to provide comprehensive exploration of the design space. Hence, FCCCD was chosen as the optimal DOE function for this dissertation.

Regarding the *Response Surface* function, the *2nd Order Polynomial Regression* model was noted to be limited to quadratic relationships. This made the *Kriging* model a better choice for capturing more complex relationships with greater accuracy. On this basis, the *Kriging* model was selected as the optimal *Response Surface* function for the purposes of this dissertation.

In summary, the chosen DOE function was the *Face-Centred Central Composite Design* due to its thorough exploration of the design space, while in predicting the performance of the output variables with respect to the input variables for all panel configurations considered, the *Kriging* model was selected as the *Response Surface* function. This was selected for its ability to accurately model complex relationships.

Extended Bibliography

ANSYS, Inc. (2023). Using Design of Experiments. In I. ANSYS, *DesignXploter User's Guide* (pp. 81-98). Canonsburg: ANSYS, Inc.

Appendix A.7

Figures A.7-1 and A.7-2 provide a graphical representation of the goodness of fit of the *Kriging model* to the sample set generated via the *Face-Centred Central Composite Design*. This appendix includes only those pertaining to total sandwich panel mass, m_T, and total sandwich panel material cost, C_T. The plot concerning the maximum vertical deflection, Δ_T, was provided in *Section 3.2.4*. The shown plots present the predicted data vs the observed data.

Also provided were the; coefficient of determination; root mean square error; relative maximum absolute error, and; relative average absolute error, with the optimal scenarios depicted in brackets.

A good fit was identified in Figures A.7-1 and A.7-2, as evidenced by the quasi y = x relationship and supported by the statistical scores.

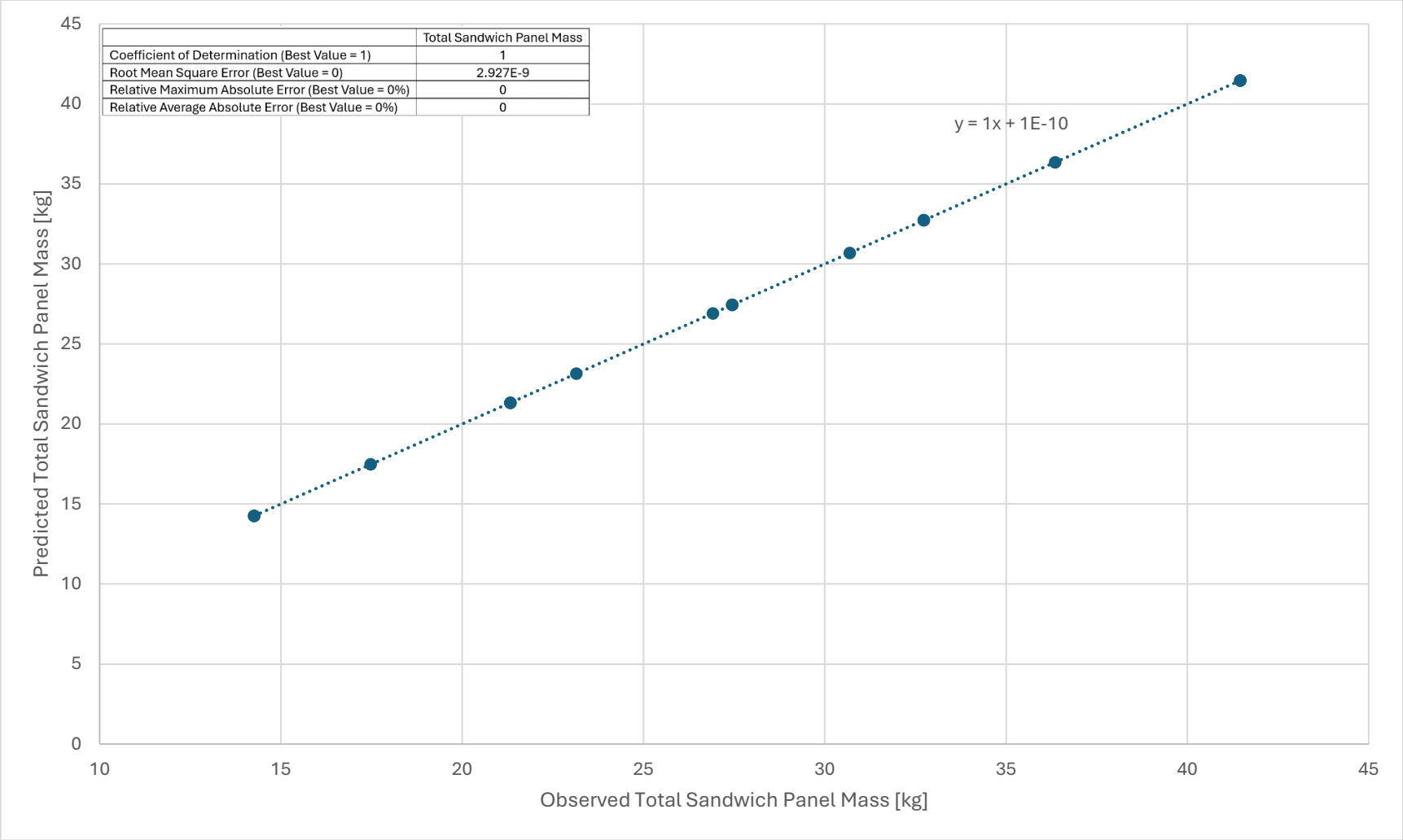

Figure A.7-1:Graph of predicted vs observed total sandwich panel mass [kg].

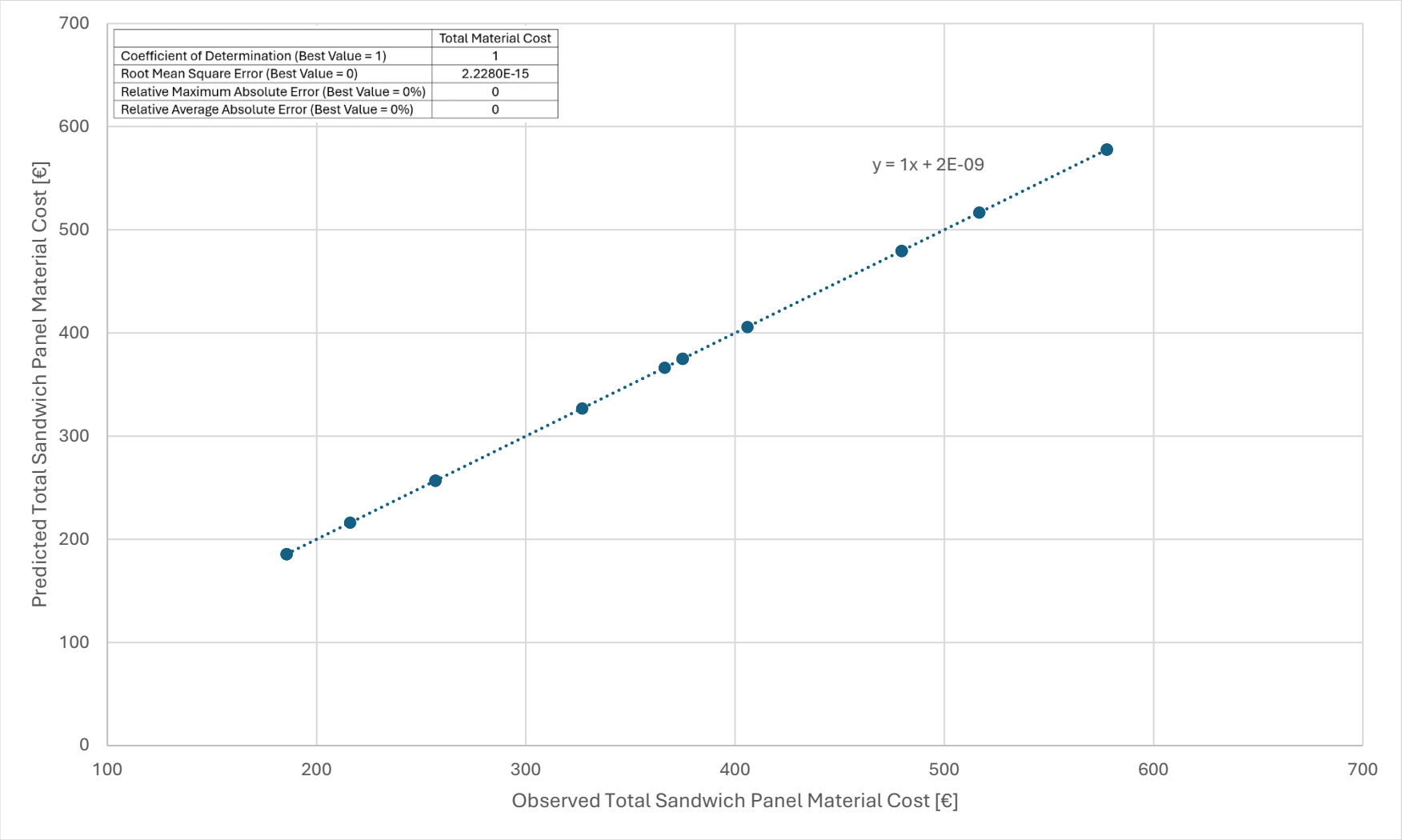

Figure A.7-2: Graph of predicted vs observed total sandwich panel material cost [€].

Appendix B.1

Designation	Angle	Thickness		Finite Element Analysis (FEA)							Analytical Analysis (AA)	FEA/AA Ratio
				Mesh				Maximum Vertical Deflection at Longitudinal Midplane				
				Penultimate		Ultimate		Penultimate [mm]	Ultimate [mm]	Convergence	Ultimate [mm]	
		Core [mm]	Facesheet [mm]	Size [mm]	Avg. Quality	Size [mm]	Avg. Quality					
A90C50F1.2	90	50	1.2	18	0.92	17	0.93	27.24	27.46	0.80%	28.62	95.95%
A90C60F1.2	90	60	1.2	18	0.96	17	0.96	19.37	19.31	- 0.31%	19.87	97.18%
A90C70F1.2	90	70	1.2	18	0.97	17	0.97	14.36	14.26	- 0.70%	14.57	97.87%
A90C80F1.2	90	80	1.2	18	0.87	17	0.87	10.80	10.81	0.09%	11.11	97.30%
A90C90F1.2	90	90	1.2	21	0.86	20	0.86	8.58	8.58	0.00%	8.74	98.17%
A90C100F1.2	90	100	1.2	23	0.85	21	0.86	7.11	6.99	- 1.72%	7.05	99.15%
A90C50F1.2	90	50	1.2	18	0.92	17	0.93	27.24	27.46	0.80%	28.62	95.95%
A90C50F1.6	90	50	1.6	18	0.92	17	0.93	20.68	20.86	0.86%	21.44	97.29%
A90C50F2.0	90	50	2.0	18	0.92	17	0.94	16.43	16.57	0.84%	16.84	98.40%
A90C50F2.4	90	50	2.4	18	0.92	17	0.94	13.59	13.71	0.88%	13.80	99.35%
A90C50F2.8	90	50	2.8	18	0.92	17	0.94	11.66	11.77	0.93%	11.73	100.34%
A90C50F3.2	90	50	3.2	18	0.92	17	0.94	10.11	10.21	0.98%	10.09	101.19%
A90C50F3.6	90	50	3.6	18	0.93	17	0.94	8.92	9.00	0.89%	8.82	102.04%
A90C50F4.0	90	50	4.0	18	0.93	17	0.94	8.00	8.08	0.99%	7.86	102.80%
A50C50F1.2	50	50	1.2	18	0.87	17	0.89	26.38	26.91	1.97%	28.32	95.02%
A60C50F1.2	60	50	1.2	18	0.89	17	0.91	27.07	27.26	0.70%	28.46	95.78%
A70C50F1.2	70	50	1.2	18	0.90	17	0.93	26.98	27.51	1.93%	28.55	96.36%

Designation	Angle	Thickness		Finite Element Analysis (FEA)							Analytical Analysis (AA)	FEA/AA Ratio
				Mesh				Maximum Vertical Deflection at Longitudinal Midplane				
				Penultimate		Ultimate		Penultimate [mm]	Ultimate [mm]	Convergence	Ultimate [mm]	
		Core [mm]	Facesheet [mm]	Size [mm]	Avg. Quality	Size [mm]	Avg. Quality					
A80C50F1.2	80	50	1.2	18	0.91	17	0.93	27.55	27.47	- 0.29%	28.60	96.05%
A90C50F1.2	90	50	1.2	18	0.92	17	0.93	27.68	27.46	- 0.80%	28.62	95.95%
A100C50F1.2	100	50	1.2	18	0.91	17	0.94	27.33	27.41	0.29%	28.60	95.84%
A110C50F1.2	110	50	1.2	18	0.90	17	0.93	27.14	27.37	0.84%	28.55	95.87%
A120C50F1.2	120	50	1.2	18	0.89	17	0.92	26.35	27.08	2.70%	28.46	95.15%
A130C50F1.2	130	50	1.2	18	0.87	17	0.89	26.08	26.63	2.07%	28.32	94.03%
A50C50F4.0	50	50	4.0	18	0.88	17	0.90	7.93	8.11	2.22%	7.80	103.97%
A60C50F4.0	60	50	4.0	18	0.90	17	0.92	8.03	8.08	0.62%	7.83	103.19%
A70C50F4.0	70	50	4.0	18	0.91	17	0.94	7.92	8.11	2.34%	7.84	103.44%
A80C50F4.0	80	50	4.0	18	0.92	17	0.94	8.08	8.07	- 0.12%	7.85	102.80%
A90C50F4.0	90	50	4.0	18	0.93	17	0.94	8.00	8.08	0.99%	7.86	102.80%
A100C50F4.0	100	50	4.0	18	0.92	17	0.94	8.03	8.07	0.50%	7.85	102.80%
A110C50F4.0	110	50	4.0	18	0.91	17	0.94	7.91	8.10	2.35%	7.84	103.32%
A120C50F4.0	120	50	4.0	18	0.90	17	0.92	7.91	8.08	2.10%	7.83	103.19%
A130C50F4.0	130	50	4.0	18	0.88	17	0.90	8.01	8.11	1.23%	7.80	103.97%
A50C100F1.2	50	100	1.2	23	0.85	21	0.86	6.87	6.99	1.72%	6.91	101.16%
A60C100F1.2	60	100	1.2	23	0.90	21	0.90	6.95	7.04	1.28%	6.97	101.00%
A70C100F1.2	70	100	1.2	23	0.93	21	0.93	7.10	7.07	- 0.42%	7.02	100.71%

Designation	Angle	Thickness		Finite Element Analysis (FEA)							Analytical Analysis (AA)	FEA/AA Ratio
				Mesh				Maximum Vertical Deflection at Longitudinal Midplane				
				Penultimate		Ultimate		Penultimate [mm]	Ultimate [mm]	Convergence	Ultimate [mm]	
		Core [mm]	Facesheet [mm]	Size [mm]	Avg. Quality	Size [mm]	Avg. Quality					
A80C100F1.2	80	100	1.2	23	0.94	21	0.95	7.23	7.08	-2.12%	7.04	100.57%
A90C100F1.2	90	100	1.2	23	0.95	21	0.95	7.07	7.08	0.14%	7.05	100.43%
A100C100F1.2	100	100	1.2	23	0.94	21	0.95	6.91	7.08	2.40%	7.04	100.57%
A110C100F1.2	110	100	1.2	23	0.93	21	0.93	6.97	7.06	1.27%	7.02	100.57%
A120C100F1.2	120	100	1.2	23	0.89	21	0.91	6.92	7.01	1.28%	6.97	100.57%
A130C100F1.2	130	100	1.2	23	0.85	21	0.86	6.85	6.97	1.72%	6.91	100.87%
A50C100F4.0	50	100	4.0	23	0.85	21	0.86	2.34	2.36	0.85%	2.04	115.69%
A60C100F4.0	60	100	4.0	23	0.90	21	0.91	2.38	2.37	- 0.42%	2.06	115.05%
A70C100F4.0	70	100	4.0	23	0.93	21	0.94	2.36	2.35	- 0.43%	2.07	113.53%
A80C100F4.0	80	100	4.0	23	0.94	21	0.95	2.36	2.34	- 0.85%	2.07	113.04%
A90C100F4.0	90	100	4.0	23	0.96	21	0.96	2.33	2.35	0.85%	2.07	113.53%
A100C100F4.0	100	100	4.0	23	0.95	21	0.95	2.36	2.34	- 0.85%	2.07	113.04%
A110C100F4.0	110	100	4.0	23	0.93	21	0.94	2.38	2.36	- 0.85%	2.07	114.01%
A120C100F4.0	120	100	4.0	23	0.90	21	0.91	2.38	2.37	- 0.42%	2.06	115.05%
A130C100F4.0	130	100	4.0	23	0.86	21	0.86	2.34	2.36	0.85%	2.04	115.69%

Appendix B.2.

This appendix serves to display all of the vertical deflection contours for trendlines *F1.2*, and *C50*. Figures B.2-2 through B.2-14 show only a quarter of the contour due to symmetry along the longitudinal and transverse axes.

Figure B.2-1 serves as a key for all figures in this appendix.

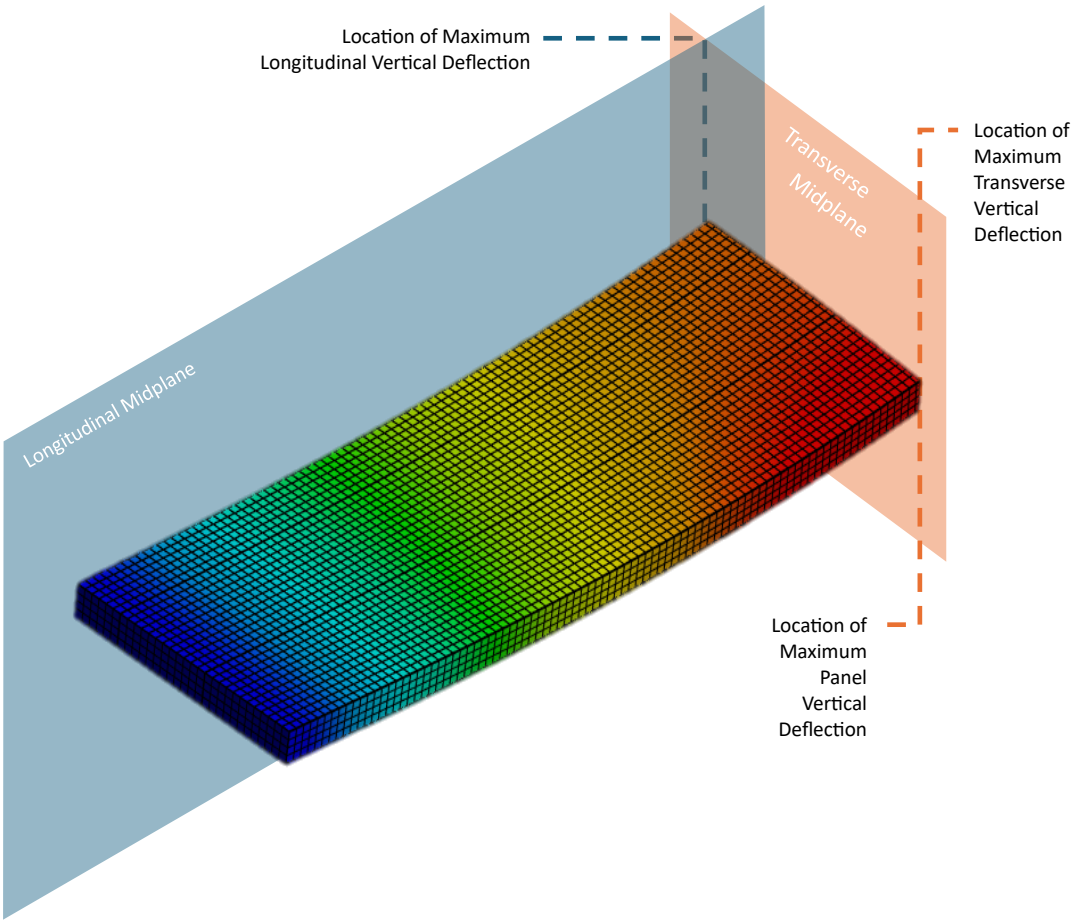

Figure B.2-1: Key applicable to vertical deflection contours.

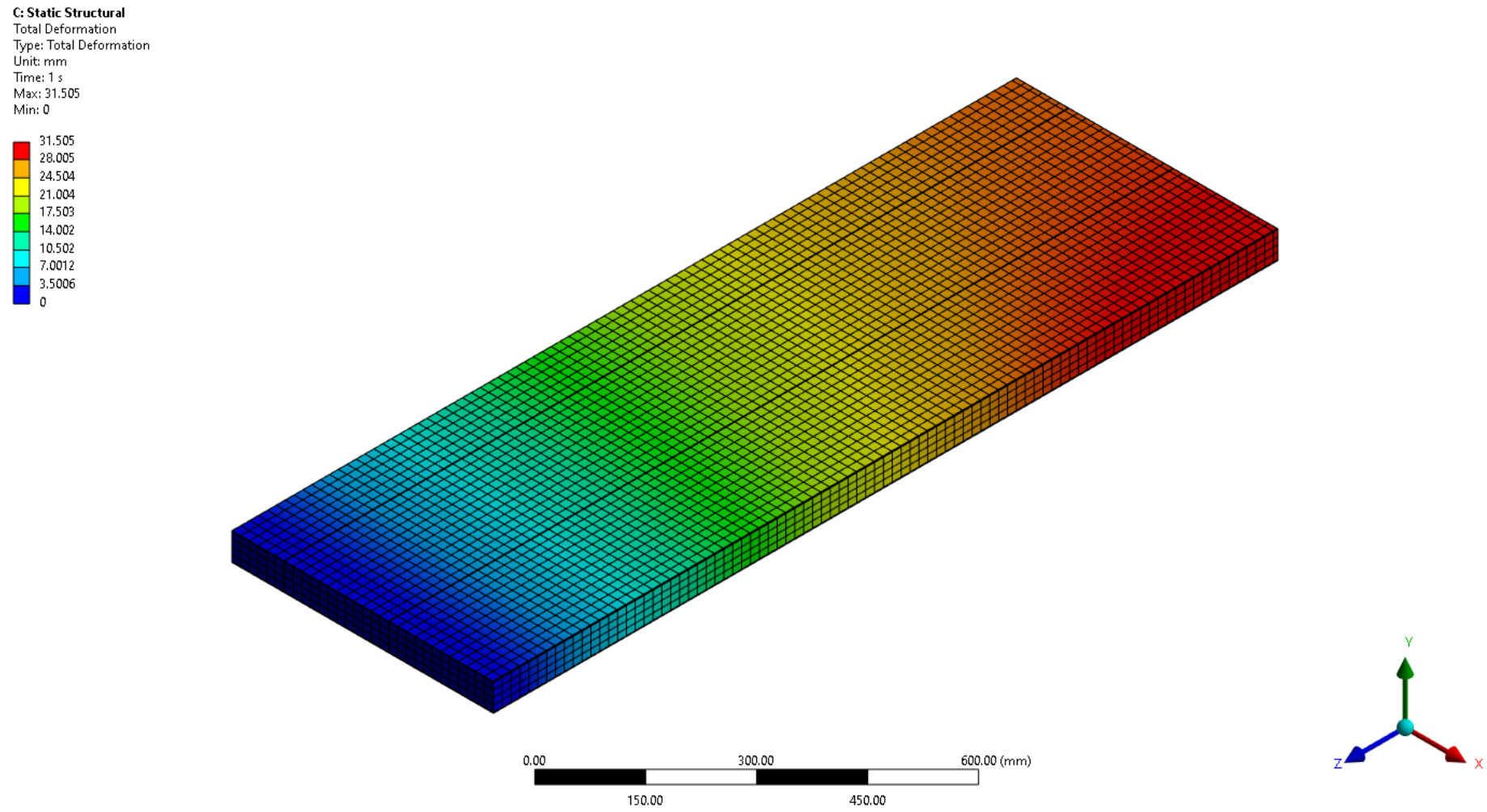

Figure B.2-2: Vertical deflection contour of configuration A90C50F1.2. Note that units are in mm.

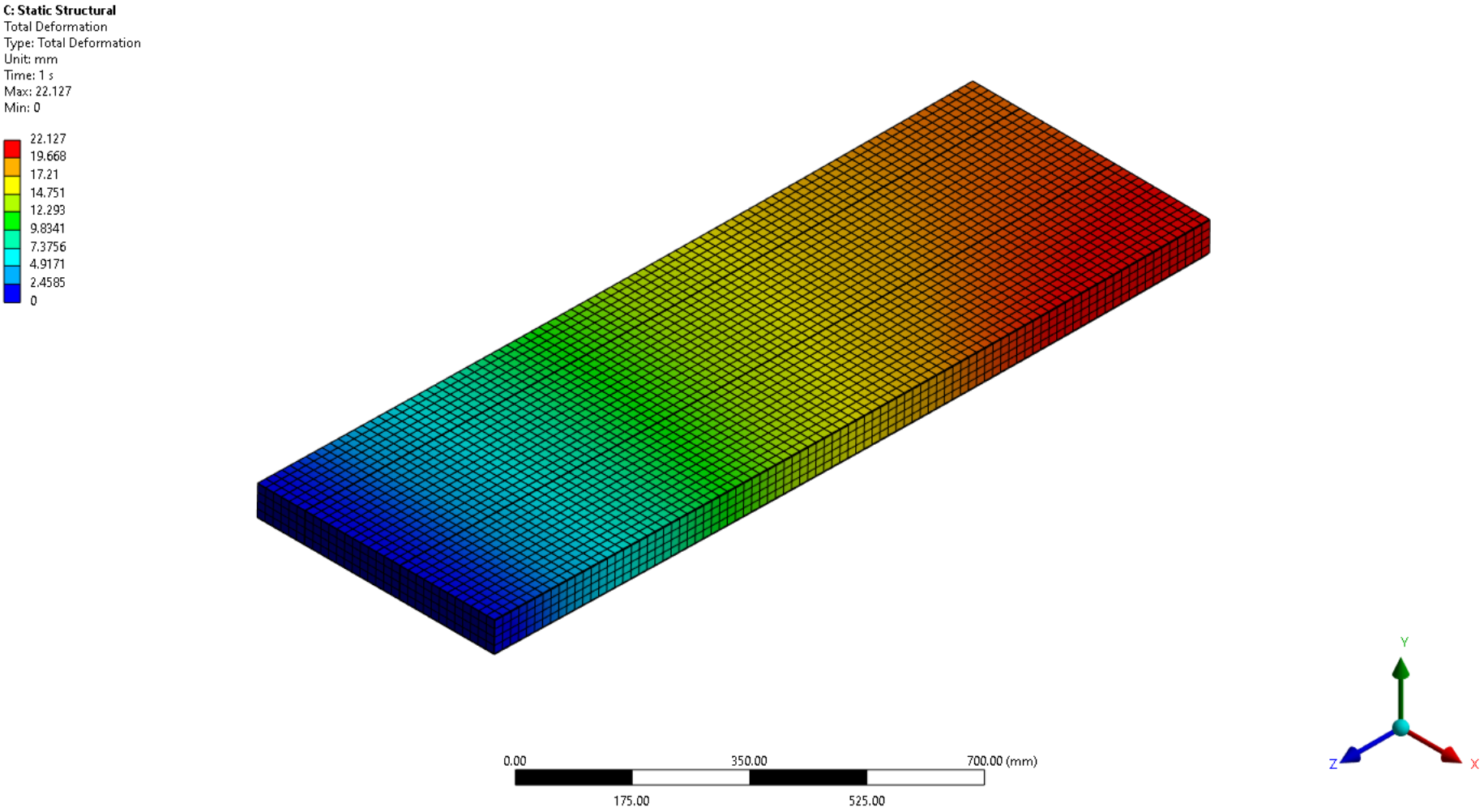

Figure B.2-3: Vertical deflection contour of configuration A90C60F1.2. Note that units are in mm.

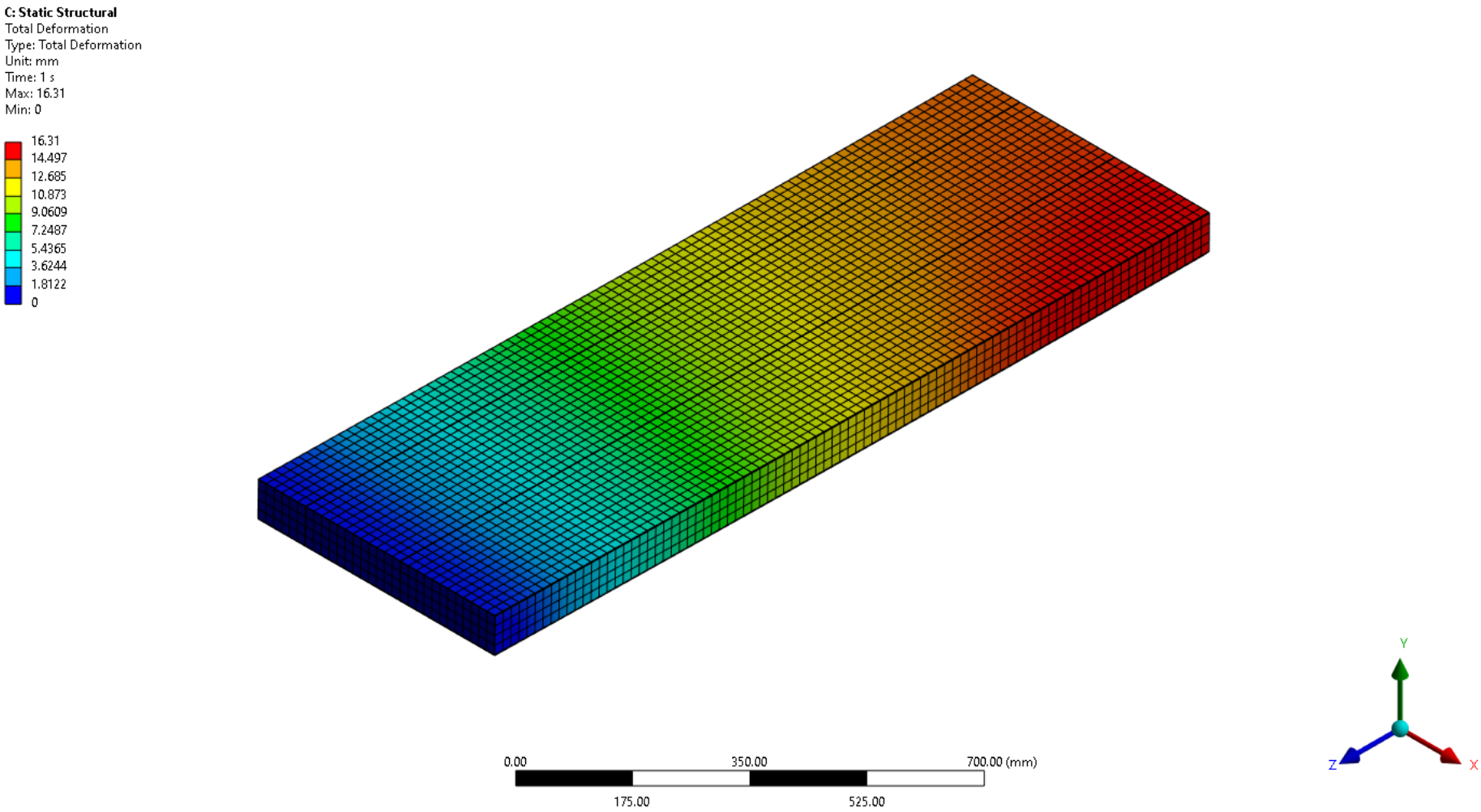

Figure B.2-4: Vertical deflection contour of configuration A90C70F1.2. Note that units are in mm.

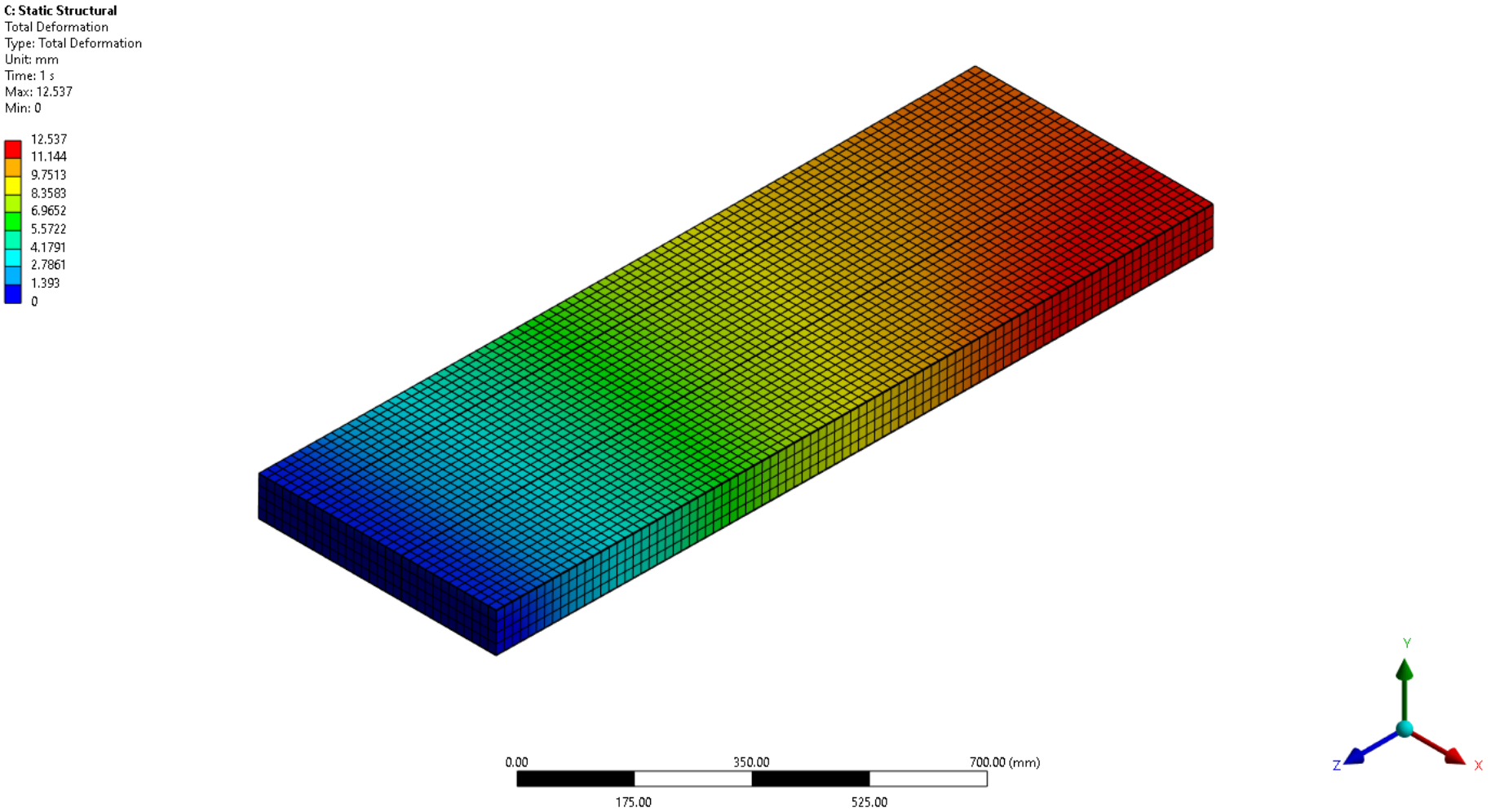

Figure B.2-5: Vertical deflection contour of configuration A90C80F1.2. Note that units are in mm.

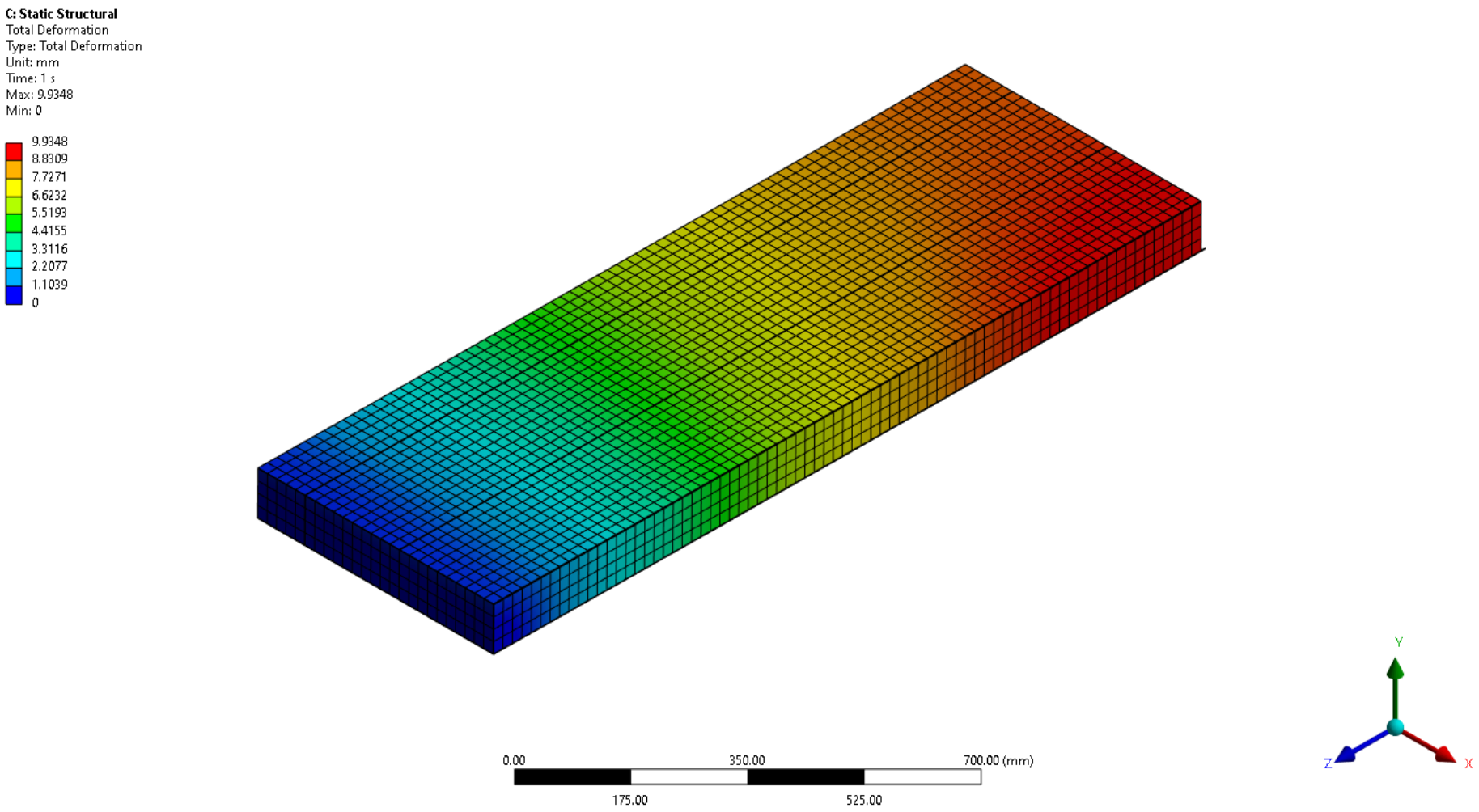

Figure B.2-6: Vertical deflection contour of configuration A90C90F1.2. Note that units are in mm.

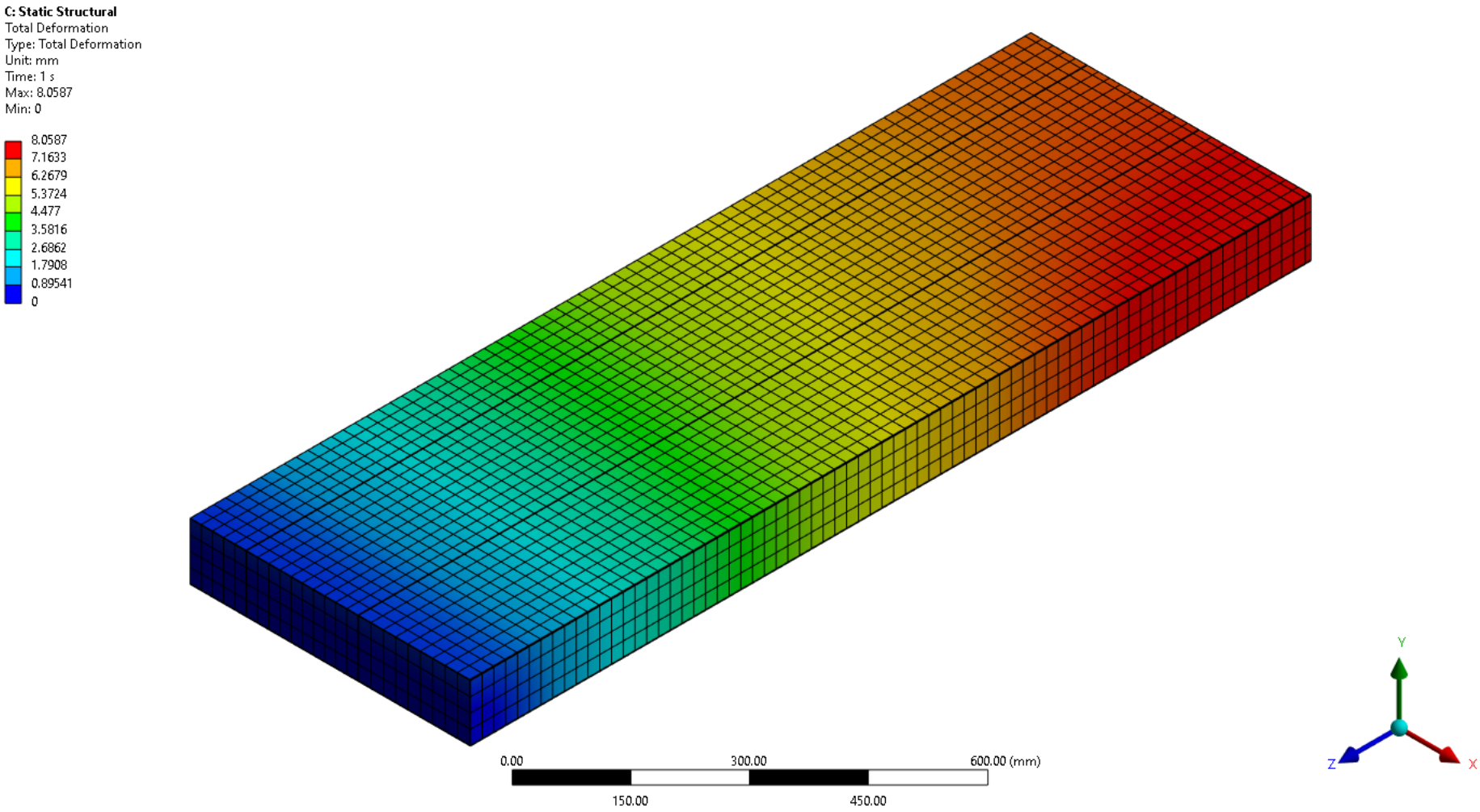

Figure B.2-7: Vertical deflection contour of configuration A90C100F1.2. Note that units are in mm.

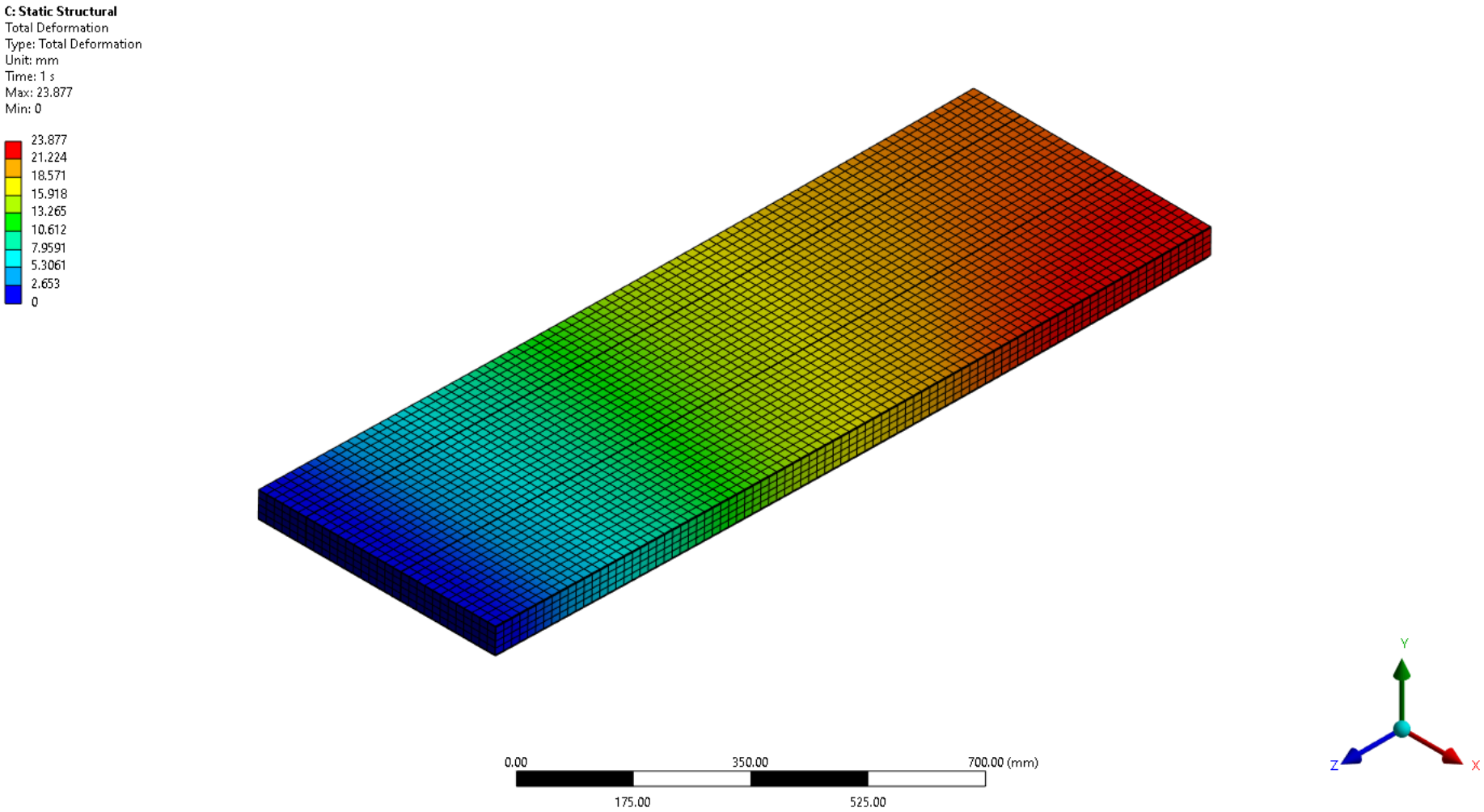

Figure B.2-8: Vertical deflection contour of configuration A90C50F1.6. Note that units are in mm.

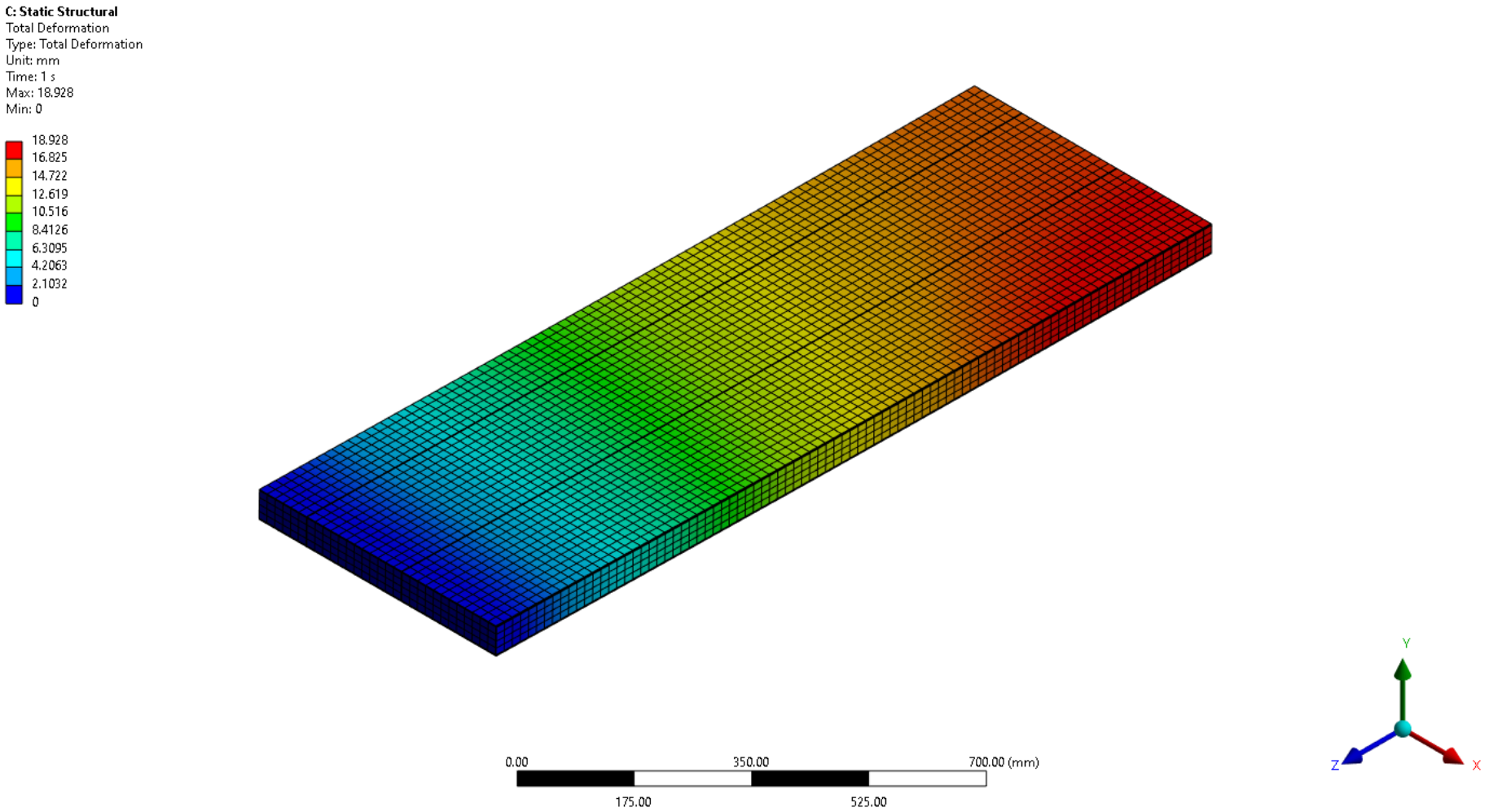

Figure B.2-9: Vertical deflection contour of configuration A90C50F2.0. Note that units are in mm.

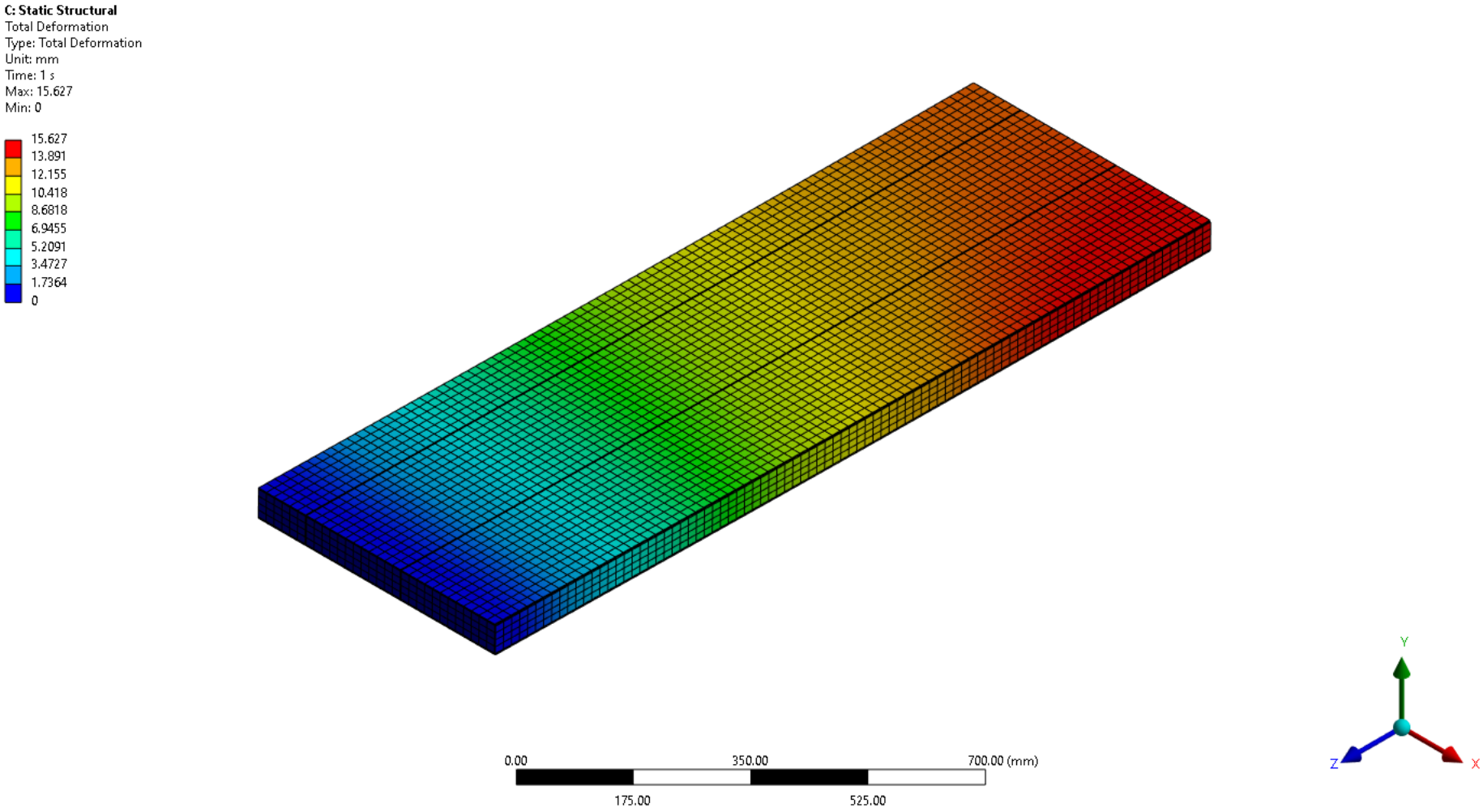

Figure B.2-10: Vertical deflection contour of configuration A90C50F2.4. Note that units are in mm.

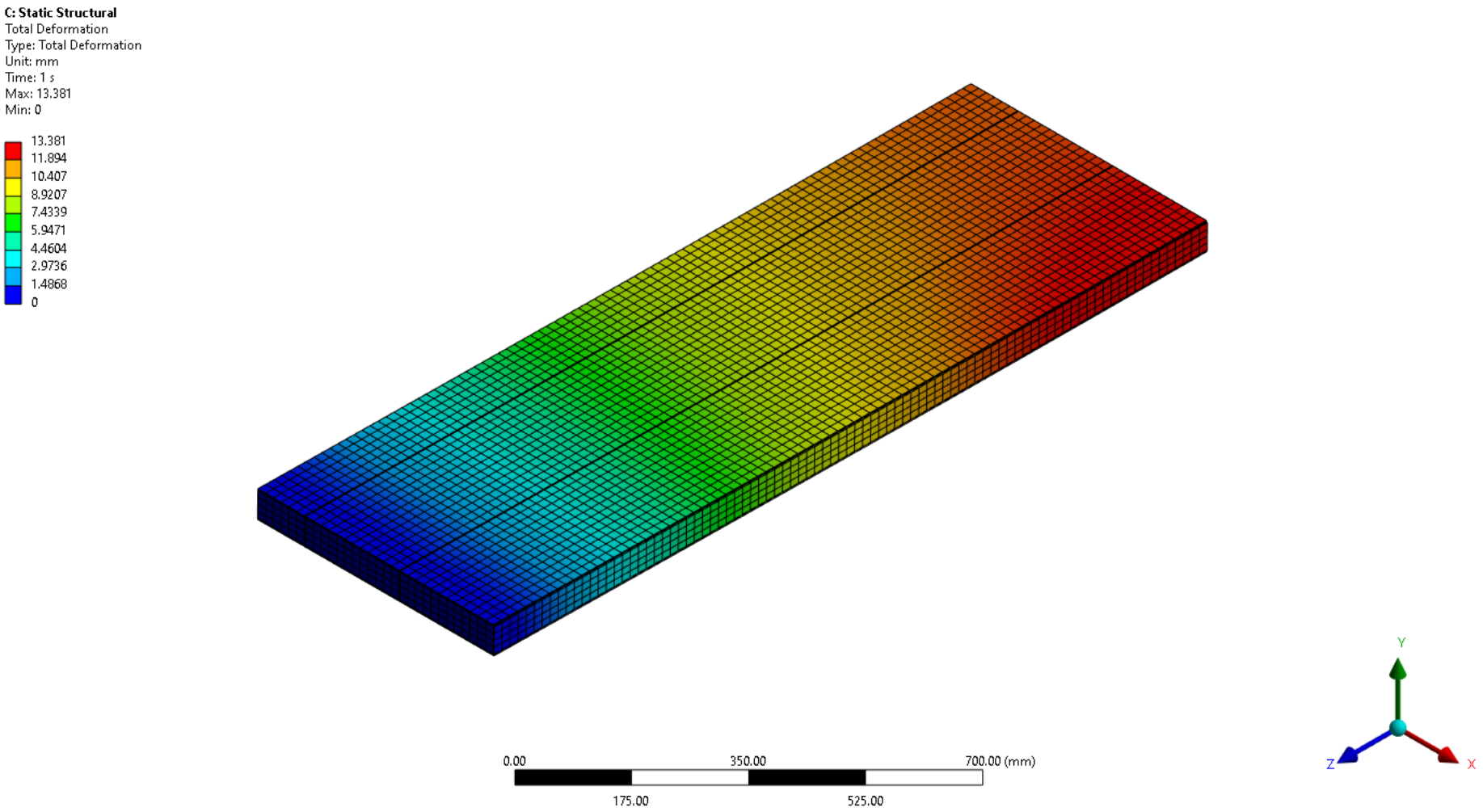

Figure B.2-11: Vertical deflection contour of configuration A90C50F2.8. Note that units are in mm.

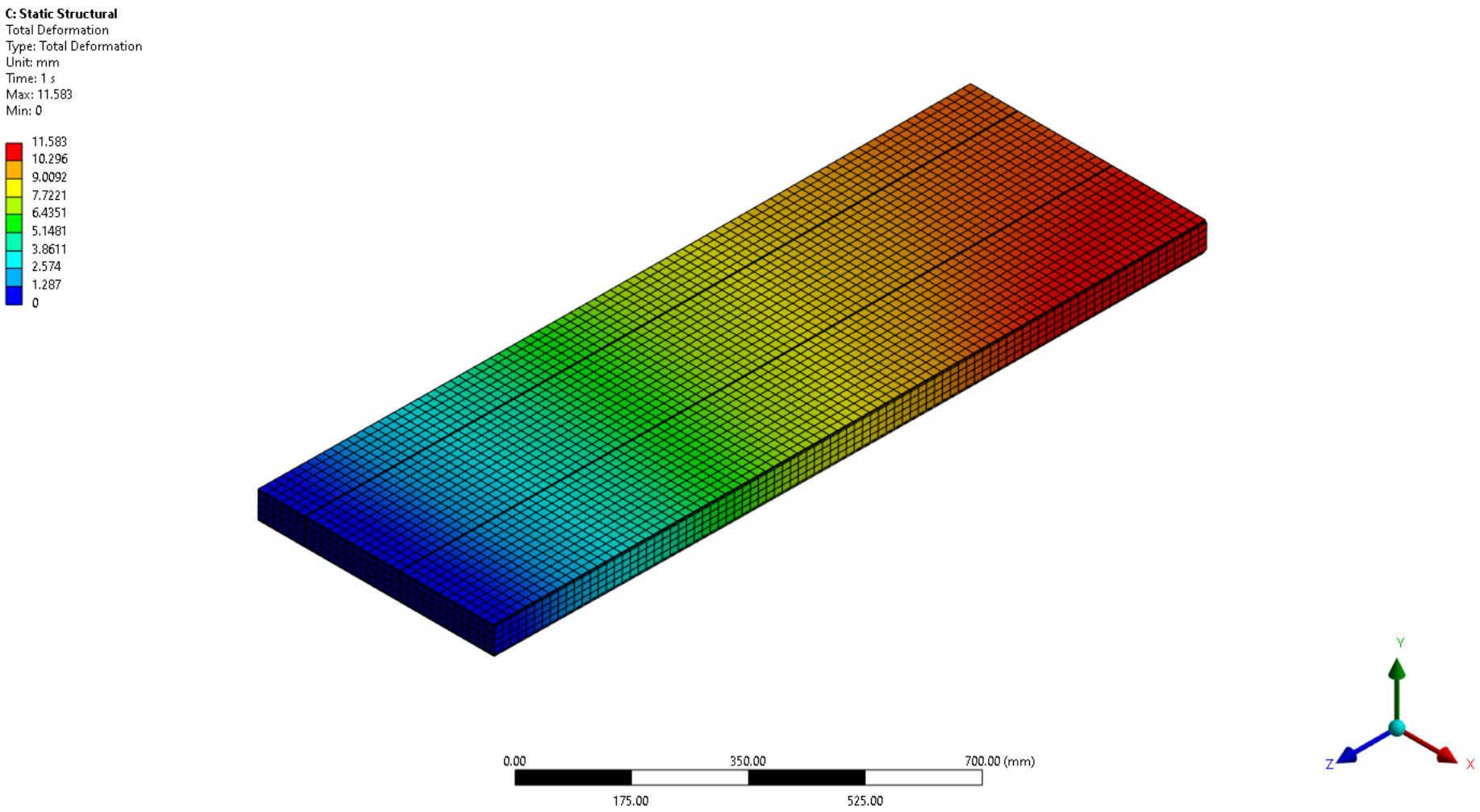

Figure B.2-12: Vertical deflection contour of configuration A90C50F3.2. Note that units are in mm.

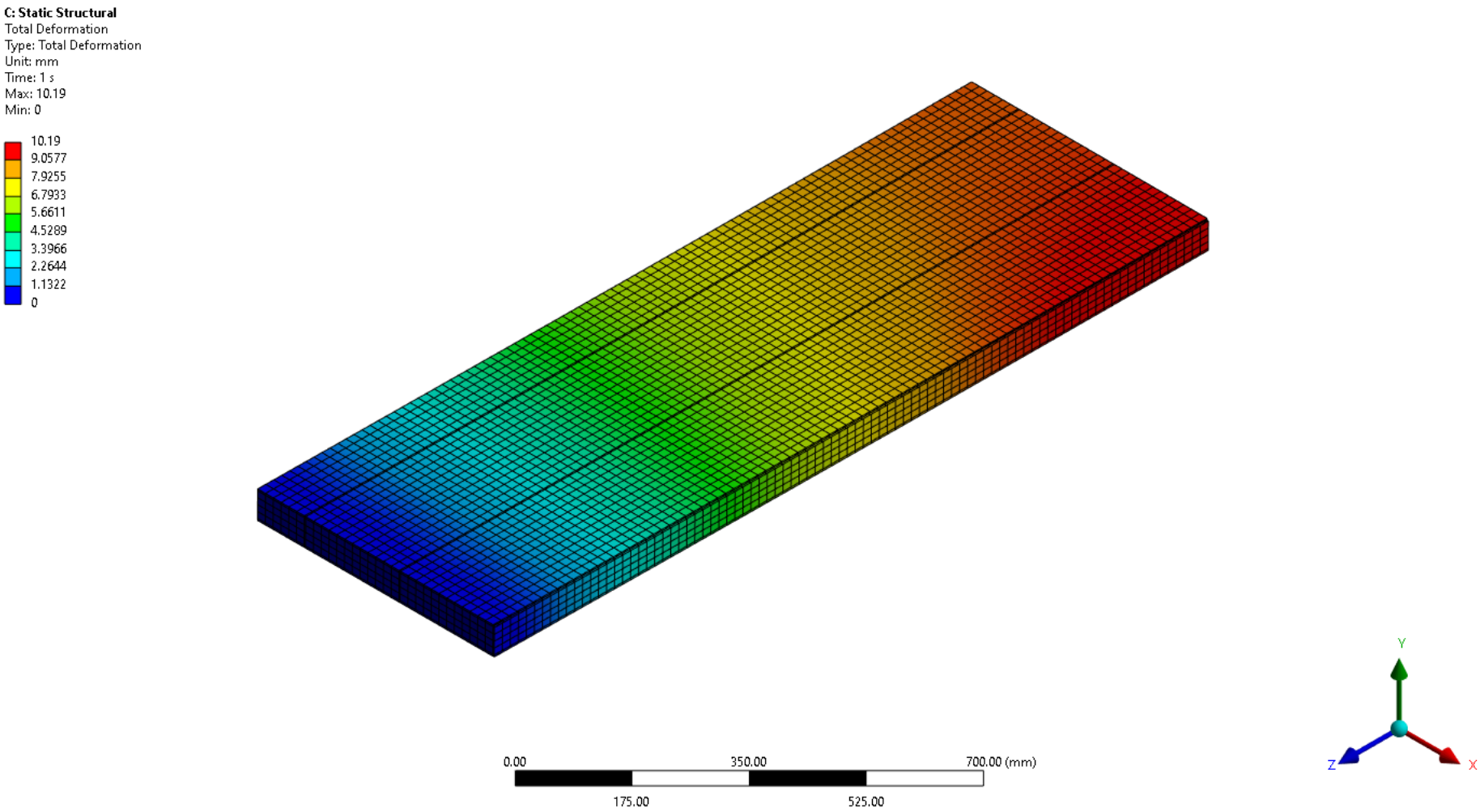

Figure B.2-13: Vertical deflection contour of configuration A90C50F3.6. Note that units are in mm.

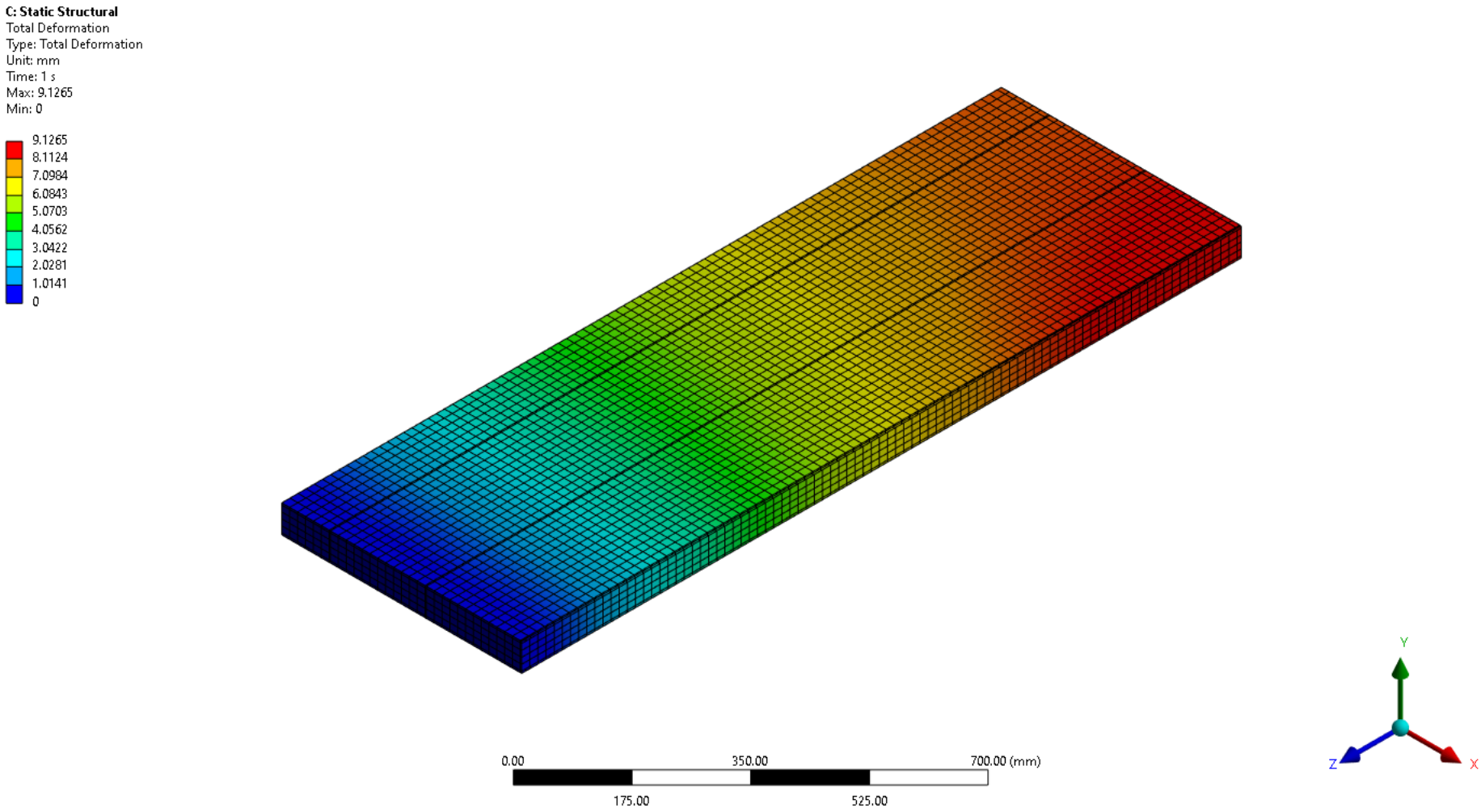

Figure B.2-14: Vertical deflection contour of configuration A90C50F4.0. Note that units are in mm.

Appendix B.3.

This appendix serves to display all the Von Mises stress contours mentioned in *Section 4.1.3.* Figures B.3-1 through B.3-10 show only a quarter of the contour due to symmetry along the longitudinal and transverse axes. Each figure includes a key that indicated the portion of the panel shown, boundary conditions, and, if applicable, stress singularities. Note that in the case of stress singularities, these were excluded from the Von Mises stress values, as reflected in the corresponding legends.

Four sections are present in this appendix. The order in which they are presented is as follows:

- Top Facesheet
- Bottom Facesheet
- Core #5
- Stiffener *E*

For each section, the contours are presented according to the order shown in Table B.3-1. Excluding the reference configuration, the table highlights four pairs of contours. The first three pairs examined the effect of varying a single variable; the first pair investigated changes in the angle of the stiffening system; the second pair explored changes in core thickness, and; the third pair addressed changes in facesheet thickness. The final pair examined the effects of varying two parameters simultaneously: first, the angle of the stiffening system with respect to core thickness and second, with respect to facesheet thickness.

Table B.3-1: Summary of the panel configurations considered, and their order. This is applicable to all section in this appendix.

Pair #	Configuration	Variable		
		Stiffener Angle	Core Thickness	Facesheet Thickness
Ref.	*A90C50F1.2*			
1	*A70C50F1.2*			
	A50C50F1.2			
2	*A90C70F1.2*			
	A90C100F1.2			
3	*A90C50F2.0*			
	A90C50F4.0			
4	*A50C100F1.2*			
	A50C50F4.0			

	Not Considered
	Considered

Top Facesheets

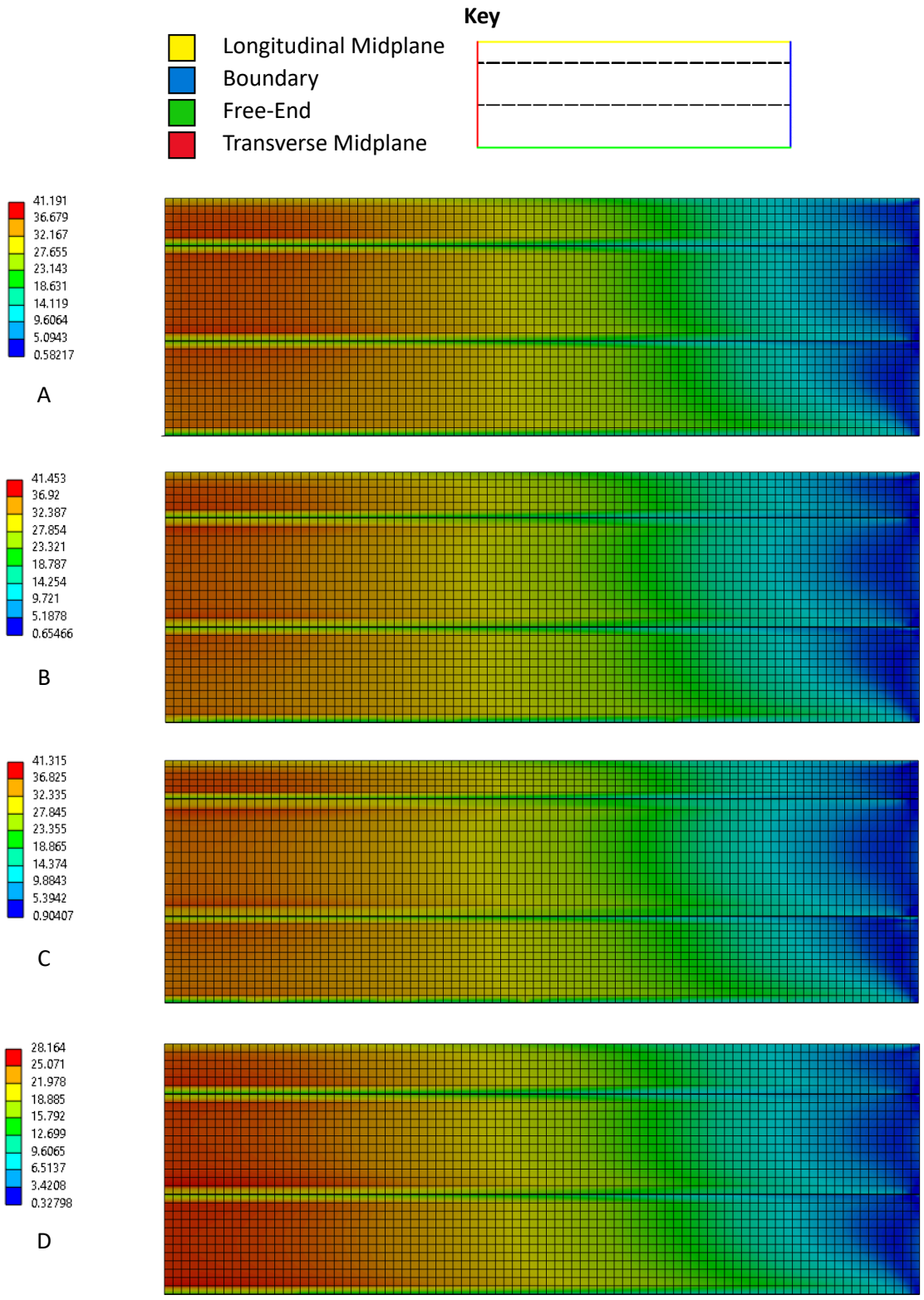

Figure B.3-1: Von Mises stress (MPa) contour of top facesheet for configuration: (A) A90C50F1.2; (B) A70C50F1.2; (C) A50C50F1.2; (D) A90C70F1.2.

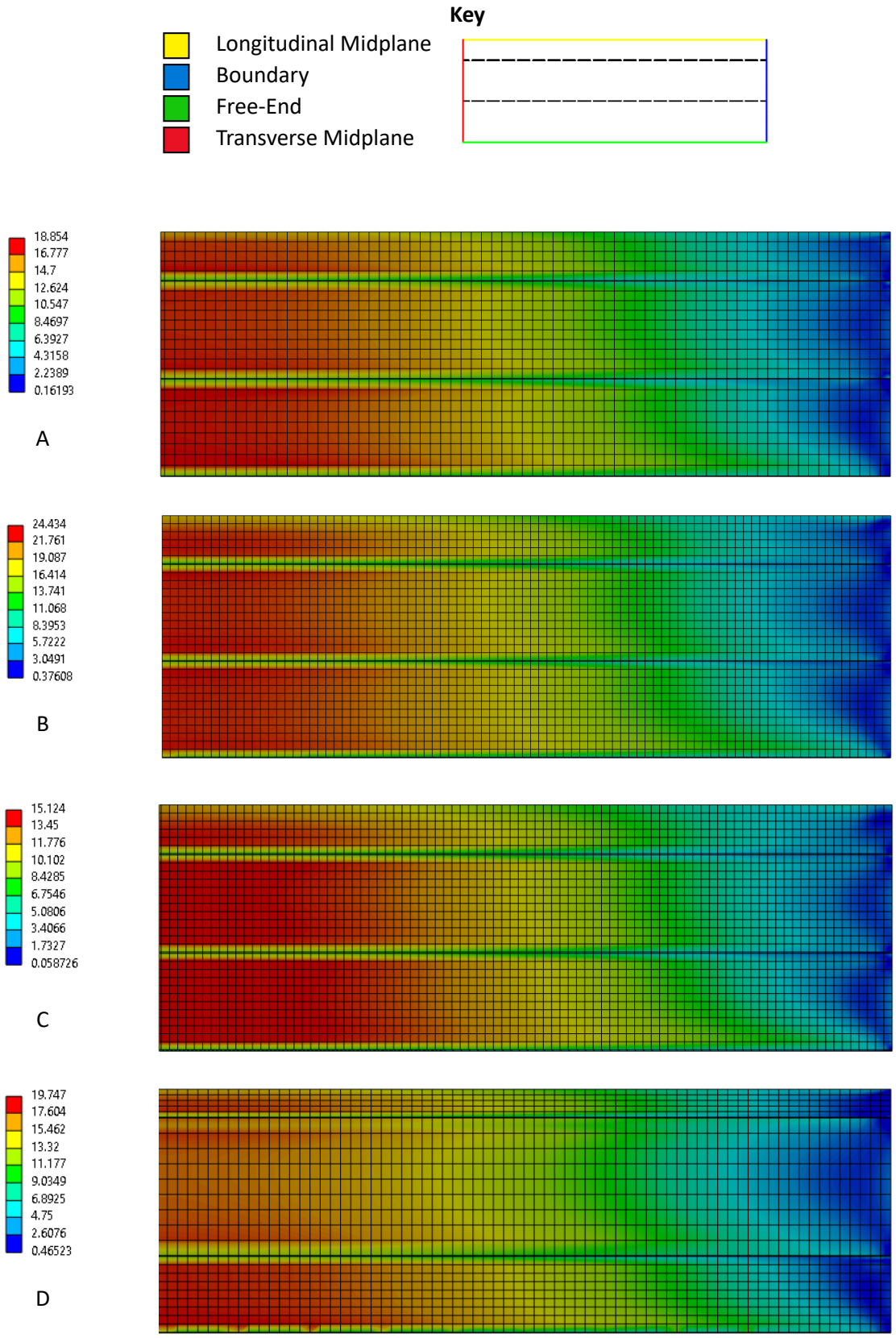

Figure B.3-2: Von Mises stress (MPa) contour of top facesheet for configuration: (A) A90C100F1.2; (B) A90C50F2.0; (C) A90C50F4.0; (D) A50C100F1.2.

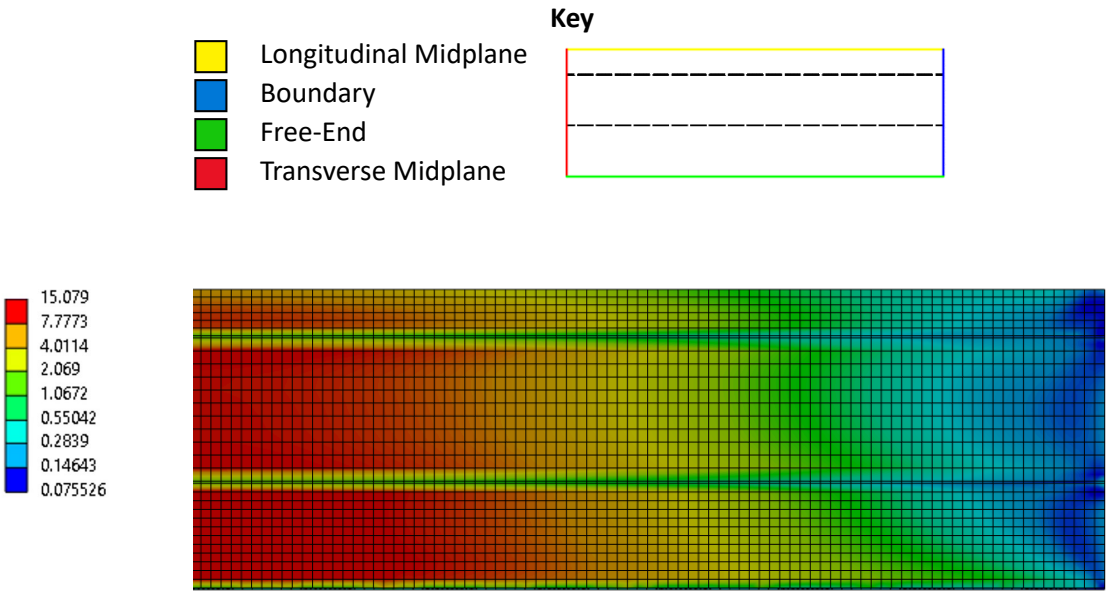

Figure B.3-3: Von Mises stress (MPa) contour of top facesheet for configuration A50C50F4.0.

Bottom Facesheets

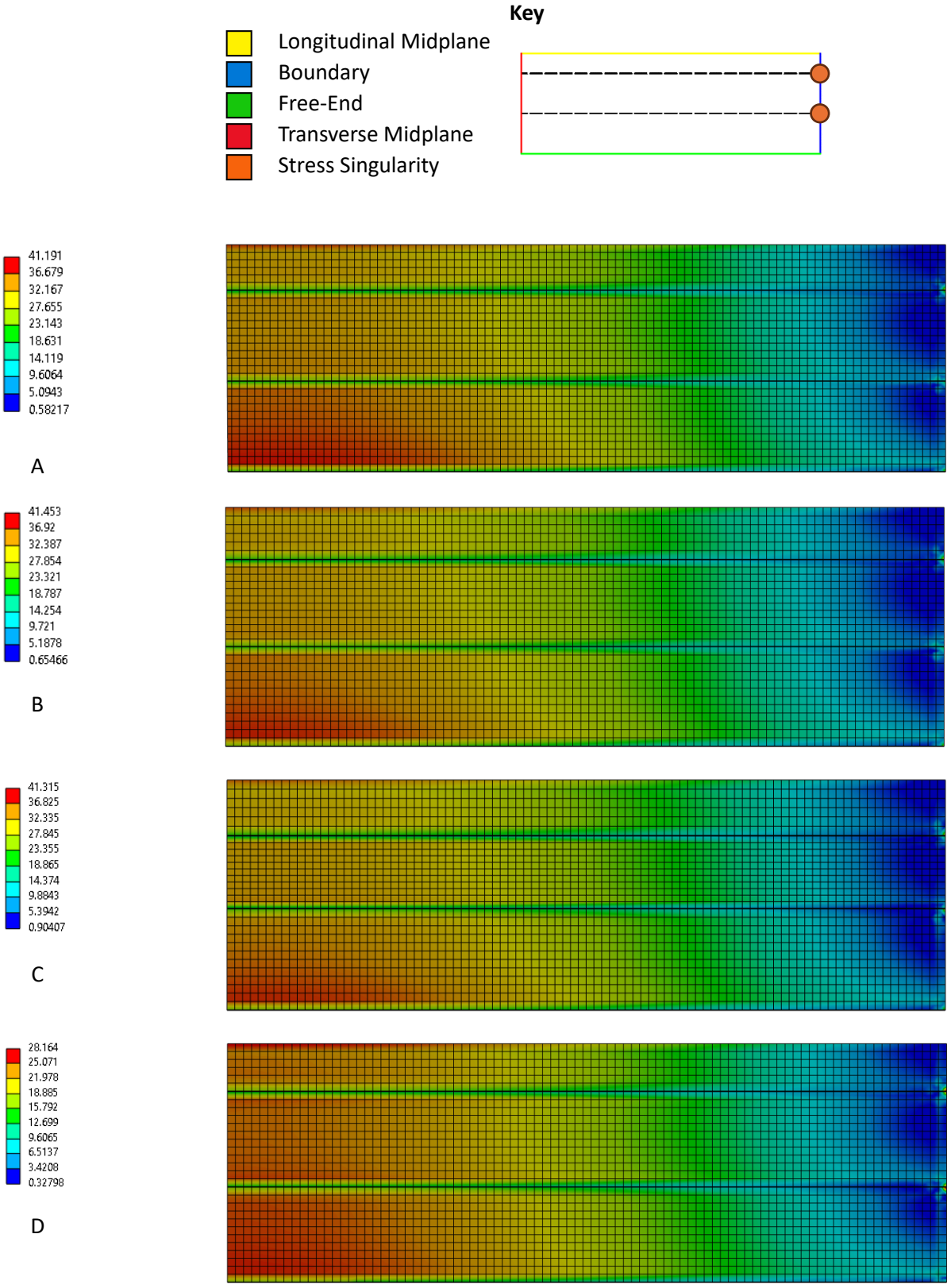

Figure B.3-4: Von Mises stress (MPa) contour of bottom facesheet for configuration: (A) A90C50F1.2; (B) A70C50F1.2; (C) A50C50F1.2; (D) A90C70F1.2.

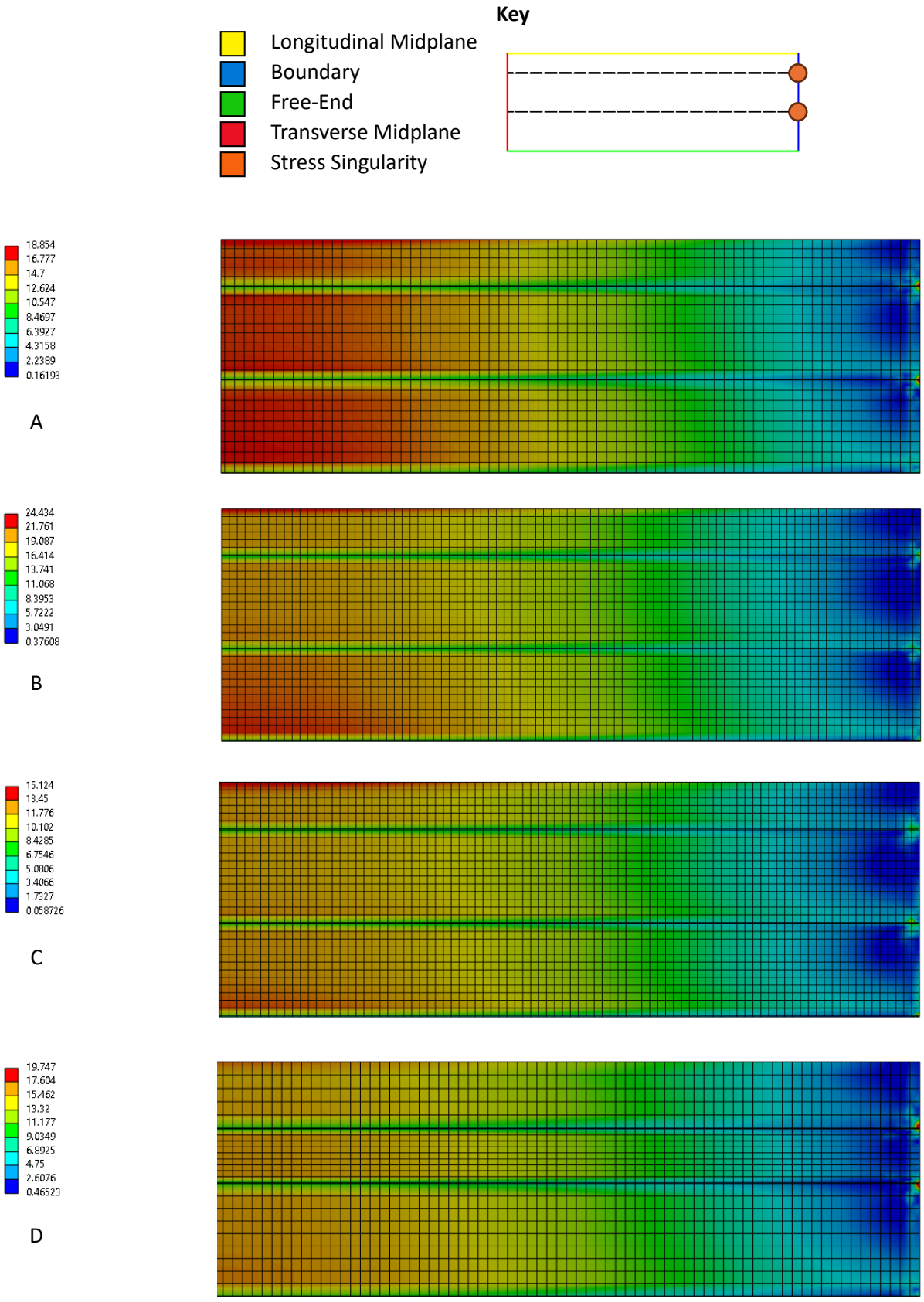

Figure B.3-5: Von Mises stress (MPa) contour of bottom facesheet for configuration: (A) A90C100F1.2; (B) A90C50F2.0; (C) A90C50F4.0; (D) A50C100F1.2.

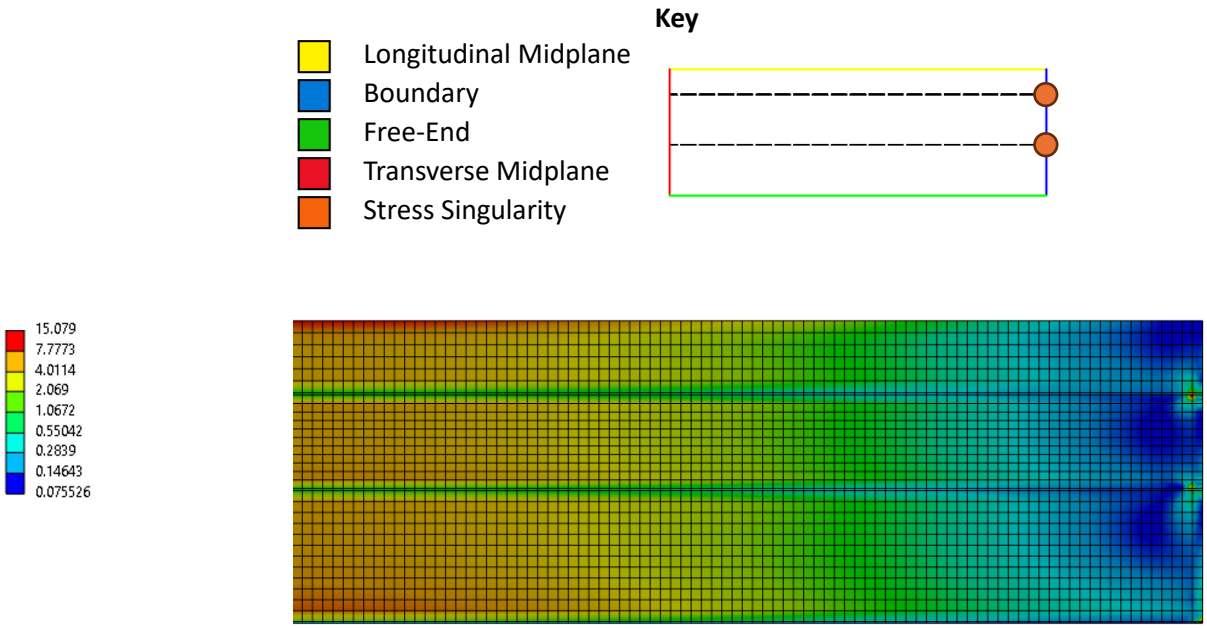

Figure B.3-6: Von Mises stress (MPa) contour of bottom facesheet for configuration A50C50F4.0.

Core #5

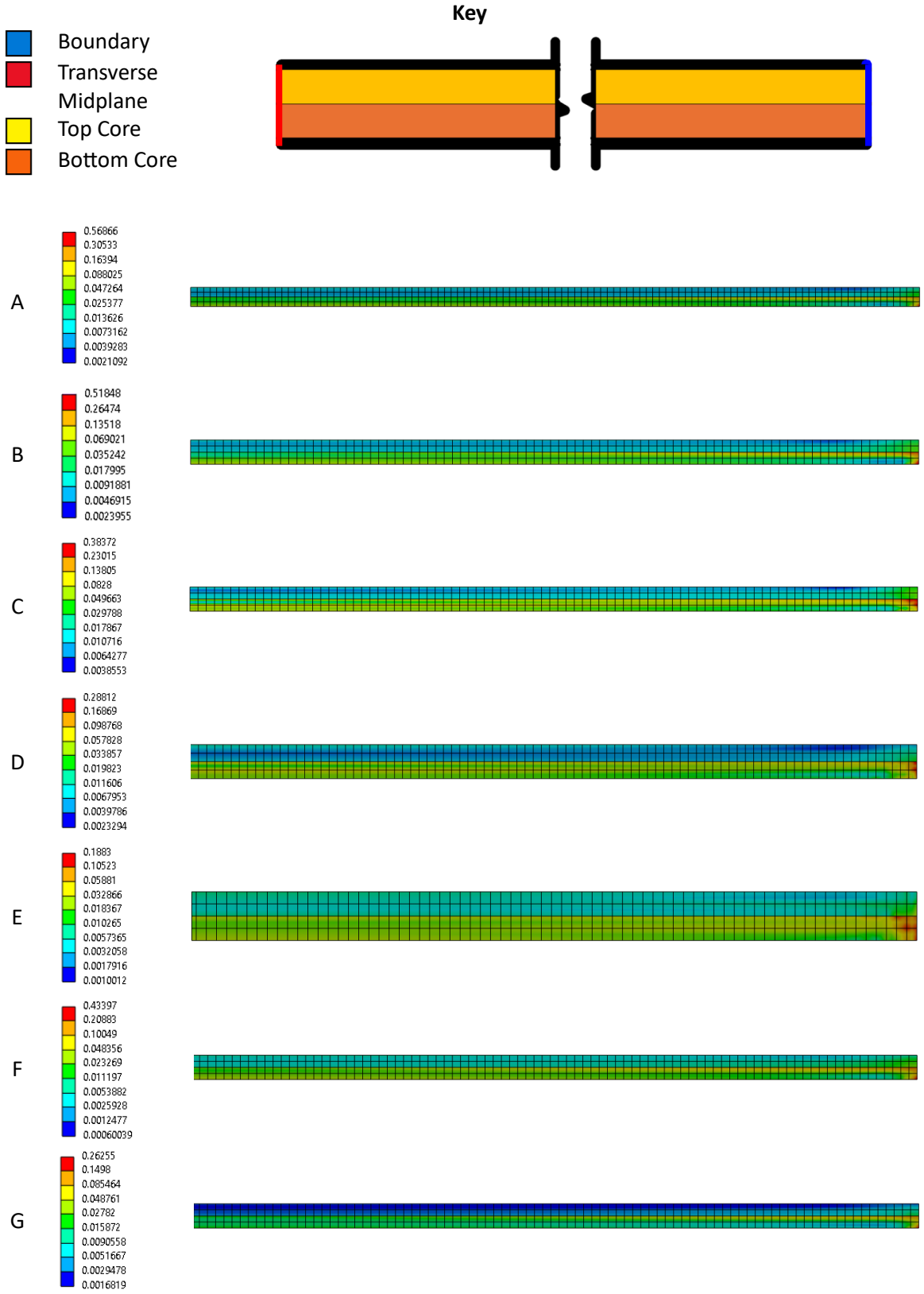

Figure B.3-7: Von Mises stress (MPa) contour of core #5: (A) A90C50F1.2; (B) A70C50F1.2; (C) A50C50F1.2; (D) A90C70F1.2; (E) A90C100F1.2; (F) A90C50F2.0; (G) A90C50F4.0.

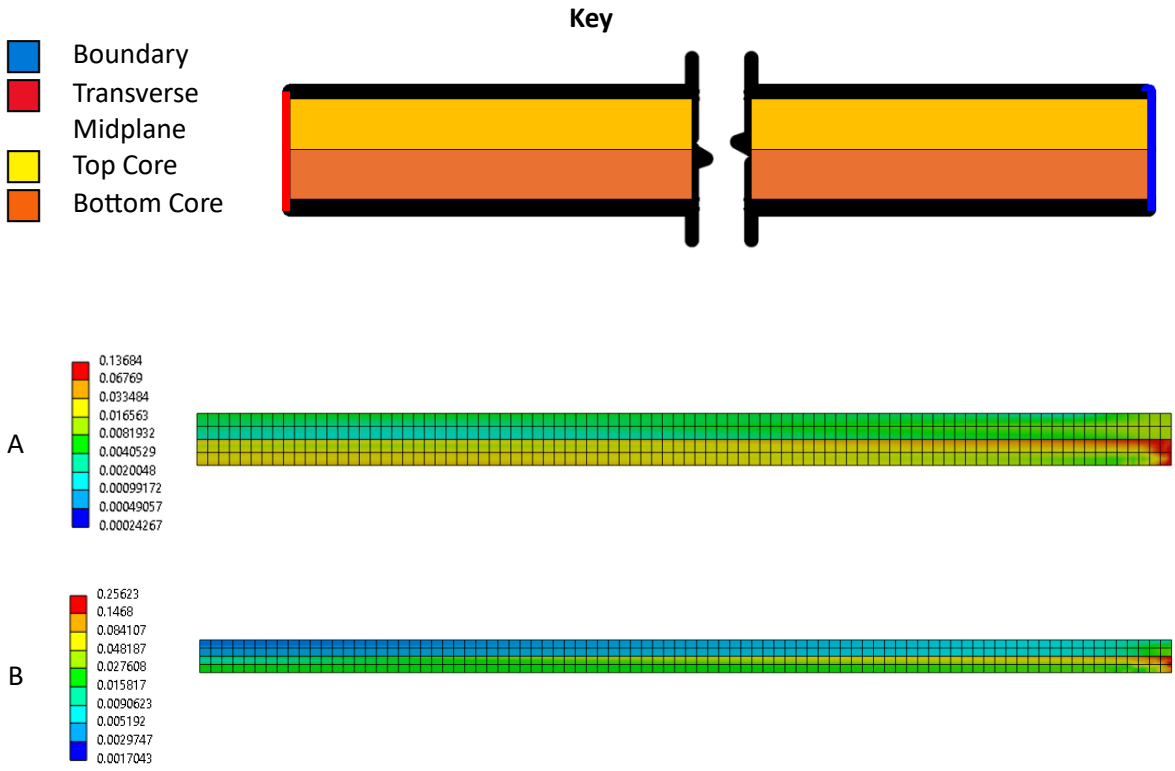

Figure B.3-8: Von Mises stress (MPa) contour of core #5: (A) A50C100F1.2; (B) A50C50F4.0.

Stiffener *E*

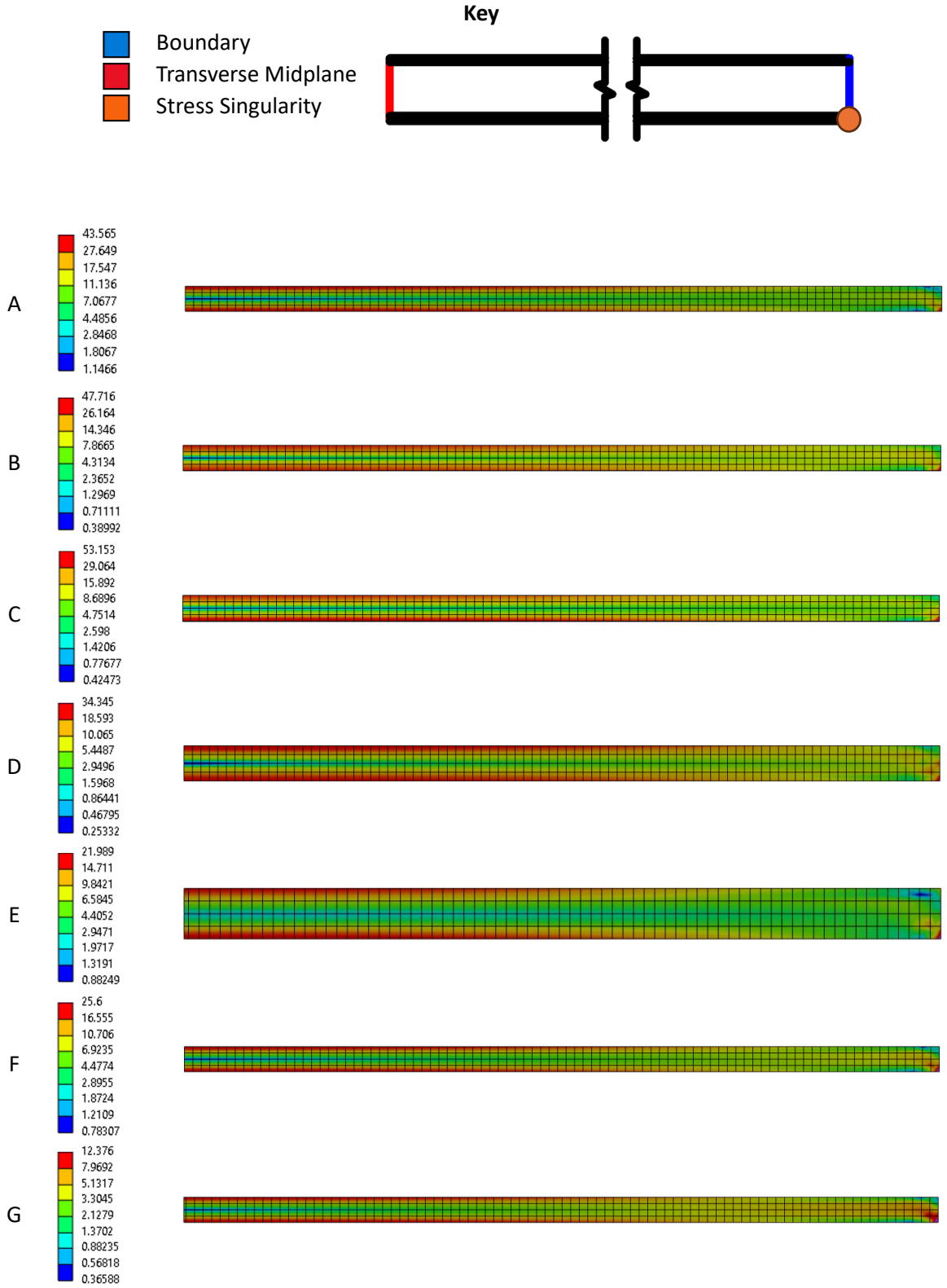

Figure B.3-9: Von Mises stress (MPa) contour of stiffener E: (A) A90C50F1.2; (B) A70C50F1.2; (C) A50C50F1.2; (D) A90C70F1.2; (E) A90C100F1.2; (F) A90C50F2.0; (G) A90C50F4.0.

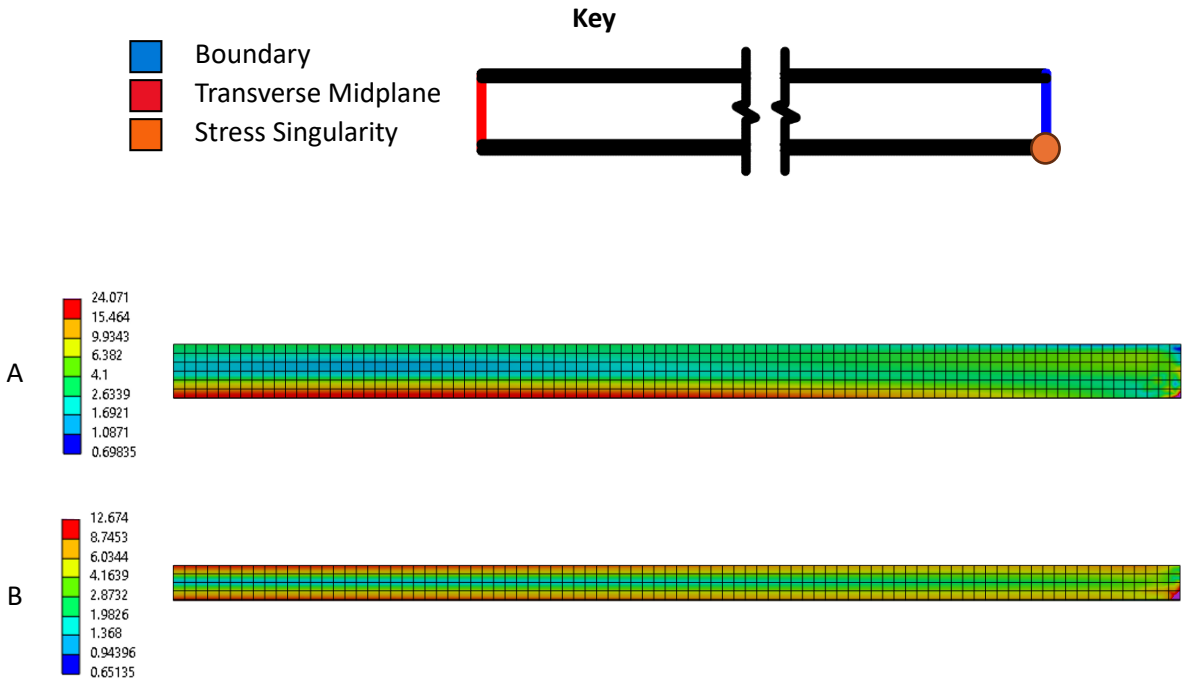

Figure B.3-10: Von Mises stress (MPa) contour of core #5: (A) A50C100F1.2; (B) A50C50F4.0.